~~SECRET~~

UNCLASSIFIED

NASA CR-54772
K-1672

[redacted]

DECLASSIFIED IAW attached letter
DATED 1-16-81 BY J. Osborne
ON Union Carbide letterhead
2-20-81 dw

CLASSIFICATION MARKINGS CHANGED
AS AUTHORIZED BY DOD 5200.1-R
ISPR NOV 73, 4-400

Prepared For
NATIONAL AERONAUTICS AND SPACE ADMINISTRATION
CONTRACT C-45120-A

UNION CARBIDE

UNION CARBIDE CORPORATION
NUCLEAR DIVISION

Operating the

OAK RIDGE GASEOUS DIFFUSION PLANT
OAK RIDGE Y-12 PLANT
OAK RIDGE NATIONAL LABORATORY
PADUCAH GASEOUS DIFFUSION PLANT

For the Atomic Energy Commission
Under U.S. Government Contract W7405 eng 26

~~SECRET~~

UNCLASSIFIED

Declassified
2-20-81 dw 54772

UNION CARBIDE CORPORATION
NUCLEAR DIVISION

TO: AFWL

DATE: 1-16-81

FROM: ORGDP, Plant Records Dept.

SUBJECT: Notice of Change in Classification

The Security classification of the document identified below has been changed from SECRET to UNCLASSIFIED by authority of D.S. Napolitan on 1-6-81

DOCUMENT NUMBER K-1672 DOCUMENT DATE 1-25-67

TITLE AND AUTHOR Summary Report - Porous Tungsten Ionizer Development and Testing, Nov. 15, 1964-Nov. 15, 1966
Author - R.B. Neal

Our records indicate you are charged with copy 25

on receipt 960351 Please take the following action:

- [✓] Delete old classification
- [ ] Special instructions
- [✓] Add new classification
- [✓] Delete old admonitory marking
- [ ] Add new admonitory marking
- [✓] Delete documentation

[✓] Place this statement on first page or cover:

Classification changed to UNCLASSIFIED

by authority of D.S. NAPOLITAN — 1-6-81

by _____ Date _____
(Person making change)

CAUTION

The subject document is not to be released to the public or given unrestricted external distribution without approval of the Law Department of UCC-ND.

Judy Osborne
Records Department

UCN-649
(1235 5-73)

[redacted]

Date of Issue: January 25, 1967 Report Number: NASA CR-54772
K-1672

Subject Category: SPECIAL

SUMMARY REPORT
POROUS TUNGSTEN IONIZER
DEVELOPMENT AND TESTING
NOVEMBER 15, 1964 - NOVEMBER 15, 1965

By
R. B. Neal

Prepared for
National Aeronautics and Space Administration
Contract C-45120-A

Technical Management
NASA Lewis Research Center
Cleveland, Ohio
Spacecraft Technology Division
Thomas J. Riley

UNION CARBIDE CORPORATION
NUCLEAR DIVISION
Oak Ridge Gaseous Diffusion Plant
Oak Ridge, Tennessee

[redacted]

Report Number: NASA CR-54772
K-1672

Subject Category: SPECIAL

Title: SUMMARY REPORT - POROUS TUNGSTEN IONIZER DEVELOPMENT AND TESTING NOVEMBER 15, 1964 - NOVEMBER 15, 1965

Author: R. B. Neal

A B S T R A C T

A method for direct forming of ionizer shapes is described in which highly classified tungsten microspheres can be used to produce efficient ionizer materials. A technique for hot pressing ionizer materials is also presented. In addition to complex ionizer shapes, forming included the preparation of porous tubes and porous fibers and very high permeability material for mercury flow control in electron bombardment ion engine experiments.

The testing of ionizers is described in detail. In addition to conventional tests several novel tests were investigated, including permeability scanning and precise radiation gauging. A detailed discussion of the determination of transmission coefficient is included.

The classification and evaluation of 40 lbs. of tungsten microspheres is described.

POROUS TUNGSTEN IONIZER DEVELOPMENT AND TESTING

TABLE OF CONTENTS

TABLE OF CONTENTS (Continued)

TABLE OF CONTENTS (Continued)

LIST OF ILLUSTRATIONS

LIST OF ILLUSTRATIONS (Continued)

LIST OF ILLUSTRATIONS (Continued)

LIST OF ILLUSTRATIONS (Continued)

LIST OF TABLES

LIST OF TABLES (Continued)

LIST OF TABLES (Continued)

POROUS TUNGSTEN IONIZER DEVELOPMENT AND TESTING

I. INTRODUCTION AND SUMMARY

Previous Work

Previous work on the preparation of porous tungsten for contact ionizers has been done primarily by conventional means. In most cases a suitable tungsten powder has been ram-pressed or isostatically pressed into buttons or billets, sintered to the required density and pore size, infiltrated with a suitable pure metal or alloy and machined to the required shape. The surface is treated by an etching technique to assure open porosity at the machined surfaces. The infiltrant is then vacuum-evaporated to return the sample to full porosity. This approach has been used almost exclusively by some investigators (1). This procedure, as briefly outlined above is both elaborate and costly. The machining requires a large excess of material in order to provide for machining losses and the machining process in itself is expensive and time consuming. A variation in this process has been developed by others (2). In this variation the tungsten powder is loaded into a warm pressing die of relatively large shape. The powder is carefully raked and combed to assure uniform die loading. It is then warm-pressed at about 300°C. and 80,000 psi. for 1/2 hour. The resulting blank is then sintered at up to 2000°C. to achieve final density. As with the previously described process, this blank or slab is infiltrated, machined to shape, etched, and the infiltrant evaporated. While this process has resulted in improved ionizers from the standpoint of uniformity of pore size, permeability and density, it has complicated rather than simplified the production process.

Another approach to the preparation of porous tungsten ionizers has involved liquid phase sintering (3). In this case the tungsten powder is mixed with an infiltrant such as copper-nickel and sintered at temperatures on the order of 1500°C. The copper-nickel alloy dissolves the tungsten, which is then reprecipitated in preferential sites, resulting in somewhat spheroidal grains and the development of a spheriodal pore shape. Most of the copper-nickel phase is then leached

out of the tungsten matrix with hot nitric acid. Subsequent vacuum evaporation serves the double purpose of reducing the copper-nickel percentage to low levels and increasing the density to the required range. Fabrication of the resulting porous tungsten into ionizer buttons or shapes requires infiltration with copper, machining to required dimensions and final evaporation of the copper. The multiple steps required with this process obviously result in high fabrication costs.

Purpose and Scope of Present Work

The purpose of the work reported here was to demonstrate that shapes could be directly formed and then sintered without machining and concomitant loss of expensive material. A secondary but important objective was to demonstrate that ionizers of equivalent or superior uniformity and operating characteristics could be made by these techniques.

The scope of the program is best illustrated by a quotation from the Work Statement:

> "The Contractor shall conduct a program on a best effort basis of developing and testing porous ionizer materials directed toward the achievement of the following long-range design goals:
>
> a. The program will develop, by suitable pressing and sintering techniques, ionizers finished as to size and shape, as required for thrustor engines.
>
> b. The design goals of the finished ionizer should be:
>
> (1) Pore diameter
>
> One micron or less, uniformly distributed.
>
> (2) Pore density
>
> More than 10^7 pores per sq. cm.

(3) Life

Capable of 10,000 hours of operation under ionization conditions (1200° - 1400°C. with cesium) and with no change in structural characteristics such as pore size, volume or density and gas permeability.

(4) Emissivity

The value of the total emissivity of the surface to be 0.3 or less.

(5) Critical temperature - work function

The ionizer shall have the lowest critical temperature consistent with the highest current density, and the highest work function. This goal includes a surface work function of 4.4 ev. minimun.

(6) Density

The density variation within the ionizer shall be less than 1 percent.

(7) Purity

To be determined by quantitative spectrographic analysis and should be as shown in Appendix A." (Table I is a reproduction of the purity specification, Appendix A, Contract C-45120-A.)

Another aspect of the program was to determine the properties of the ionizers and to show that they are equivalent to other presently developed ionizer materials. The tests required are enumerated under Phase II of the contract "Testing and Evaluation" and are quoted below:

"1. Spectrochemical analysis
2. Bubble testing
3. Permeability (specific flow testing)
4. Density by gas displacement technique

TABLE I

REPRODUCTION OF THE PURITY SPECIFICATION TABLE
FROM CONTRACT C-45120-A

(APPENDIX A - LEVELS OF PURITY REQUIRED IN
TUNGSTEN AND TUNGSTEN ALLOYS)

Element	Maximum Allowed Content, ppm. (% Weight)	Group	Element	Maximum Allowed Content, ppm. (% Weight)	Group
Li	10	I A	Hf	10	IV B
Na	10	I A	Th	10	IV B
K	10	I A	Sb	10	V A
Rb	10	I A	Bi	10	V A
Cu	15	I B	V	10	V B
Ag	10	I B	Nb	10	V B
Ca	10	II A	Ta*	50	V B
Sr	10	II A	Cr	15	VI B
Ba	10	II A	Mo	250	VI B
Be	10	II A	Mn	10	VII B
Mg	10	II A	Re	50	VII B
Zn	10	II B	Fe	50	VIII
B	10	III A	Co	10	VIII
Al	10	III A	Ni	10	VIII
C	30	IV A	Rh	10	VIII
Si	20	IV A	Pd	10	VIII
Sn	10	IV A	Os*	10	VIII
Pb	10	IV A	Ir*	10	VIII
Ti	10	IV B	Pt	10	VIII
Zr	10	IV B			

*This limit only applies when element is not specifically added.

5. Void surface area (BET krypton method)
6. Total void fraction by mercury immersion
7. Mercury intrusion
8. Hydraulic pore radius
9. Metallography at 2000 magnification
10. Crystallographic orientation and strain by X-ray
11. Surface work function
12. Transverse rupture or hardness testing
13. Simulated life testing to project lifetime of ionizer."

In the original conception of the program, methods of determining uniformity were to be explored as the program developed and as the need became evident. The requirement for ionizers of improved uniformity made it apparent that a uniformity test superior to what was presently available would be required. With this in mind, the development of a permeability uniformity test was undertaken.

Experimental Approach

As mentioned earlier, the primary object of this work was to develop a method of forming ionizer shapes directly, then sintering to final size. Figure 1 shows the ionizer shape which was selected as one of the shapes to be produced under this contract. The shape dimensions were taken from Hughes Research Laboratories Drawing C-835931 Rev. B supplied by NASA's Lewis Research Center. Another method to be used in this program was to hot press the tungsten powder in graphite dies to the general shape and then sinter to final size in pure hydrogen. Pressing tungsten in graphite dies is common; however, it is not usually used for complicated parts with close tolerances. The final sintering in high purity hydrogen was intended to remove the carbon by reduction. In this particular application a high vacuum furnace was used for the final hydrogen sintering. This furnace can first be evacuated to a pressure of 10^{-5} Torr before the introduction of the hydrogen so that the hydrogen can enter the pores of the tungsten and effectively remove the residual carbon.

DWG. NO. G-66-600

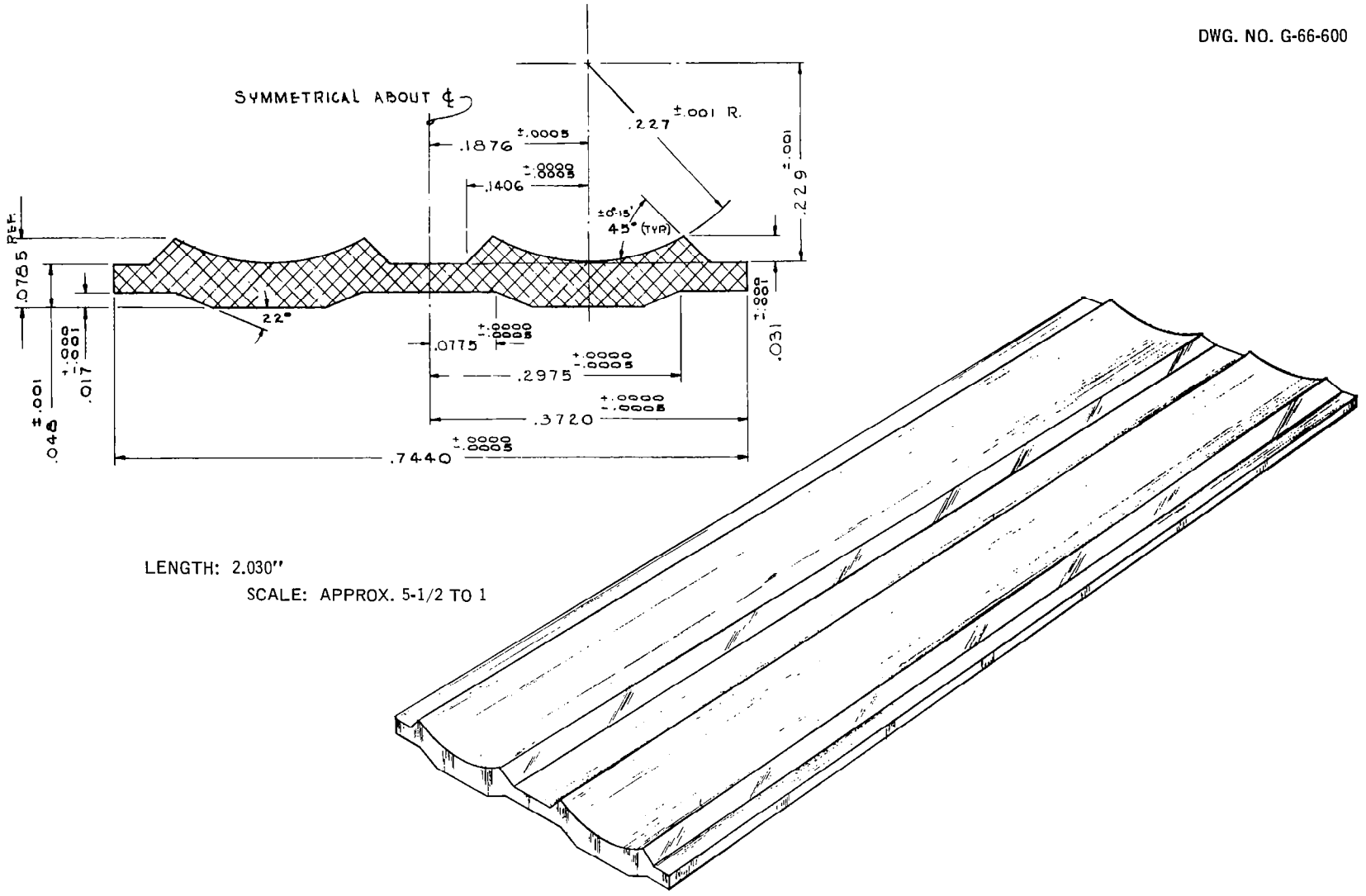

LENGTH: 2.030"

SCALE: APPROX. 5-1/2 TO 1

POROUS TUNGSTEN IONIZER SHAPE
MODIFIED HUGHES DESIGN

Figure 1

Recognition of Similar Work

To our knowledge, there have been no other reported attempts to form ionizers to shape other than by conventional machining methods. Most of the work reported in the literature has involved pressing and sintering. As mentioned previously, Hughes ionizer blanks have been warm-pressed prior to sintering, but machining is still required to form the shape. Most of the other contractors have used spherical powders in their ionizer fabrication work. Since the spherical powders have been shown to produce ionizers with superior operating characteristics, the scope of this contract called for their ultimate use in the process.

Program Results

Significant accomplishments of this program are summarized below.

1. The general applicability of the technique of direct forming of the ionizer shape has been demonstrated.

2. The applicability of classified spherical tungsten powders to this process has been shown.

3. The possible use of hot pressing as an ionizer fabrication method has been demonstrated. Dies can be made with various types of inserts and carbon can be removed by reduction in hydrogen.

4. Evaluation methods for determining pore size, uniformity and permeability have been demonstrated. Flow measurements which are generally used for porous materials have been used primarily to determine these parameters. The feasibility of a permeability scanning technique for uniformity testing has been demonstrated, and the determination of density variations by narrow beam radiation absorption gauging has been shown.

5. Auxiliary materials of various types have been prepared in the course of this work. The usefulness of various porous materials in other applications became apparent during the contract period. These have included:

Mercury Flow Control. During the program it became apparent that some of the material which had been prepared was of higher permeability than most porous tungsten available and could very reasonably be applied to the control of mercury flow in the electron bombardment engine. Porous slabs of this type were supplied to NASA for evaluation in the application and were found to be acceptable. As a result, NASA requested approximately 80 linear inches of material of a similar type but of still higher permeability. The material was to be 1 in. wide by 0.057 in. thick in lengths of about 2 in. It was to have a void fraction of 0.48 and a transmission coefficient of 1×10^{-3}. The necessary design and fabrication variables were worked out and the material was being prepared at the close of the contract period.

Porous Tungsten Tubes. Porous tungsten tubes having particular specifications were also supplied to NASA for an undisclosed application.

Porous Tungsten Fibers. As a result of an expressed interest by NASA porous tungsten fibers have been prepared in the diameter range of 0.002 in. to 0.010 in. These fibers have been sintered at up to 2000°C. and have been shown to be reasonably strong although they do exhibit the usual brittleness characteristic of sintered tungsten.

II. DIRECT FORMING

The object of this phase of the program was to form material directly to the required shape using suitable dies and then sinter to the final dimensions and properties. Material was formed both as rectangular flats and as ionizer shapes using this approach. The flat samples were made primarily for testing since a flat sample is more convenient for most of the tests which are performed on ionizer materials. The shapes were formed in order to demonstrate the capability of the process, the shape in this case being that of the Hughes Research Laboratories design as shown in figure 1.

The formed material was then sintered in two steps to achieve final density and dimensions. First it was low temperature-sintered at 1200°C. in hydrogen. Secondly it was high temperature-sintered in

purified hydrogen at up to 2000°C. This sintering cycle decreases the carbon content to less than 10 ppm. which is below the level at which it was present in the original powder. The samples were sintered generally on tungsten plates with heavy tungsten radiation shields surrounding them on all sides to form a black body condition with tungsten walls. Some sintering was done in the vacuum hot press with the rams retracted, thus using the press as a sintering furnace.

Specific experimental work using the direct forming and sintering technique is described in the following paragraphs.

Direct Forming with Angular Powders

In order to demonstrate the feasibility of the process most practically and economically, the use of angular powders was felt to be the best approach. A relatively cheap, unclassified powder was selected for use in the process first; following a successful fabrication of the unclassified powder, a classified fraction of angular powder was then used.

Use of Unclassified Angular Powder. The first successful fabrications were made with Sylvania M-30 angular tungsten powder. This powder has a broad particle size distribution with an average diameter of about 3 microns by Micromerograph. It is described more fully in Section VI. Few difficulties were encountered in demonstrating that shapes could be fabricated directly. An example of the fabrication is shown in figure 2. This is the modified Hughes design, previously mentioned. The as-formed shape in this case is 12 in. long.

Use of Classified Angular Powder. A classified fraction of Firth Sterling angular powder was used in attempts to show that this type of powder could be fabricated by the direct forming method. This powder had an average particle diameter of about 3.2 microns by Micromerograph. It is described also in Section VII of this report. About 20 attempts were made to fabricate this powder without success. When the spherical powders became available, work with the angular classified powder was curtailed. The reason for the failure is now understood; however, there

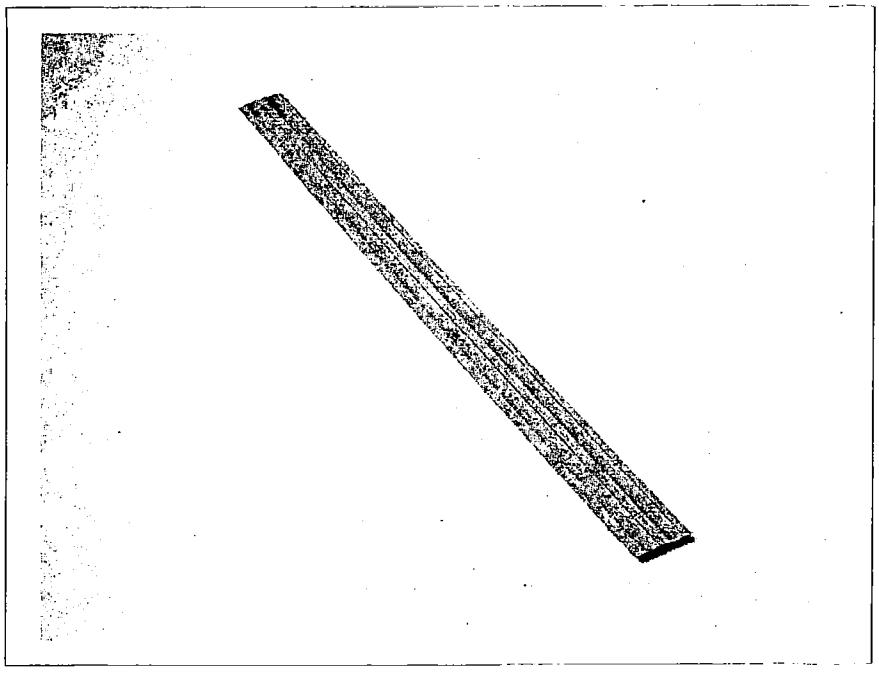

SHAPE MADE BY DIRECT FORMING
Figure 2

has been no further need to fabricate material from this powder and thus no additional work has been done with it.

Direct Forming with Spherical Powders

After successful fabrication of shapes from the angular powder, spherical powders were incorporated into the process. Larger powders were felt to present fewer problems in fabrication, and thus were used first. Following this, some of the finest available classified spherical powders were used successfully.

Use of Precut Linde Microspheres. Three different sizes of classified tungsten microspheres were purchased from the Linde Division of Union Carbide Corporation. These powders had average particle diameters of 4.1, 4.8, and 5.8 microns as determined by microscopic particle count. They are further described in Section VI and are compared with other classified powders in Appendix III, Classification of Spherical Tungsten Powder. The 4.8-micron powder was first used successfully in the direct forming process. Following this success the largest powder 5.8 microns, and finally the smallest powder, 4.1 microns, were used with no serious problems. In these experiments with spherical powder, a flat, rectangular shape 7/8 in. wide x 0.060 in. thick was made rather than the Hughes 2-strip ionizer design since it was felt that the flat samples could be more readily used for evaluation.

Use of Sharply Cut Microspheres. In order to provide additional spherical tungsten for the program, 40 lbs. of microspheres were purchased from Linde to a specification of 75% less than 10 microns by count. This powder was classified into 17 sharp fractions by Vortec Products Company, Torrance, California, using their C-1 particle classifier. These cuts were much sharper than the Linde precut microspheres. One of the cuts of greatest interest, 4.2 microns diameter (No. 4868-66), was then successfully used in the fabrication process. The properties of this powder as well as details of the classification and evaluation of the 40 lbs. of microspheres are described in Appendix III.

The work described above indicates that highly classified spherical tungsten powder at least as small as 4.2 microns diameter can be successfully fabricated by a direct forming process. During this program over 40 fabrications were made totaling about 1200 linear inches of material. Not all of these fabrications were completely successful and in many instances none of the material was sintered; however, sufficient finished material was made to adequately demonstrate the capability of the process. One sample of the ionizer material made from the Linde precut 4.8-micron powder was tested for ionizing characteristics at TRW Systems and found to be comparable to material made by TRW from a similar powder (4).

Additional photographs of shapes made by the direct forming method are shown in figures 3 and 4. In addition to the shapes shown here, rectangular shapes having cross sections of approximately 1 in. x 1/16 in., 1 in. x 1/8 in., and 2-1/4 in. x 1/8 in. and lengths up to 6 in. have been fabricated.

The sintering of all of the shapes described in the preceding sections is discussed in Section III, Sintering. Evaluation of ionizer materials made by this method is described in Section V, Ionizer Evaluation.

III. SINTERING

Low Temperature Sintering

The shaped samples were first sintered in tank hydrogen at 1200°C. for 1 hour followed by 15 minutes sintering in dry hydrogen. In all cases molybdenum boats were used as setters to support the tungsten samples. Radiation shielding was employed over the samples to protect them from excessive radiation from the furnace muffle. A slow heat-up rate was used generally at the early stages up to about 300°C., after which the sample was heated to a maximum temperature of 1200°C. in 2 to 3 hours. After the sintering cycle was completed the sample was pulled into a water-cooled cooling zone where it was held for approximately 30 minutes before it was removed from the furnace.

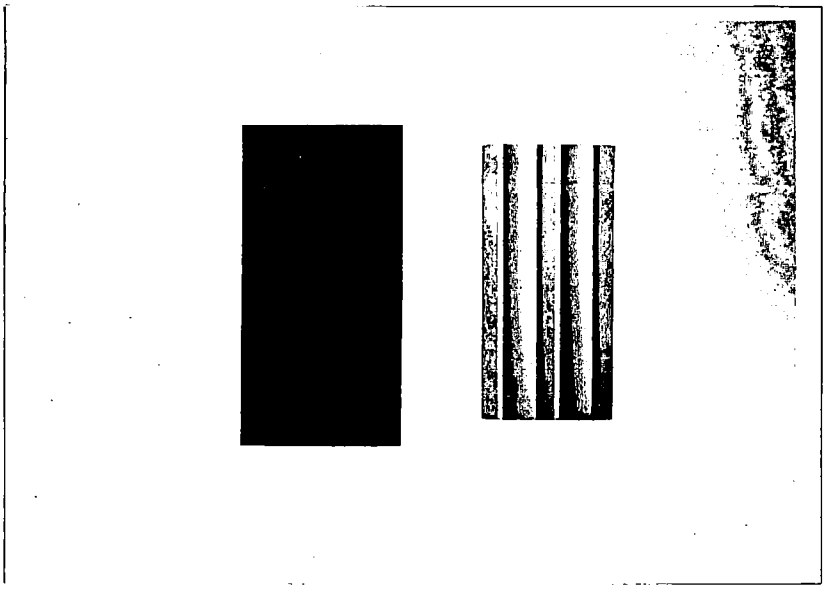

1 X A-2146

IONIZER SHAPE PRODUCED BY DIRECT FORMING
TOP VIEW - AS FORMED (LEFT) AND
SINTERED AT 1900°C. (RIGHT)

Figure 3

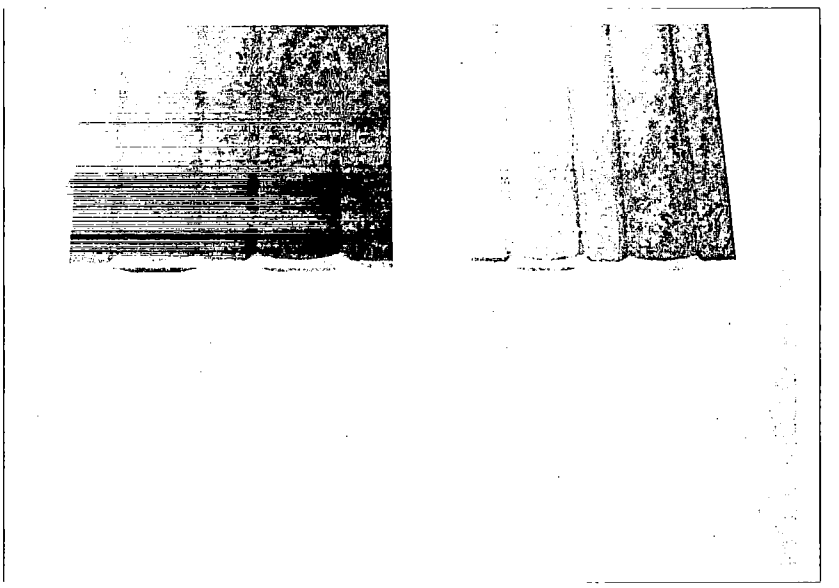

2.1 X A-2147

IONIZER SHAPE PRODUCED BY DIRECT FORMING
END VIEW - AS FORMED (LEFT) AND
SINTERED AT 1900°C. (RIGHT)

Figure 4

High Temperature Sintering

Most of the high temperature sintering was done in a Brew Model 905 horizontal side loading furnace having a 4- x 6- x 12-in. hot zone with a tungsten mesh heating element. Some sintering was done in a smaller Brew Model 424B furnace, with tungsten mesh heating elements using a 4-1/2- x 7-in. hot zone for temperatures to 2500°C. in hydrogen and a 3- x 6-in. hot zone for temperatures up to 2800°C. in hydrogen. Because of their vacuum design both of these furnaces are capable of providing very pure hydrogen atmospheres. A picture of the side loading furnace with the fixtures in place is shown in figure 5. In operation the furnace is first evacuated to 10^{-5} Torr, then back-filled with helium and re-evacuated in order to minimize contamination from oxygen and other gases. Hydrogen is then bled into the furnace up to 1 in. of oil pressure. The hydrogen employed is purified by a Serfass palladium alloy diffusion purifier which removes impurities to the level of less than 10 ppm. The purity of the hydrogen produced by these purifiers has been verified by mass spectrometry. After the pure hydrogen has been admitted, the sample is then heated to 1800° to 2000°C. in about 45 minutes. The heating rate varies considerably with the material being sintered. The sample is then cooled in hydrogen after which the hydrogen is evacuated and the furnace is pumped to 10^{-5} Torr before the sample is removed.

The furnacing fixtures used in sintering most of the samples are shown in figures 6 and 7. The parts consist of 1/4 in. thick ground tungsten plates. The samples can be sintered in a variety of ways using these fixtures; they can be laid flat on one of the plates or they can stand vertically on an edge between two plates. There is also provision for sintering samples at varying angles of repose.

Sintering samples at 2000°C. on tungsten gives some sticking and distortion problems. Another method which avoids these problems is to suspend them from a wire or rod. This requires that a hole be drilled in the sample in order to suspend it; thus, it is necessary to provide additional length for the hole and this material must be removed after sintering. Secondly, it requires more space and thus limits the length of the sample which can be sintered.

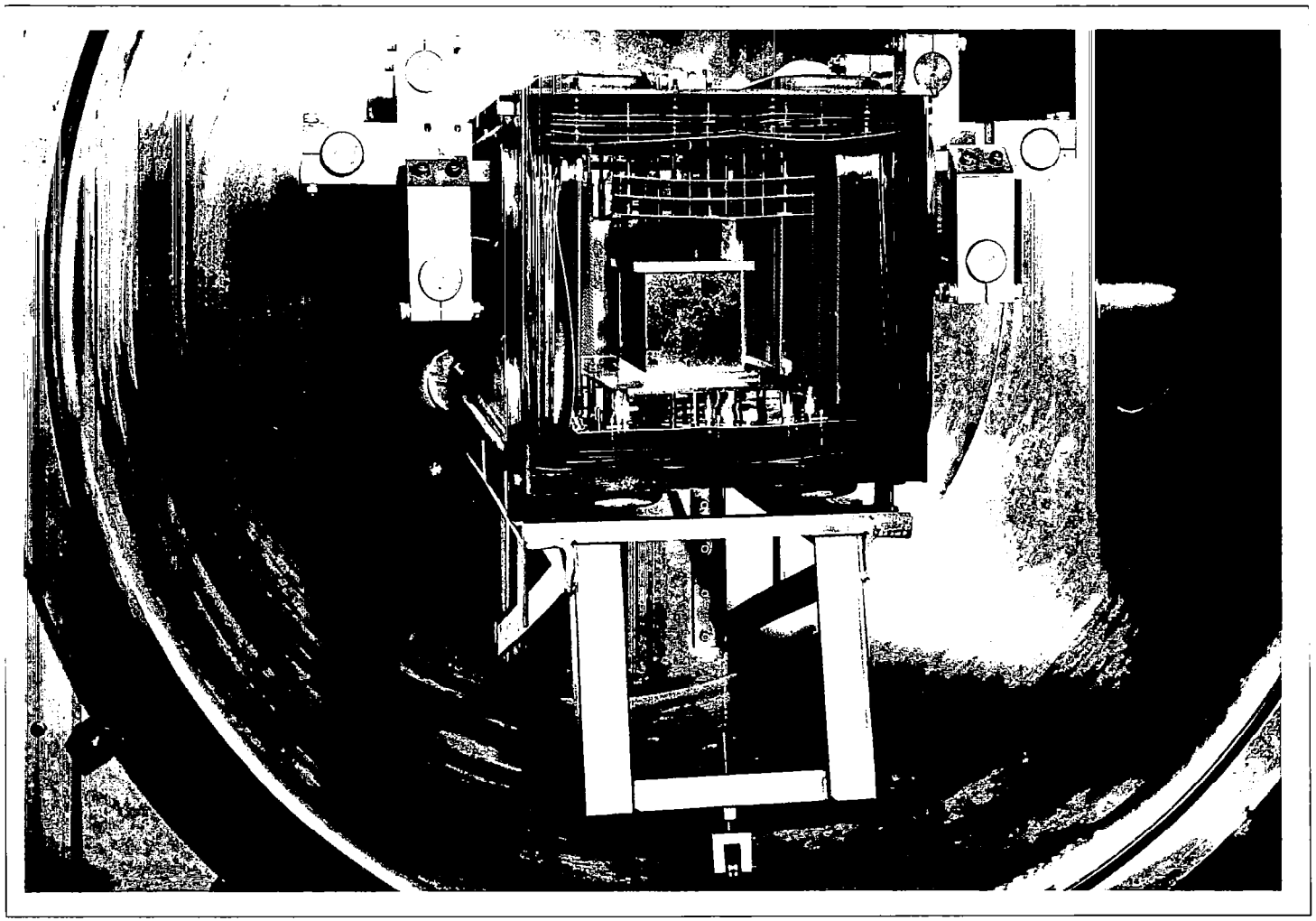

HIGH TEMPERATURE VACUUM - HYDROGEN SINTERING FURNACE

Figure 5

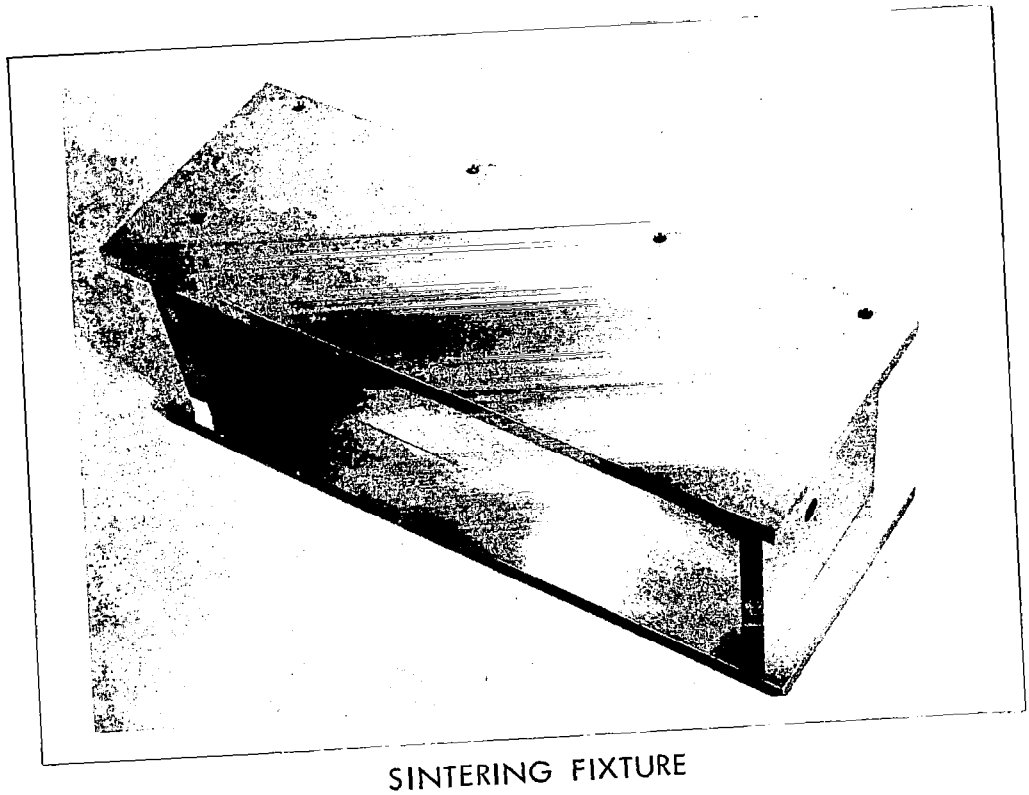

SINTERING FIXTURE

Figure 6

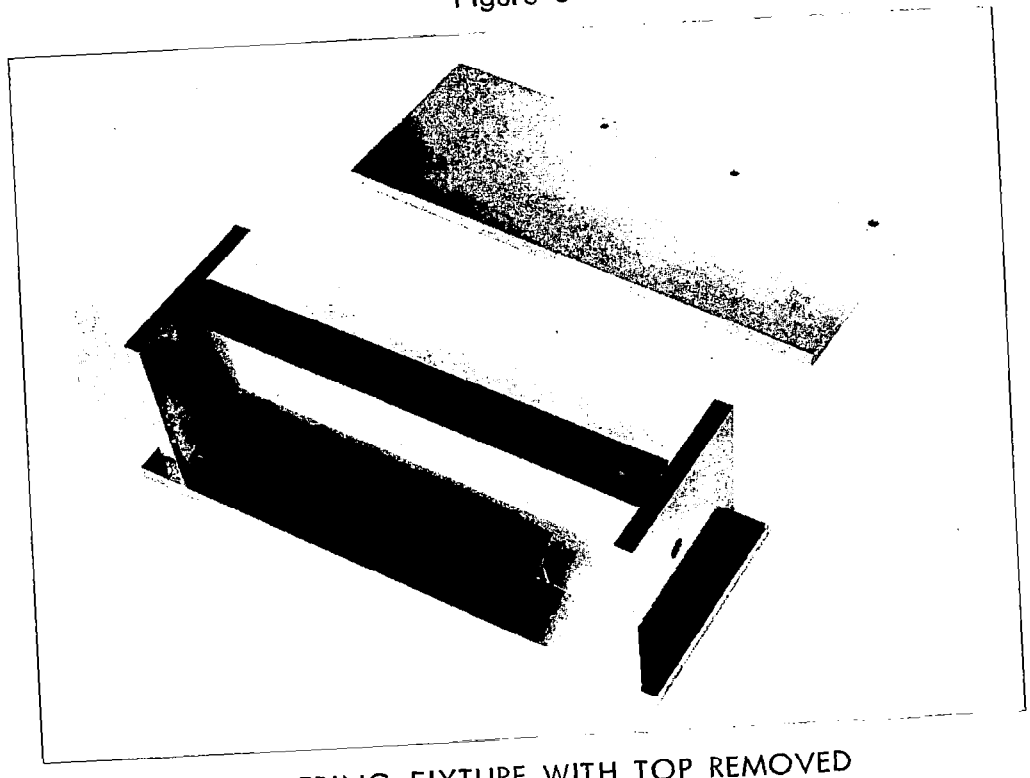

SINTERING FIXTURE WITH TOP REMOVED

Figure 7

The sintering data summary for flat shapes made by the direct forming process is shown in table II. Permeability data and a pore diameter calculated from the permeability, where available, is also shown. All of the samples were sintered on edge between tungsten plates, as described above. The powders from which these samples were made are described in Section VI, Materials Selection. Other samples, not shown here, were sintered to 80% of theoretical density and higher. The sintering rate data are also shown in figure 8.

Shrinkage

The dimensional uniformity of the sintered shape and its relation to the as-formed shape is shown in table III and is demonstrated graphically in figure 9. Note that in this modification the side tabs were increased in length from the original dimensions shown in figure 1. Thus the formed width was 0.870 in. instead of 0.744 in., and the half-width was 0.435 in. instead of 0.372 in. The shape was formed directly to the dimensions of the Hughes design, with the modifications just described with no provision made for sintering shrinkage since it was felt that once the feasibility of the direct forming method was shown, that scale-up to required dimensions would present no particular problems.

Special Techniques

In order to test the possibility of sintering on graphite and avoiding some of the problems associated with sticking and distortion on tungsten fixtures, sintering was done on an experimental basis in the vacuum hot press. In this case major consolidation was achieved on graphite setters. No sticking was observed and samples were sintered in both the flat and vertical positions. The carbon or carbides which are picked up by the material in sintering in graphite is then removed by further sintering in hydrogen. Another application of the vacuum hot press is in the straightening or flattening of distorted samples. This is found to be very effective on samples which had been cupped or bowed by too rapid sintering in the conventional hydrogen sintering furnace, or samples which have been isostatically pressed and sintered. At 1500°C., less than 1000 psi. is required to straighten samples of the types

TABLE II

SINTERING DATA SUMMARY FOR IONIZER MATERIAL MADE FROM SPHERICAL TUNGSTEN POWDER

Sample Number	Powder	Sintering*** Conditions		Density, Percent of Theoretical	Flow Data	
		Temp., °C.	Time, hr.		Permeability x 10^5, g/cm/sec/mm Hg	Pore Diameter, microns
4927-49-2	Linde-14*, 4.2 μ	2000	1	71.1	--	--
4927-49-1	Linde-14*, 4.2 μ	2000	2	74.7	--	--
4927-49-3	Linde-14*, 4.2 μ	2000	4	78.5	--	--
4927-46-4	Linde-16*, 4.8 μ	2000	1	69.7	0.0415	1.94
4927-48-2	Linde-16*, 4.8 μ	2000	2	70.9	0.0390	2.04
4927-48-7	Linde-16*, 4.8 μ	2000	4	72.9	0.0316	1.96
4927-46-2	Linde-18*, 5.8 μ	2000	1	67.4	0.0587	2.32
4927-49-4	Vortec Cut-66**, 4.2 μ	2000	1	74.4	--	--
4927-49-5	Vortec Cut-66**, 4.2 μ	2000	2	77.1	--	--
4927-48-8	Vortec Cut-66**, 4.2 μ	2000	4	78.7	--	--

*Linde Microspheres, purchased as classified fractions, Lot 2044-6.

**Classified cut by Vortec Products Company from 40 lbs. of Linde Microspheres, Lot 2044-27.

***All sintering in pure hydrogen.

SECRET

DWG. NO. G-66-601

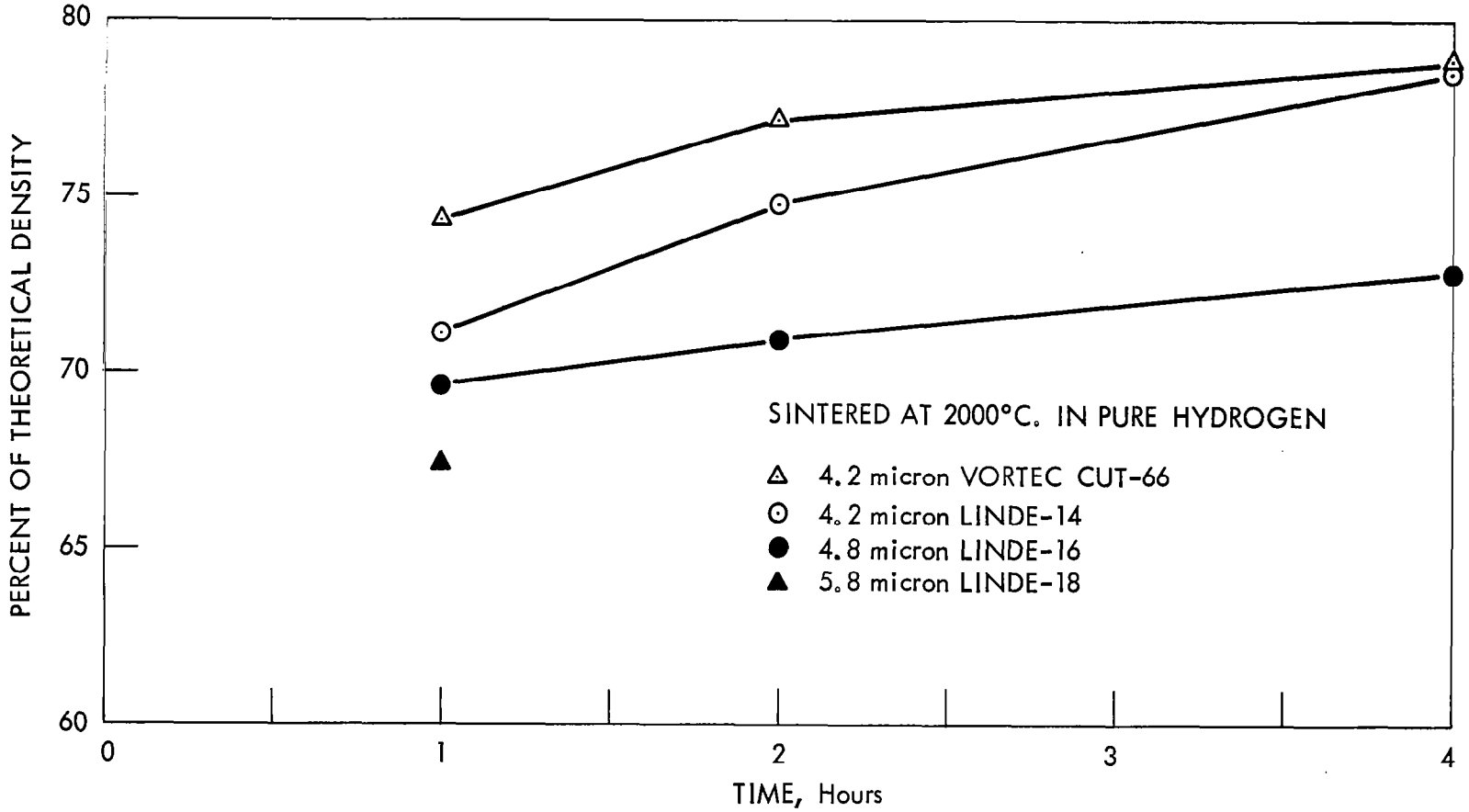

SINTERING RATE OF POROUS TUNGSTEN MADE FROM MICROSPHERES

Figure 8

TABLE III

DIMENSIONAL SHRINKAGE IN IONIZER SHAPE

Dimension, inches		Shrinkage,
As-Formed	Sintered	percent
0.1876	0.143	23.8
0.1406	0.107	23.7
0.0775	0.0585	24.5
0.2975	0.229	23.0
0.4350*	0.3337	23.3
0.870**	0.664	23.7

*Originally 0.3720 in Hughes design.

**Originally 0.7440 in Hughes design.

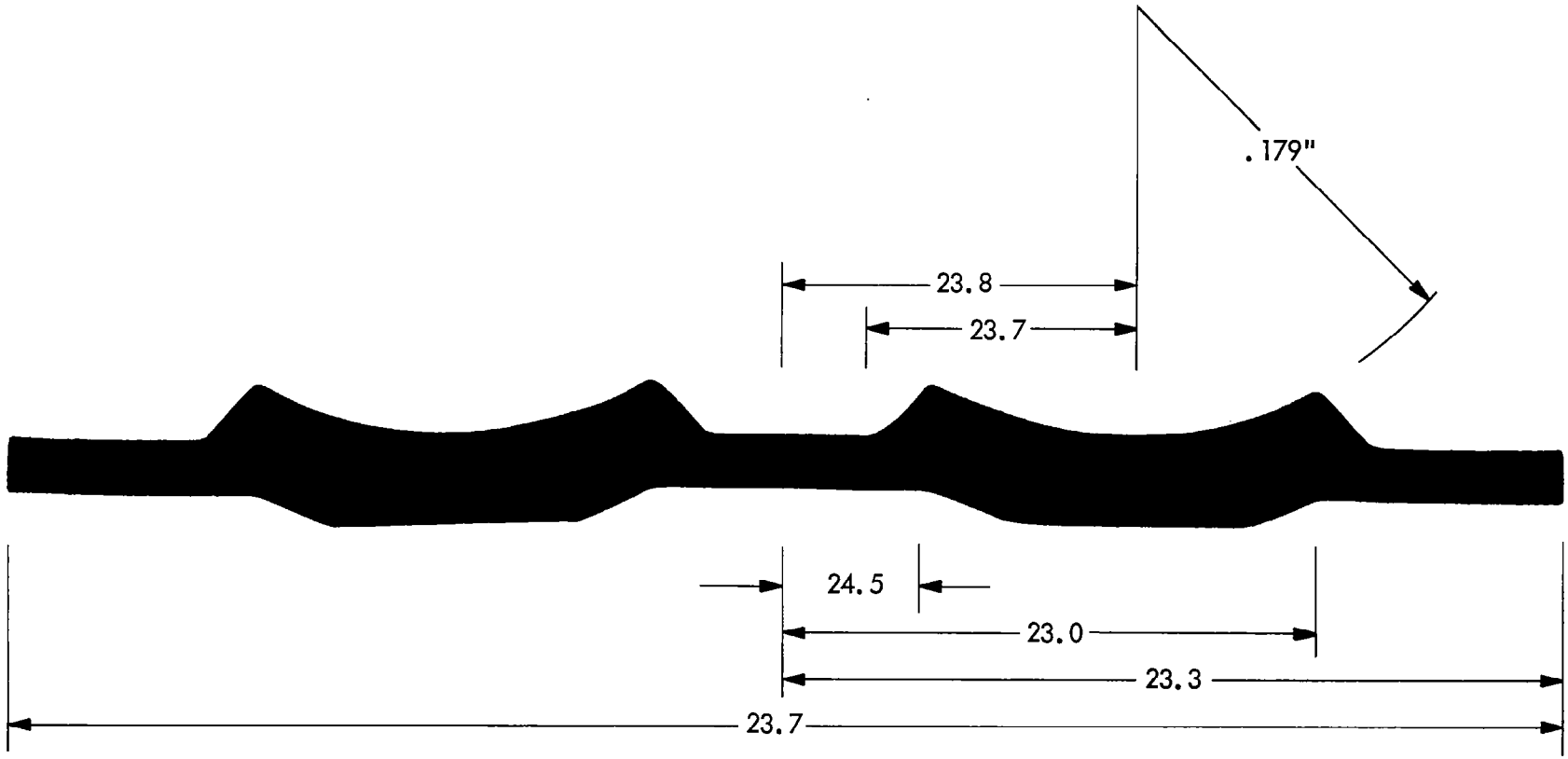

MAGNIFICATION 13.8X

NOTES: (1) Numbers at various dimensions (except radius) are percent shrinkage values from initial forming to final sintering, measured on an optical comparator.

(2) Radius shown is actual value in inches, measured on an optical comparator.

PERCENT SHRINKAGE AT VARIOUS DIMENSIONS ON ACTUAL CROSS-SECTION OF SHAPE PREPARED BY DIRECT FORMING AND SINTERING

Figure 9

developed in this program. Figure 10 is an exterior view of the hot press. In figure 11, the hot press is shown with the door open, revealing the induction coil, the quartz heat shield and the susceptor arrangement.

IV. HOT PRESSING

The second approach to ionizer fabrication was hot pressing and sintering. The object of this approach was to load a formed shape die with a preform of originally good uniformity. In this process, advantage is taken of the simultaneous application of heat and pressure to permit the tungsten particles to move to their closest possible relative positions of close packing. The application of the pressure at relatively low temperatures achieves better uniformity since the final uniformity of a sintered structure is determined largely by its uniformity prior to the application of heat in the temperature range at which fairly rapid diffusion and consolidation occur. The hot pressing is followed by high temperature sintering in hydrogen to achieve final dimensions and properties and to remove carbon. This process may be applicable only to flat samples for this particular application. It has been demonstrated only with flat samples during this contract period. With further development it may possibly be used on shapes also. One other limitation is that it may provide directional uniformity only since the sample is restricted to move only in thickness rather than in all directions as is achieved by isostatic pressing. This is not expected to be a serious problem.

Tamped Powder Loading

The feasibility of forming shapes by hot pressing was first shown by tamped powder loading. This initial hot pressing of a shape was done in a prototype die which was fabricated in the early stages of the contract period before the drawings of the Hughes ionizer shape were available and was intended only to give preliminary information about powder loading, pressing parameters and problems which might be encountered. A photograph of the prototype die components and the assembled die and

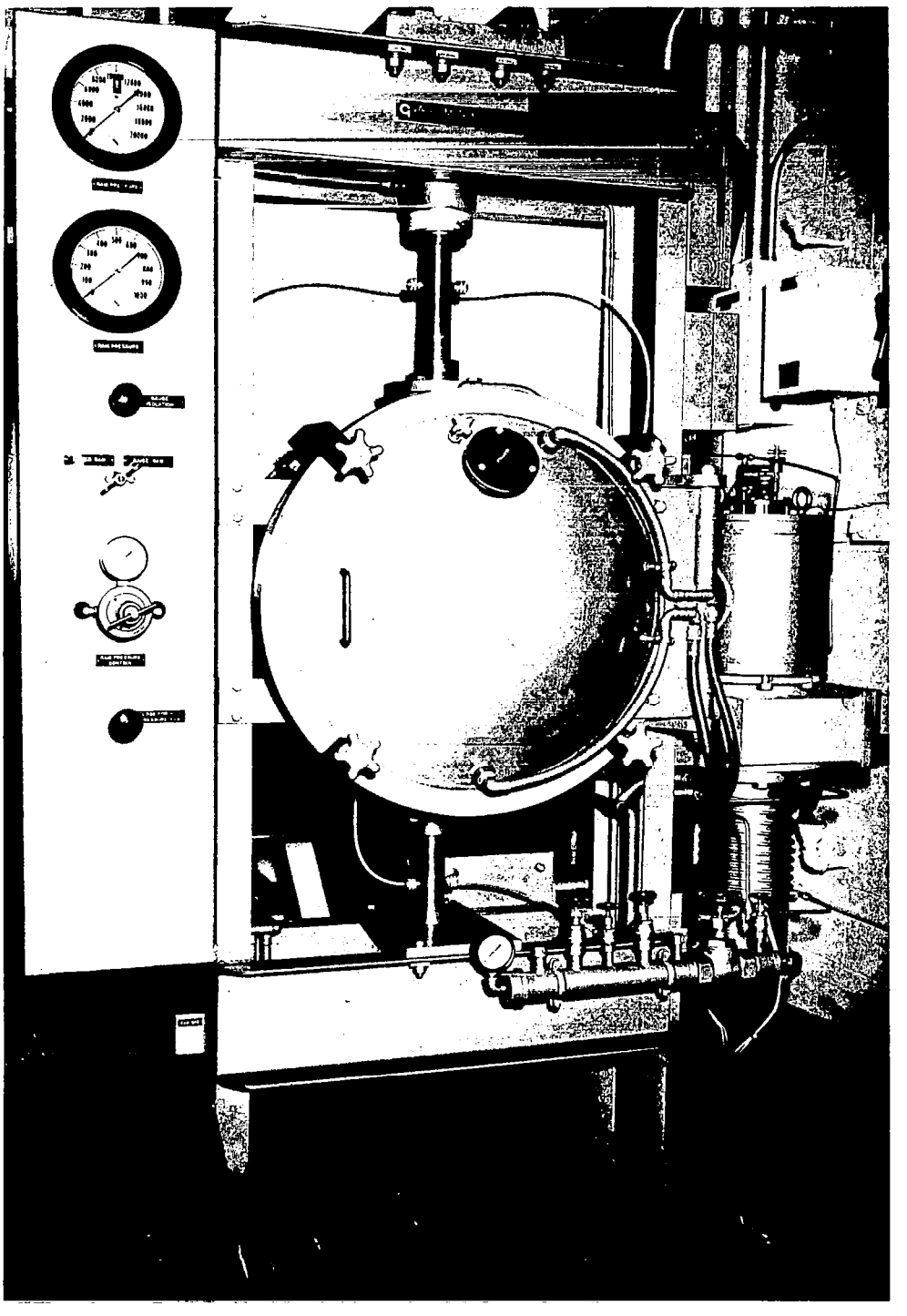

VACUUM HOT PRESS
Figure 10

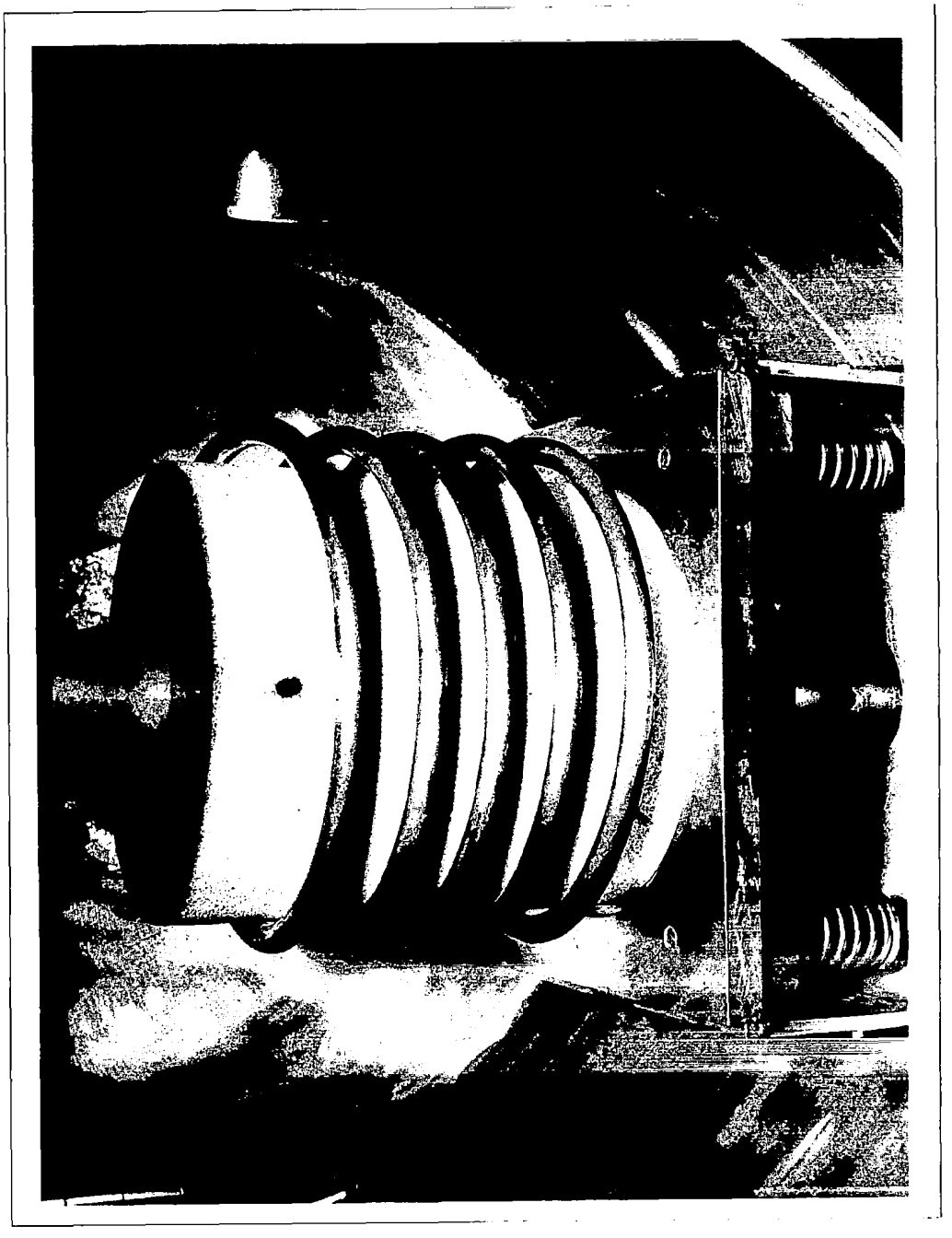

INTERIOR VIEW OF VACUUM HOT PRESS
Figure 11

retainer-susceptor is shown in figures 12 and 13. This die did not work successfully because the angles were too severe and the tungsten samples upon cooling gripped the edges of the graphite die and could not easily be removed. Although no complete shapes were obtained using this die, valuable information was obtained which demonstrated the feasibility of the method and aided in the design of the die for the Hughes design. Figure 14 shows one of the tungsten shapes on the die base before removal was attempted. Later in the contract period, a method for removing shapes of this type was developed.

Figure 15 is a drawing of the tungsten ionizer die assembly of the modified Hughes design. This die was found to work particularly well with angular powder. The completed die is shown in figure 16. Shown in figure 17 is a rectangular die of similar design for pressing rectangular, flat samples. The hot-pressing technique worked very well for angular powder and it was possible to press packs to close to the desired density and thickness and also possible to remove them from the die. They did, however, vary in density and thickness along their length. This process did not work well with spherical powder for several reasons. One of the reasons was the poor bonding associated with spherical powders as described previously. Secondly, the free flowing powder entered crevices in the die, thus contributing to flash formation. This flash then gripped the sides of the die so that the pack stuck to the rams. In some cases it was possible to break the pack loose but in most cases it was necessary to sacrifice the die by a hydrogen treatment which removed the graphite successfully. Disc packs of various types were made very successfully with this technique. It was possible because of the inherent nonuniformity achieved by the powder tamping to produce samples which were very useful for demonstrating nonuniformities in flow tests. Figure 18 shows one of the hot-pressed ionizer shapes made from angular powder. Figure 19 shows two of the shapes as-pressed and three samples after sintering in hydrogen.

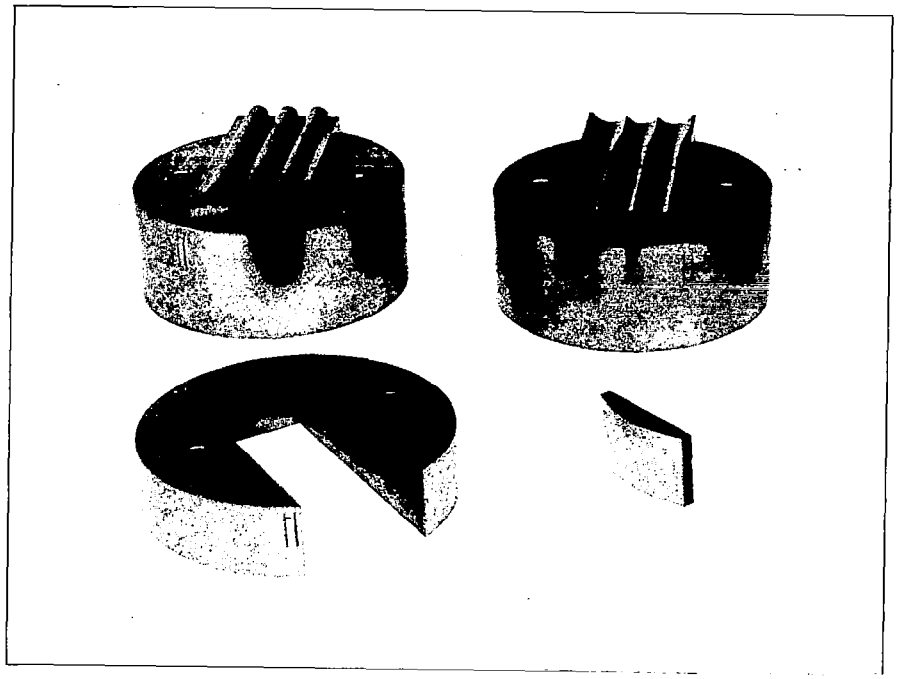

PROTOTYPE DIE COMPONENTS
Figure 12

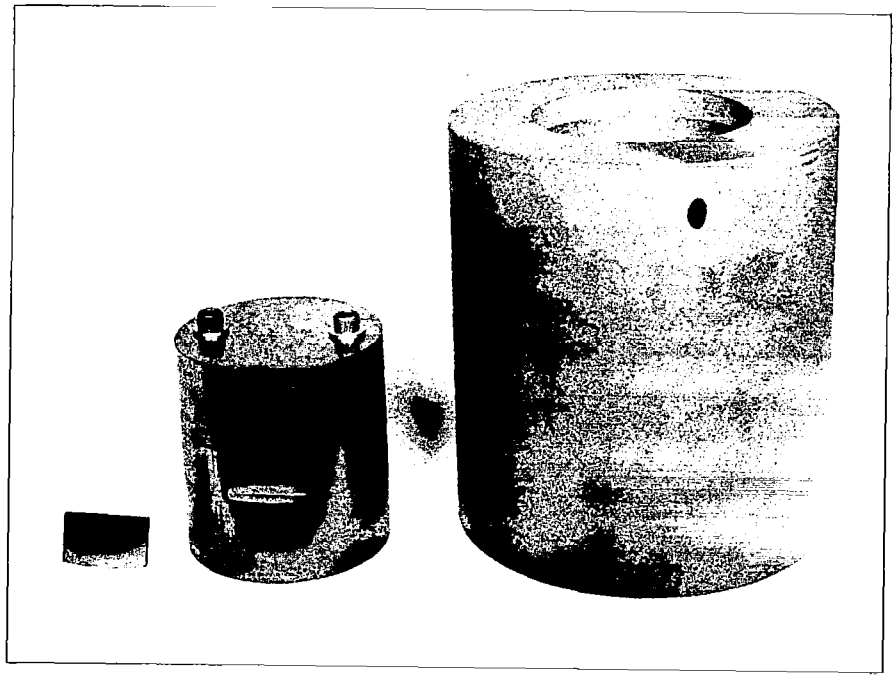

ASSEMBLED DIE AND RETAINER-SUSCEPTOR
Figure 13

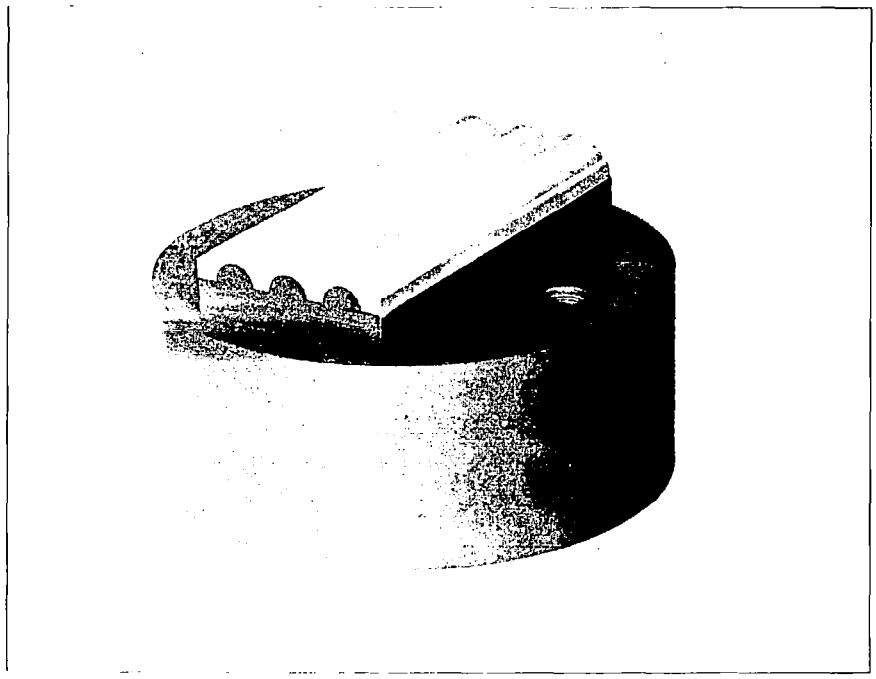

HOT PRESSED SAMPLE ON DIE BASE
Figure 14

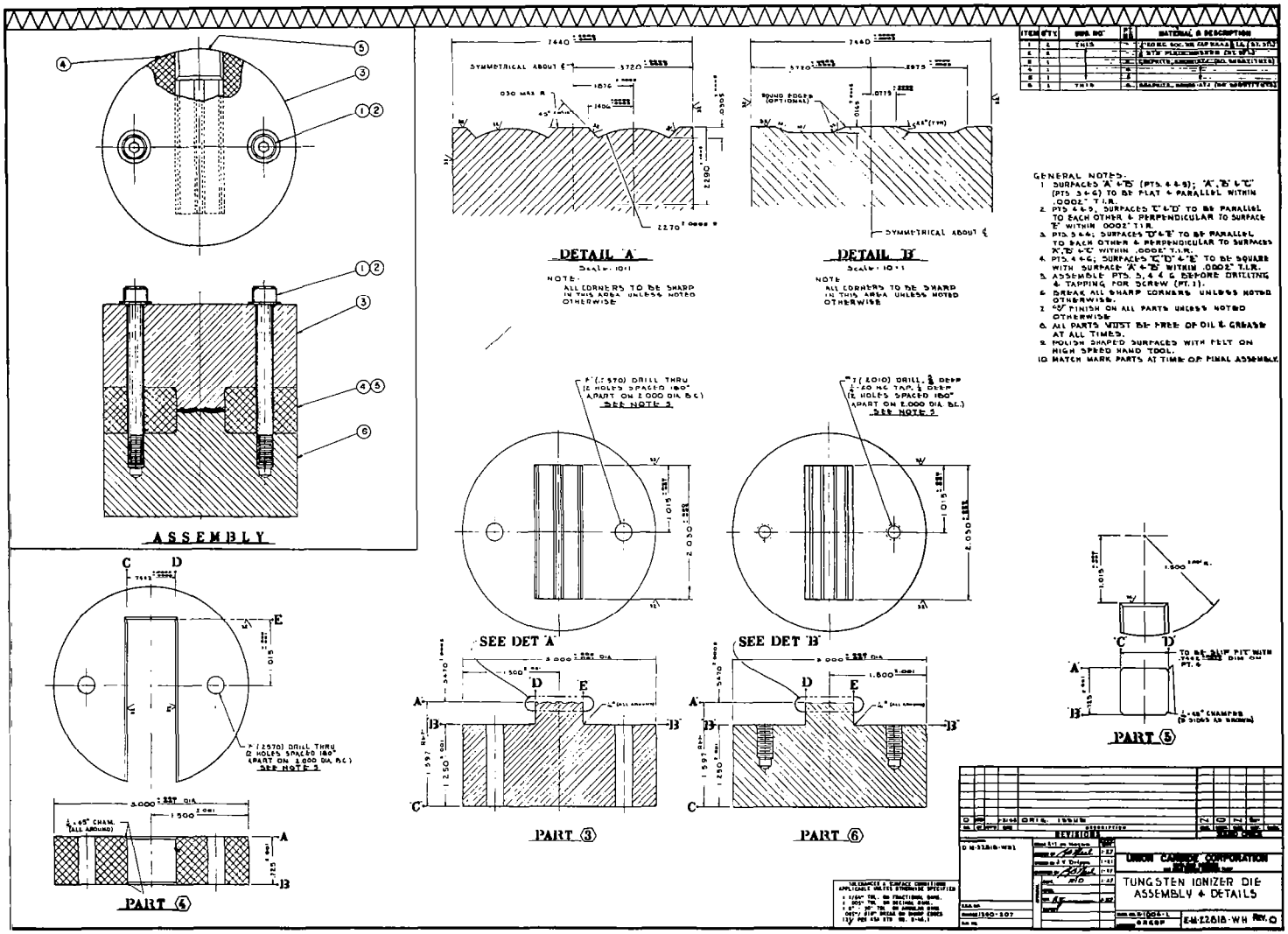

TUNGSTEN IONIZER DIE ASSEMBLY AND DETAILS

Figure 15

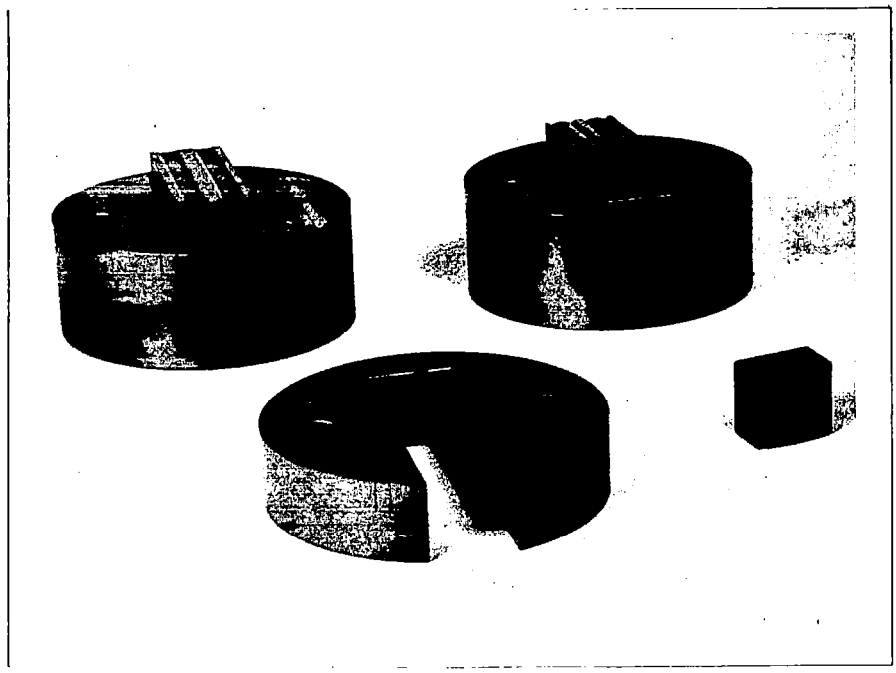

2-STRIP IONIZER DIE
Figure 16

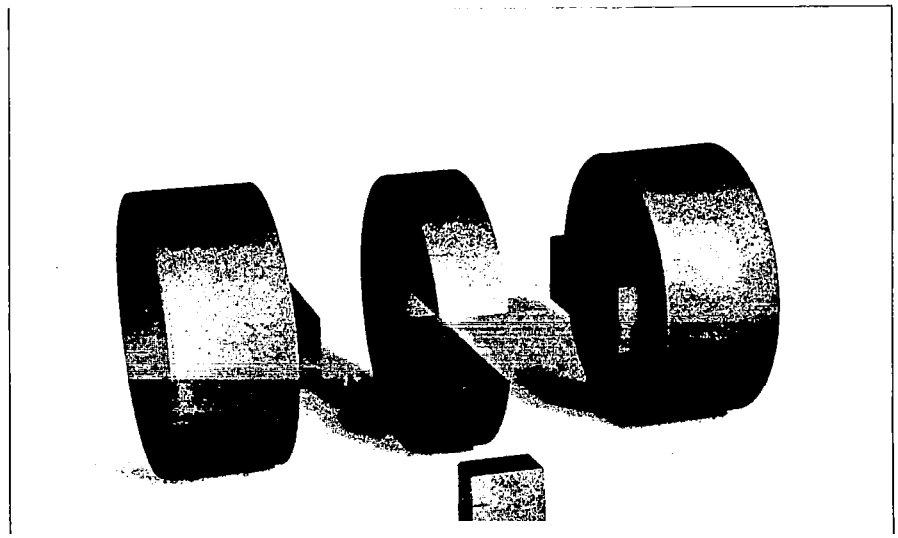

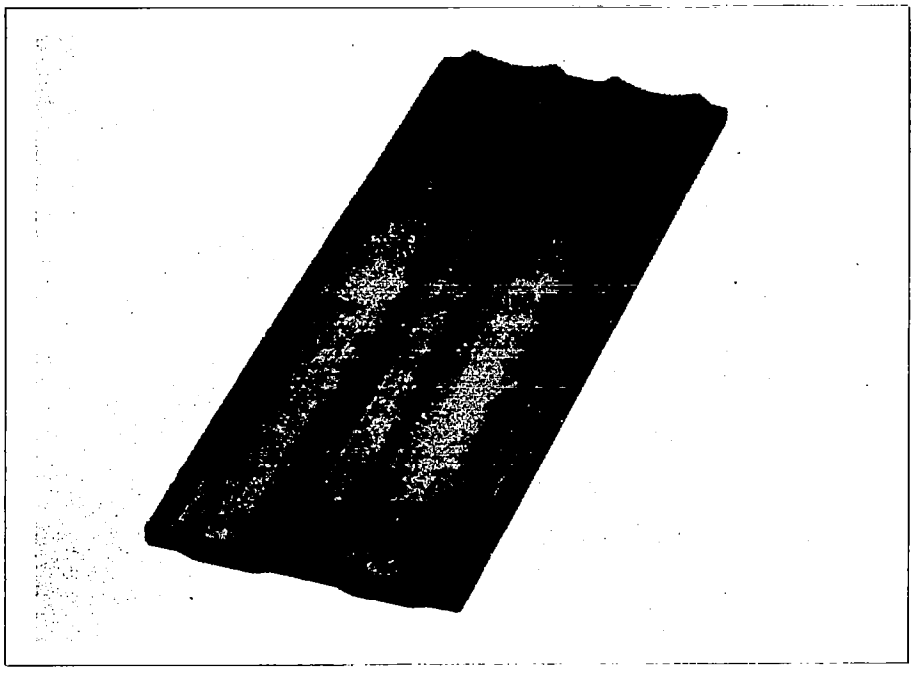

HOT PRESSED SHAPE

Figure 18

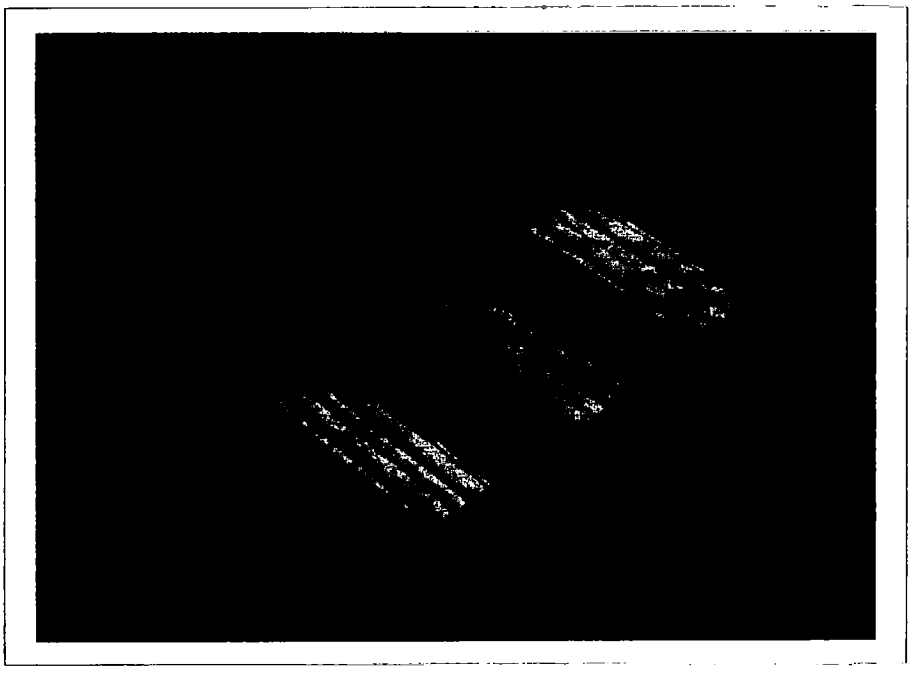

HOT PRESSED SHAPES, BEFORE (TOP)
AND AFTER (BOTTOM) SINTERING

Figure 19

Preforms

The hot-pressing technique was not emphasized after success had been achieved by the direct-forming method. In the latter stages of the contract period, however, preforms became available which could be used in hot pressing. It was found that by this method, hot-pressed samples could be successfully made from any powder. These preforms were presintered to size in order to fit the dies properly. They were then pressed at 1500°C. and 8000 psi. No sticking problems were encountered and spherical powder was found to press just as well as the angular powder. This technique has been used only for flat samples; however, it might well be used for shaped samples although there are some problems inherent in this method.

Carbon Removal

During the course of the hot-pressing work it was demonstrated that carbon or carbides can be readily removed by high temperature sintering in high purity hydrogen. Carbon has always been considered a problem in that ionizers containing high percentages of carbon have been less efficient in their ionizing characteristics due to a lowered work function. Hydrogen sintering by the method described previously has been shown to remove carbon down to a level of less than 10 ppm. In order to demonstrate this, packs were pressed at varying thickness and the percentage of carbon in them was determined. Alternate packs were then sintered in hydrogen at up to 2000°C. and carbon again determined. Hydrogen sintering was found to remove the carbon to less than 10 ppm. in all cases but one and in some cases to less than 5 ppm. with no apparent dependence of the carbon level on sample thickness. These results are shown in figure 20. This result is particularly important in that it demonstrates that the residual carbon is not concentrated at the sample surface; for if it were, the thinner samples should show higher percentages of carbon.

DWG. NO. G-66-602

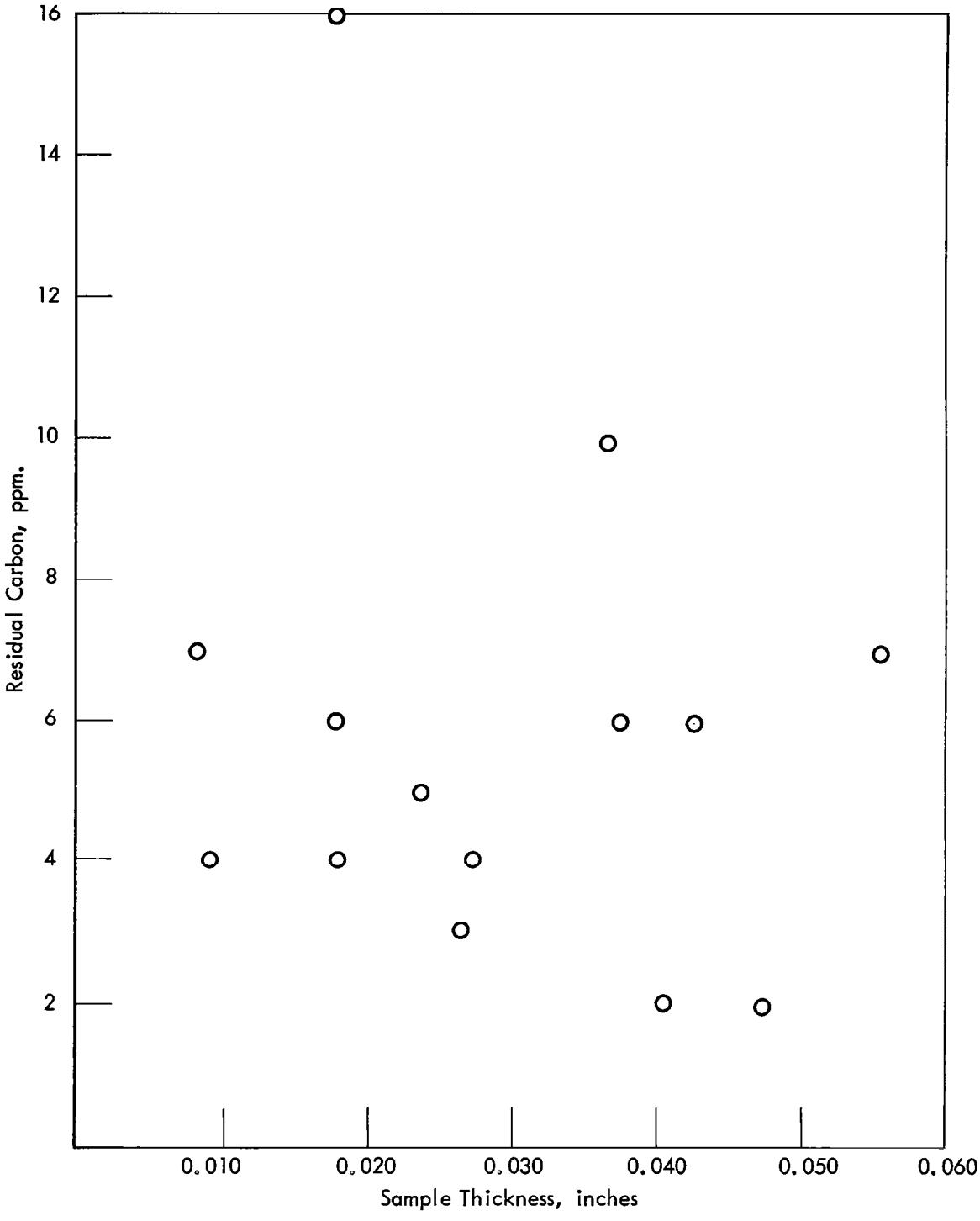

RESIDUAL CARBON VS. SAMPLE THICKNESS
Figure 20

Variations in Technique

During this work it was also demonstrated that hydrogen reduction can be used to release packs which are stuck to rams, thus conserving an otherwise acceptable sample. It was also shown that in some cases pyrolytic graphite foil liners can be used to protect the rams. Thus, if the pack sticks, it sticks only to an inexpensive disc of 0.005 in. foil, which can be burned off in hydrogen.

Die inserts of tantalum and molybdenum foil were also used to attempt to prevent formation of carbides. While this technique has some applications, it was felt that the etching procedure used to remove the foil liner would result in excessive contamination.

A summary of the hot-pressing data obtained using tamped powder loading is shown in table IV. The data obtained on the samples which were hot-pressed from preforms are summarized in table V. Representative hot-pressed flats were also evaluated in regard to pore size and flow properties. A summary of this evaluation is included in Section VI, Ionizer Evaluation. The data are tabulated in comparison with other ORGDP samples made by direct forming and with samples made by EOS, TRW, and Hughes. The samples hot-pressed from preforms are very uniform as seen by the flow and bubble test data and their pore size approached that of the design criteria; however, the permeability is somewhat lower than that obtained on sintered material made from the same powder.

V. IONIZER EVALUATION

In addition to the development and fabrication of porous tungsten ionizer materials, the contract called for evaluation of the materials and processes under Tasks I and II using the tests and techniques as listed in the Introduction. It was understood also that the tests should not necessarily be limited to those which were listed in the contract.

This section summarizes the results of tests obtained on various materials fabricated during the course of the program and compares their properties with those of ionizers fabricated by other contractors.

TABLE IV

HOT PRESSING SUMMARY

				Pressing Conditions				Sintering Conditions			
Powder Pack	Powder*	Die Type	Inserts	Temperature, °C.	Pressure, psi	Time, min.	Relative Density, %	Relative Density, %	Temperature, °C.	Time, min.	Remarks
10-11-12-13	FSU-3.0 μ	Prototype	--	963	3250	5	66.48		1900	60	Broken
14-15-16-17	FSU-3.0 μ	Prototype	--	1017	6000	45	49.58		--	--	Broken
18-19	FSU-3.0 μ	Prototype	--	1057	6000	45	50.70		--	--	Broken
22-23	FSU-3.0 μ	Prototype	--	1260	6000	5	65.43		2000	60	Broken
24-25	FSU-3.0 μ	1 in. disc	--	1404	3000	49	68.00		--	--	Broken
26-27	FSU-3.0 μ	1 in. disc	--	1431	3000	6	--		--	--	Broken
30-31	FSU-3.0 μ	1 in. disc	--	1448	3000	110	--		--	--	Broken
34-35	FSU-3.0 μ	Prototype	--	1016	6000	34	--		--	--	Broken
36-37	FSU-3.0 μ	Prototype	--	1260	6000	127	--		--	--	Broken
38-39	G.E.-8, 9.1 μ	1 in. disc	Molybdenum	1007	6000	35	--		--	--	Broken
40-41	G.E.-2, 6.5 μ	1 in. disc	Molybdenum	1106	6000	30	61.38		--	--	Broken
42-43	G.E.-2, 6.5 μ	1 in. disc	Molybdenum	1163	6000	5	61.17		--	--	Broken
50-51	FSU-3.1 μ	Rectangular	--	1249	6000	31	60.12		--	--	Good
52-53	FSU-3.1 μ	Rectangular	--	1243	8000	30	69.44		--	--	Good
54-55	FSU-3.1 μ	Rectangular	--	1236	8000	30	64.87		--	--	Good
58-59	G.E.-8, 9.1 μ	Rectangular	--	1241	8000	35	--		2000	60	Broken
60-61	FSU-3.1 μ	Ionizer	--	1249	8000	30	--		1800	60	Good
62-63	FSU-3.1 μ	Ionizer	--	1249	8000	30	--		1800	60	Good
64-65	FSU-3.1 μ	Ionizer	--	1246	8000	30	--		--	--	Good
66-67	L-14, 4.2 μ	Ionizer	--	1243	8000	30	--		--	--	Broken
68-69	L-14, 4.2 μ	Ionizer	--	1004	8000	30	--		2000	60	Broken
70-71	L-14, 4.2 μ	Rectangular	--	1106	8000	30	--		--	--	Broken
72-73	FSU-3.1 μ	2 in. disc	--	1241	8000	4	--		1800	60	--
76-77	L-14, 4.2 μ	1 in disc	Moly-Lower Tant-Upper	1260	6000	30	--		--	--	Broken
78-79	L-14, 4.2 μ	Rectangular	Molybdenum	1240	8000	30	--		--	--	Broken
80-81	FSU-3.1 μ	2 in. disc	--	1249	8000	30	57.50		1800	60	Good
84-85	L-14, 4.2 μ	1 in. disc	Tantalum	1506	8000	30	77.20		1800	60	Good
86-87	L-14, 4.2 μ	1 in. disc	Molybdenum	1506	8000	30	--		--	--	--
90-91	FSU-3.1 μ	1 in. disc	--	1299	8000	30	64.82	77.90	1800	60	Good
92-93	FSU-3.1 μ	Ionizer	--	1304	8000	30	65.99	76.60	1800 2000	60	Good
94-95	L-14, 4.2 μ	1 in. disc	--	1507	8000	30	70.73		1800	60	Broken
96-97	L-14, 4.2 μ	1 in. disc	--	1499	8000	30	--		1800	60	Broken
100-101	L-14, 4.2 μ	1 in. disc	--	1502	8000	30	70.66	78.70	1800 2000	60	Broken
102-103	FSU-3.1 μ	Ionizer	--	1250	8000	30	--	72.80	1800 2000	60	Broken
104-105	L-14, 4.2 μ	1 in. disc	--	1504	8000	30	62.21		1800	60	Good
106-107	L-14, 4.2 μ	2 in. disc	--	1521	8000	30	68.57	72.64	1800	60	Good
108-109	L-14, 4.2 μ	Ionizer	--	1502	8000	30	71.92		1800	60	Good
110-111	L-18, 5.8 μ	1 in. disc	--	1502	8000	30	72.45		1800	60	Good
112-113	L-14, 4.2 μ	Ionizer	--	1499	8000	30	72.60		1800	60	--
114-115	L-14, 4.2 μ	1 in. disc	--	1505	8000	30	--		1800	60	Broken
116-117	L-14, 4.2 μ	1 in. disc	--	1504	8000	30	--		--	--	Broken
118-119	L-14, 4.2 μ	Rectangular	--	1501	8000	30	--		2000	60	Broken
120-121	L-14, 4.2 μ	1 in. disc	--	1510	8000	30	74.95		1800	60	--
122-123	L-14, 4.2 μ	Rectangular	--	1510	8000	30	--		--	--	--
124-125	L-14, 4.2 μ	1 in. disc	--	1510	8000	30	74.75		1800	60	--
126-127	FSU-3.1 μ	1 in. disc	--	1254	8000	30	--	80.20	1800	60	Good

TABLE IV

HOT PRESSING SUMMARY (Continued)

Powder Pack	Powder*	Die Type	Inserts	Pressing Conditions: Temperature, °C.	Pressing Conditions: Pressure, psi	Pressing Conditions: Time, min.	Pressing Conditions: Relative Density, %	Sintering Conditions: Relative Density, %	Sintering Conditions: Temperature, °C.	Sintering Conditions: Time, min.	Remarks
128-129	FSU-3.1 μ	1 in. disc	--	1250	8000	30	56.32		1800	60	Good
130-131	FSU-3.1 μ	1 in. disc	--	1250	8000	30	57.75		1800	60	Good
132-133	FSU-3.1 μ	1 in. disc	--	1249	8000	30	56.85		1800	60	Good
136-137	FSU-3.1 μ	1 in. disc	--	1249	8000	30	--		--	--	Broken
142-143	FSU-3.1 μ	1.75 in. disc	--	1260	8000	30	56.45		--	--	--
144-145	FSU-3.1 μ	1 in. disc	--	1260	8000	30	58.24		1800	60	Good
148-149	FSC-3.2 μ	1 in. disc	--	1257	8000	30	--		--	--	Broken
150-151	FSC-3.2 μ	1.75 in. disc		1251	8000	30	61.27		--	--	--
152-153	FSC-3.2 μ	1 in. disc	--	1507	8000	30	--		--	--	Broken
154-155	FSC-3.2 μ	1.75 in. disc	--	1251	8000	30	58.30		1800	60	--
156-157	FSC-3.2 μ	1 in. disc	--	1254	8000	30	60.74		1800	60	Good
158-159	FSC-3.2 μ	1 in. disc	--	1257	8000	30	63.06		1800	60	Good
160-161	FSC-3.2 μ	1.75 in. disc	--	1251	8000	30	58.93		--	--	--
162-163	FSC-3.2 μ	1 in. disc	--	1260	8000	30	58.19		1800	60	Good
164-165	FSC-3.2 μ	1.75 in. disc	--	1249	8000	30	--		--	--	Broken
166-167	FSC-3.2 μ	Rectangular	--	1249	8000	30	63.50		1800	60	--
172-173	FSC-3.2 μ	1 in. disc	--	1251	8000	30	61.35		1800	60	Good
174-175	FSC-3.2 μ	1 in. disc	--	1254	8000	30	58.39		1800	60	Good
178-179	FSC-3.2 μ	1 in. disc	--	1254	8000	30	59.96		1800	60	Good
180-181	FSC-3.2 μ	1 in. disc	--	1254	8000	30	57.08		1800	60	Good
182-183	L-14, 4.2 μ	Rectangular	--	1502	8000	30	66.18		--	--	Broken
184-185	FSC-3.2 μ	1 in. disc	--	1252	8000	30	58.69		1800	60	Good
194-195	L-14, 4.2 μ	Rectangular	--	1649	8000	60	--	80.26	1800	60	Broken
196-197	FSC-3.2 μ	Rectangular	--	1377	8000	30	--	80.02	1800	60	--
198-199	L-14, 4.2 μ	Rectangular	--	1254	8000	120	61.63	68.36	1800	60	--
208-209	L-14, 4.2 μ	Rectangular	Al_2O_3	1499	8000	30	--	--	1200	60	--
222-223	Syl. M-30	1 in. disc	--	1016	8000	30	57.11	57.86	1200	75	--
224-225	L-18, 5.8 μ	Rectangular	Flat Graphite	1501	8000	30	71.06	79.00	2000	60	Good
226-227	L-16, 5.0 μ	Rectangular	Flat Graphite	1621	8000	30	72.11	80.00	1900	60	Good
228-229	L-18, 5.8 μ	Rectangular	Flat Graphite	1616	8000	60	72.69	77.40	1900	60	Good
230-231	L-18, 5.8 μ	Rectangular	Flat Graphite	1499	8000	30	68.87	--	--	--	Good

*Powder Identification

L-14, 4.2 μ - Linde Microspheres, 4.2 μ Dia., ORGDP No. 4868-14.
L-16, 4.8 μ - Linde Microspheres, 4.8 μ Dia., ORGDP No. 4868-16.
L-18, 5.8 μ - Linde Microspheres, 5.8 μ Dia., ORGDP No. 4868-18.
FSU, 3.0 μ - Firth Sterling Powder, Unclassified, 3.0 μ Dia., ORGDP No. 4868-10.
FSU, 3.1 μ - Firth Sterling Powder, Unclassified, 3.1 μ Dia., ORGDP No. 4868-12.
FSC, 3.2 μ - Firth Sterling Powder, Classified, 3.2 μ Dia., ORGDP No. 4868-20-5.
G.E.-8, 9.1 μ - General Electric Microspheres, 9.1 μ Dia., ORGDP No. 4868-8.
G.E.-2, 6.5 μ - General Electric Microspheres, 6.5 μ Dia., ORGDP No. 4868-2.
Syl. M-30 - Sylvania M-30, Unclassified, 2.4 μ Dia., ORGDP No. 4766-54.

TABLE V

DATA SUMMARY ON SAMPLES HOT PRESSED FROM PREFORMED BLANKS OF LINDE SPHERICAL POWDER

Sample Number	Average Powder Size, microns	Hot Pressing			Void Fraction After Hot Pressing	High Temperature Sintering		Void Fraction After Sintering
		Temp., °C.	Time, hr.	Pressure, psi.		Temp., °C.	Time, hr.	
4848-80-1	5.0	1600	1/2	8000	0.275	1900	1	0.205
4848-80-2	5.8	1600	1	8000	0.275	1900	1	0.222
4848-77-6	5.8	1500	1/2	8000	0.289	2000	1	0.210

EOS Standard Blank

In order to assess the problems associated with some of the evaluation techniques and to provide some means of comparing the evaluation of samples produced under this contract with ionizer materials which are currently available, a porous tungsten slab was supplied by NASA for evaluation. This blank was made by Electro-Optical Systems, Inc. (5) and was fabricated by pressing at 60,000 psi. isostatically and then sintering at 2000°C. for 1 hour in a vacuum of 10^{-5} Torr. It was then infiltrated with copper to permit cutting and machining. The evaluation procedure adopted is summarized in figure 21 which shows the sequence of operations which were carried out on this material. The slab was cut into the various shapes by using an abrasive cut-off wheel, operated with an excess of coolant to prevent local overheating. The various cut samples were then metallographically polished and etched to remove flowed metal. Finally, the copper infiltrant was removed by heating in a vacuum furnace at a pressure of 10^{-6} Torr at up to 1800°C.

A summary of the results obtained in this evaluation is presented in table VI. The void fraction was determined by three methods and it is apparent that the closed porosity is less than was determined by EOS. The pore diameter was determined by five different methods. It is apparent that there is some bias between the methods of determining pore diameter; however, they are sufficiently similar to suggest that any one of them can be used to adequately describe the average pore diameter of a porous sample.

A comparative evaluation of the results obtained on this sample is shown in table VII. It is important to point out that the slab tested at ORGDP was different from that tested by EOS, although they were fabricated concurrently by the same technique and from the same powder lot. The most obvious bias in results is in the permeability measurements and is probably related to test method rather than a difference in material. The pore count results are in reasonable agreement and can perhaps be accounted for by differences in sampling and in operators. The micrograph used for counting at ORGDP is shown in figure 22.

DWG. NO. G-66-603

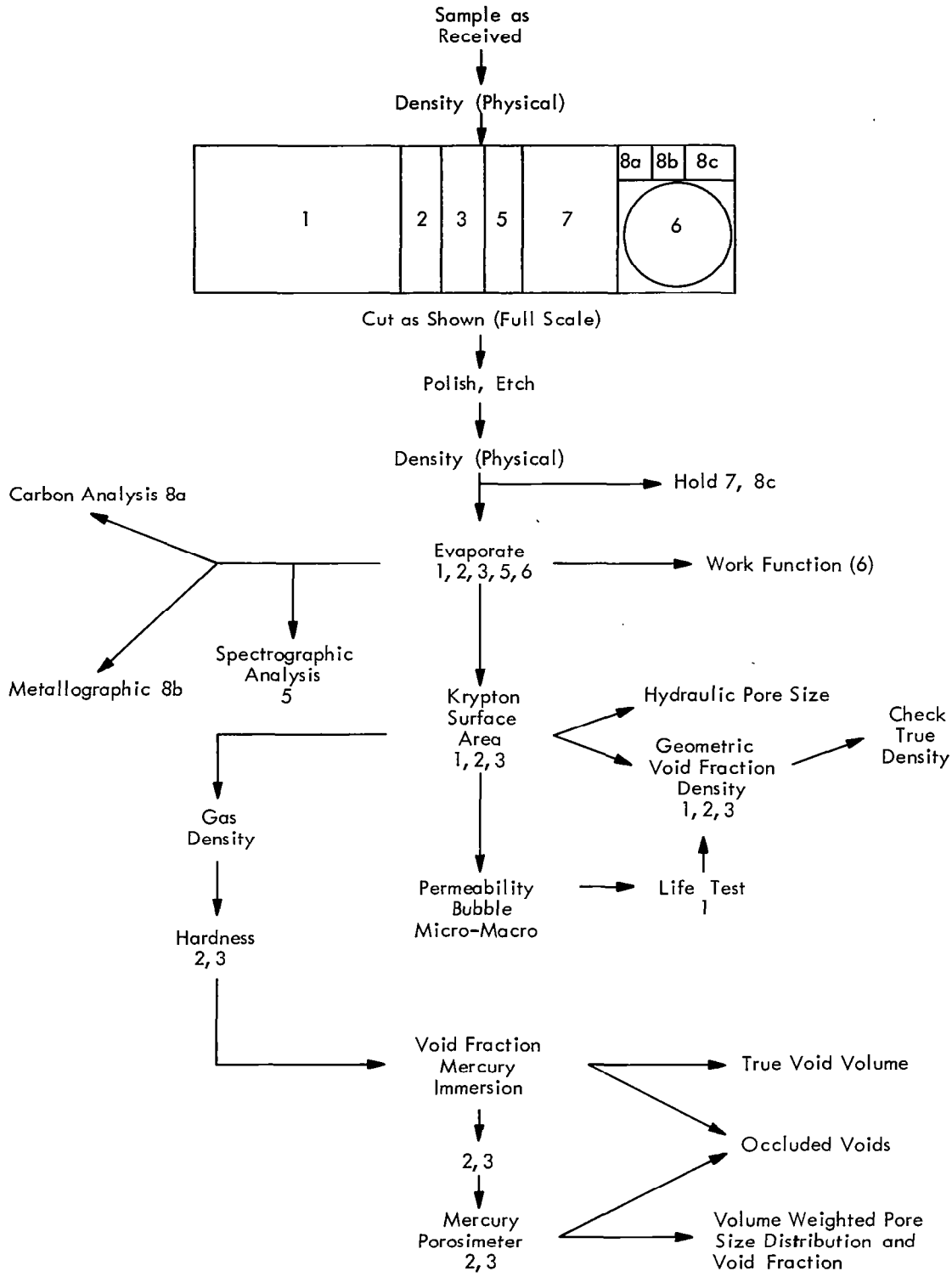

SEQUENCE OF OPERATIONS - NASA POROUS TUNGSTEN SAMPLE

Figure 21

TABLE VI

RESULTS OF EVALUATION OF EOS IONIZER
BLOCK NO. 1, CONTRACT NAS 3-5253

Type of Test	Test Method	Result	Dimensions
Density	Physical Measurements	79.4	% of theoretical
Density	Mercury Immersion	80.0	% of theoretical
Density	Mercury Intrusion	80.3	% of theoretical
True Density	Gas Displacement (Argon)	19.3	g./cc.
Surface Area	Nitrogen Adsorption (BET)	0.018	sq.m./g.
Permeability*	Dry Air Flow	0.17×10^{-6}	g./cm./sec./mm. Hg
Pore Diameter	Permeability	1.98	microns
Pore Diameter	Bubble	2.66 (max.) 1.74 (avg.)	microns microns
Pore Diameter	Mercury Intrusion**	1.29 (avg.) 1.23 (median)	microns microns
Pore Diameter	Calculated Hydraulic Diameter	2.88	microns
Pore Density	Calculated from Void Fraction and Flow Pore Size	6×10^{6}	pores/sq.cm.
Pore Density	Microscopic Count	1.8×10^{6}	pores/sq.cm.

*Extrapolated to zero pressure.

**Using 130° contact angle.

TABLE VII

COMPARATIVE EVALUATION OF RESULTS ON EOS BLOCK NO. 1,
CONTRACT NAS 3-5253

	EOS*	ORGDP
Density, Bulk, % of Theoretical	79.46** 79.12	79.40 ---
Permeability, g./cm./sec./mm. Hg	0.4202×10^{-6}	0.17×10^{-6}
Density, Mercury Porisimeter, % of Theoretical	80.09	80.3
Occluded Voids, %	1.12	0.89
Open Voids, %	18.78	19.72
Pore Diameter, Mercury Intrusion, microns, average	1.24	1.29
Pore Count, pores/sq.cm. Microscopic	2.3×10^6	1.8×10^6
Hardness, Infiltrated, DPH	287	276
Carbon, ppm.	2	< 2

*Abstracted from certification for this slab and from EOS Report 5140, Contract NAS 3-5253.

**This test only was made on the same sample. All other tests were made on a similar sample fabricated identically.

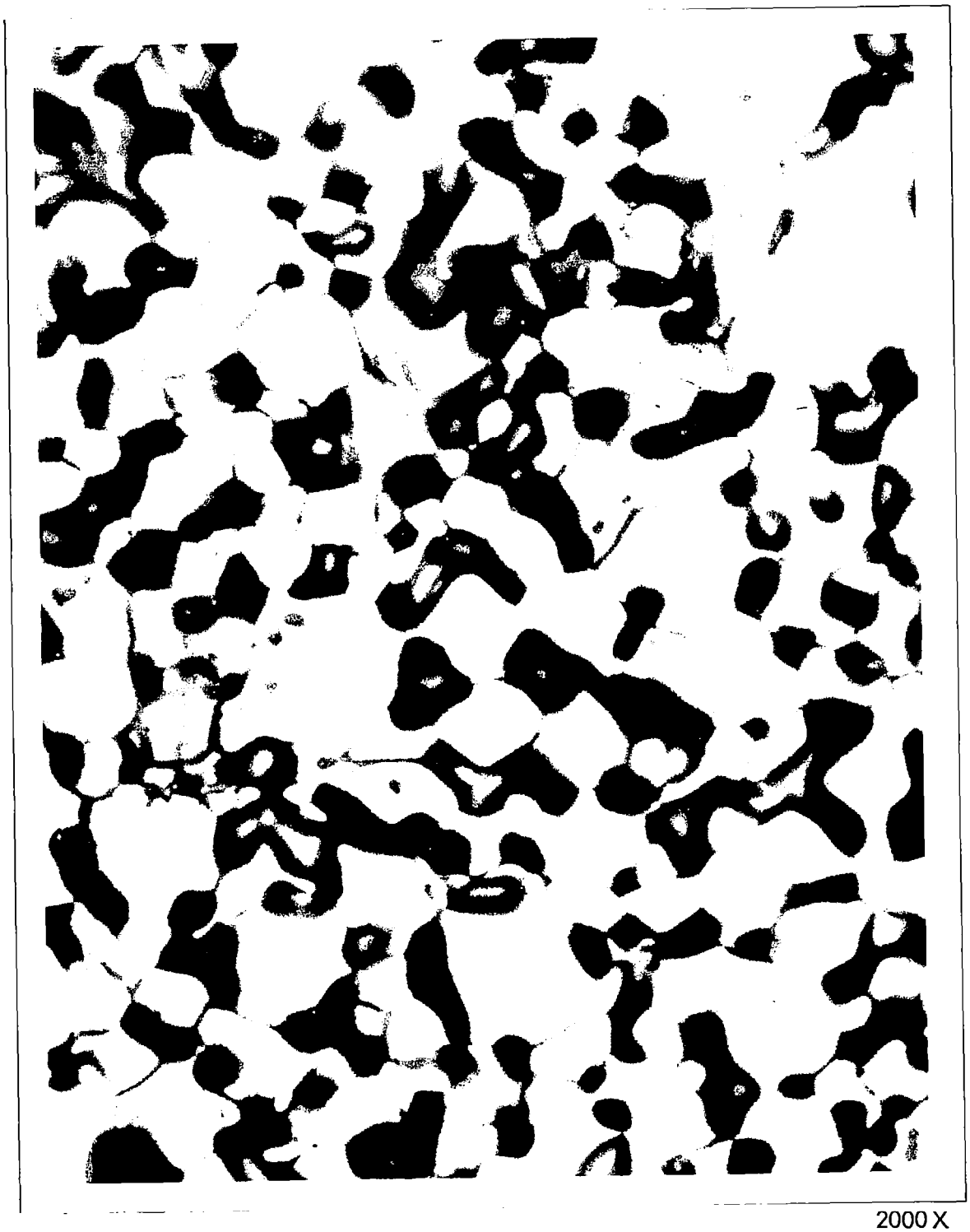

2000 X

MICROGRAPH OF EOS SLAB NO. 1
USED FOR PORE COUNTING

Figure 22

After the measurements were made on the largest of the samples, (Sample 1 in figure 21) it was sintered for 8 hours in hydrogen as a simulated life test. The use of hydrogen in this test rather than vacuum was inadvertant; however, the results are apparently quite similar to those obtained by vacuum sintering. The results are summarized in table VIII. Again the discrepancy is in the permeability measurements. These measurements are shown graphically in figure 23. The flow has decreased substantially and it is apparent that at low pressures it would be difficult to measure. The method of obtaining permeability measurements is described in a later section.

Comparative spectrochemical analyses are shown in table IX. The only discrepancy noted here is in Fe and Mo and it is doubtful that these differences could be considered significant.

This evaluation demonstrates that samples of porous tungsten can be given an extensive series of tests and that when similar techniques are used, results are in general agreement with those obtained by other laboratories. It is also demonstrated that the scope of evaluation tests used in these tests is generally broader than that usually available in such work.

Other Sample Evaluations

In addition to the initial blank from EOS, several other ionizer samples were supplied by NASA during the course of the contract period for our evaluation and cross-comparison. These results are tabulated in table X. The samples cover a broad range of permeability and of pore size as well as sample geometry or configuration. For example, the EOS and the HRL samples are all slabs. The Philips Mod E sample is a porous tungsten ionizer in the Hughes design machined and finished to shape. The TRW samples are actually finished ionizers, sealed to a tungsten plenum chamber and with a cesium feed tube attached. The external dimensions of the ionizing surface are 2 in. x 1/2 in. The surface is made up of 52 parallel grooves of 0.0225 in. radius on 0.040 in. centers. The ORGDP samples listed are of various types as can be seen from the footnotes.

TABLE VIII

LIFE TEST ON COMPARABLE SAMPLES FROM EOS BLOCK NO. 1, CONTRACT NAS 3-5253

	Before		After*	
	EOS	ORGDP	EOS	ORGDP
Density, % of Theoretical	79.33	79.40	85.81	85.34
Permeability, g/sec/cm/mm Hg	0.371×10^{-6}	0.17×10^{-6}	Nil	0.05×10^{-6}
Pore Diameter, microns:				
From Permeability Measurements		1.95		1.74
From Bubble Test		1.74		1.42

*Life Test Conditions: EOS - 6 hrs. at 2000°C. in vacuum.
ORGDP - 8 hrs. at 2000°C. in hydrogen.

DWG. NO. G-66-604

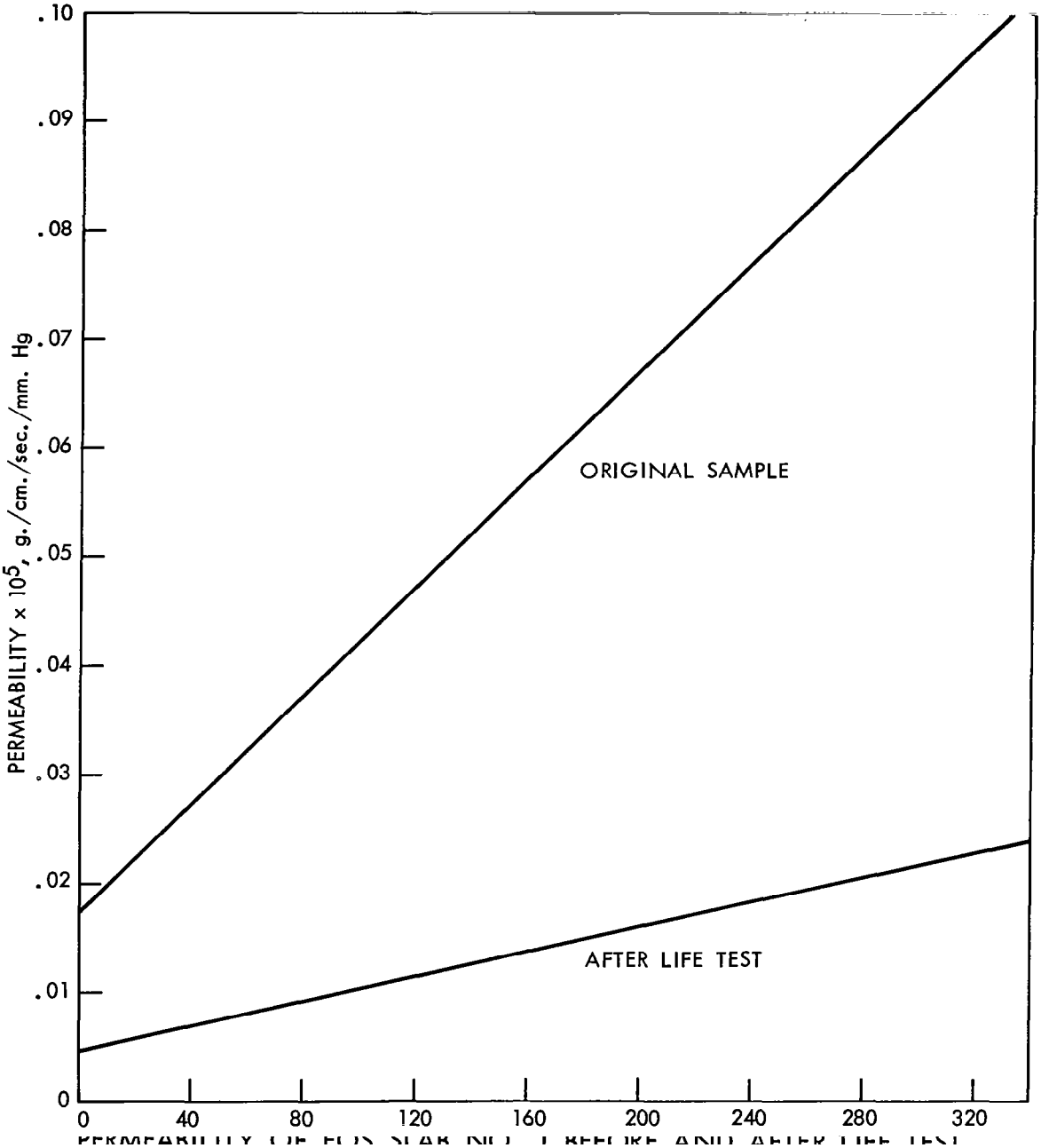

PERMEABILITY OF FEP STAR NO. 1 BEFORE AND AFTER LIFE TEST

TABLE IX

COMPARATIVE SPECTROCHEMICAL ANALYSIS ON EOS BLOCK NO. 1,
CONTRACT NAS 3-5253

Element	Concentration, ppm. ORGDP	EOS*	Element	Concentration, ppm. ORGDP	EOS*
Ag	< 1		Na	6	
Al	3	< 5	Ni	6	< 5
As	< 3		P	< 5	
Au	< 1		Pb	< 1	
B	< 1	< 10	Sb	< 1	
Ba	< 1		Si	2	
Be	< 0.1	15	Sn	< 1	
Bi	< 1		Sr	< 1	
Ca	1	< 10	Ta	1	
Cb	< 1		Ti	1	
Cd	< 1		Tl	< 1	< 10
Co	< 3		V	< 1	
Cr	5	< 5	Zn	< 15	
Cu	5		Zr	< 1	< 10
Fe	20	< 10	Cs	< 10	
Ga	< 1		Rb	< 5	
Ge	< 1				
Hg	< 2				
In	< 1				
K	1				
Li	< 1				
Mg	< 1				
Mn	< 1	< 5			
Mo	13	< 5			

*Obtained from EOS certification of block.

TABLE X

RESULTS OF SAMPLE EVALUATION

Sample Designation	Description	Density, Percent of Theoretical	Permeability*** x 10^5	Pore Diameter, microns: Flow Test Average	Bubble Test Maximum	Bubble Test Average
EOS NAS3-5253	Slab No. 1	79.4	0.0173	1.98	2.66	1.74
EOS NAS3-7102	Slab No. 1	79.7	0.0143	1.98	2.28	1.62
HRL NAS3-7105	Slab No. 205	80.3	0.0112	1.48	--	1.04
Philips Mod E	Hughes design ionizer		0.0314	3.32	3.92	2.66
TRW Thrustor G-1 NAS3-5906	EOS NAS3-5756 Bar No. 1	79.0**	0.0260	1.88	2.42	1.90
TRW Thrustor G-2B NAS3-5906	Hughes NAS3-4110 Bar No. 150, 2.4μ tungsten	83.4**	0.0065	1.14	1.04	0.92
ORGDP 196-197	Hot-pressed and sintered angular powder	80.0	0.0060	1.24	1.02	0.90
ORGDP Tube 4848-62-1	Angular powder	81.7	0.0021	0.62	0.95	0.58
ORGDP Tube 4848-62-2	Angular powder	78.5	0.0029	0.59	0.76	0.58
ORGDP Flat 4848-66-2	Direct formed and sintered 5.8μ spherical tungsten	65.0	0.064	2.30	2.72	2.28
ORGDP Flat 4848-72-1	Direct formed and sintered 5.8μ spherical tungsten	72.3	0.031	2.32	2.98	2.04
ORGDP Flat* 4848-82-1	Direct Formed and sintered 5.8μ spherical tungsten	79.4	0.018	1.92	3.06	1.92
ORGDP Flat 4848-80-1	Hot-pressed from preform and sintered, 5.0μ spherical tungsten	79.5	0.0051	1.14	1.18	1.04
ORGDP Flat 4848-80-2	Hot-pressed from preform and sintered, 5.8μ spherical tungsten	77.8	0.0079	1.32	1.42	1.26
ORGDP Flat 4848-77-6	Hot-pressed from preform and sintered, 5.8μ spherical tungsten	79.0	0.0091	1.38	1.44	1.34

*This sample was ionization tested by TRW Systems.

**Measured by TRW.

***Permeability is in g./sec./cm./mm. Hg.

The comparison between the pore diameter as determined from the flow tests and that determined for the bubble test is generally quite good. These pore diameters are compared in figure 24 which shows graphically the flow test average versus the bubble test average. Figure 25 is a micrograph of the sample which was supplied at NASA's request to STL Laboratories for button tests.

Uniformity Tests

Uniformity tests are divided generally into six different areas as follows:

Flow Tests. The flow test employed in these evaluations involves maintaining a constant flow through a sample and observing the changes in pressure drop across the sample which result from changing the average pressure to which the sample is exposed. The flow is held constant with a critical orifice upstream of the sample. Pressure drop is measured across the sample at several different pressure levels. The permeability coefficient is then calculated from the formula $K = \frac{WL}{A\Delta P}$ where W is the mass flow in grams per sec., A is the area in square centimeters, L is the sample thickness in centimeters, and ΔP is the pressure drop across the sample in millimeters of mercury. The permeability coefficient K is then plotted against the sum of the fore pressure and the back pressure for the measured points. Theoretically, these points should therefore lie on a straight line. Thus, by obtaining a least squares straight line through these data (see figure 23). the permeability coefficient at any pressure can be calculated. It is also possible to calculate a pore size from this data and a transmission coefficient can easily be determined. The calculation of the transmission coefficient is treated in the appendix. The flow measurements were made using a flow system whose principal components are shown schematically in figure 26.

Bubble Test. The pressure differential required to displace liquid from the wetted pores of a material is used to determine the maximum pore size of the sample. This driving force (pressure differential) is opposed by surface tension forces of the liquid in the pores of the

DWG. NO. G-66-605

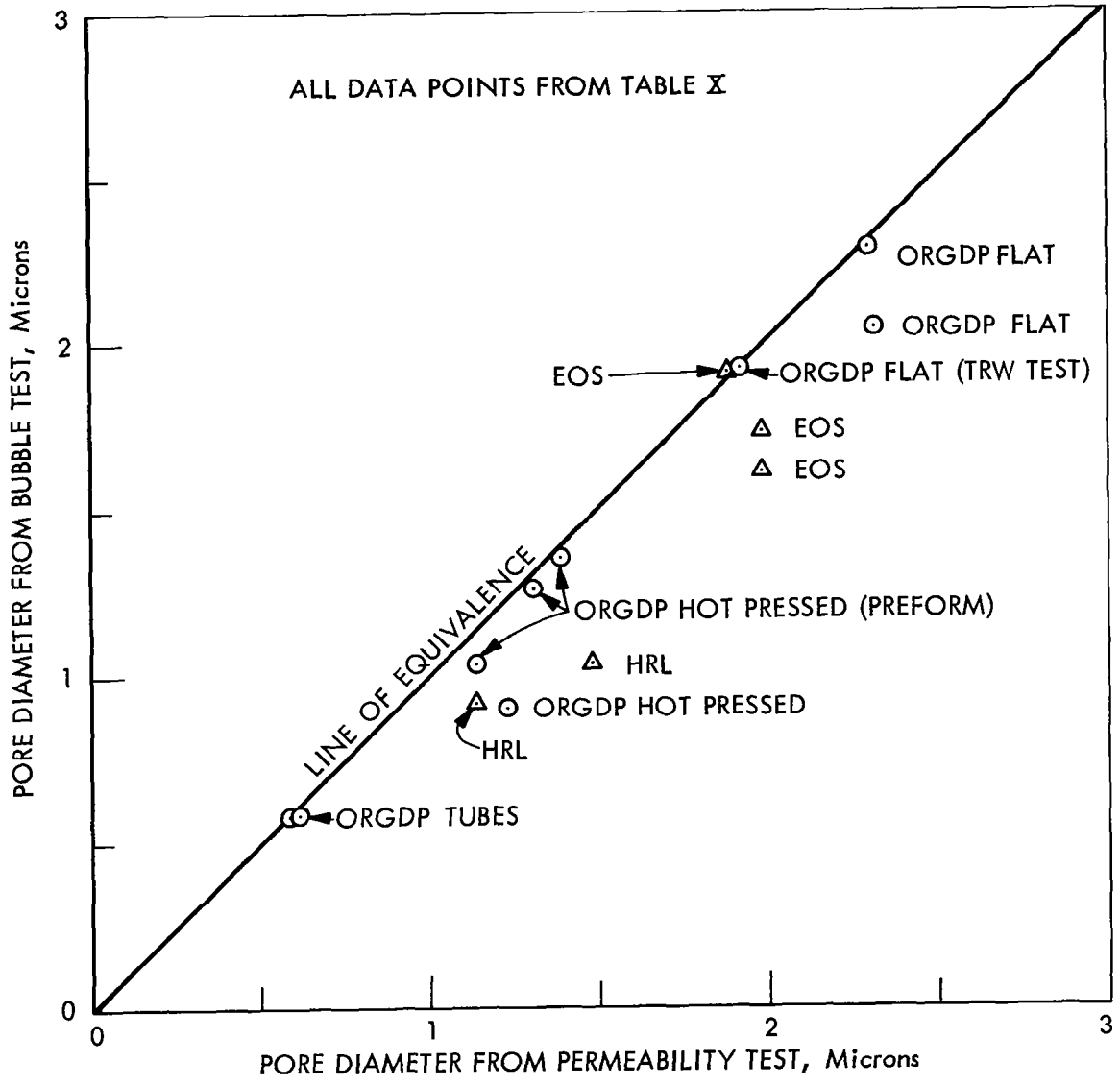

COMPARISON BETWEEN PORE DIAMETER CALCULATED FROM FLOW TEST AND BUBBLE TEST

Figure 24

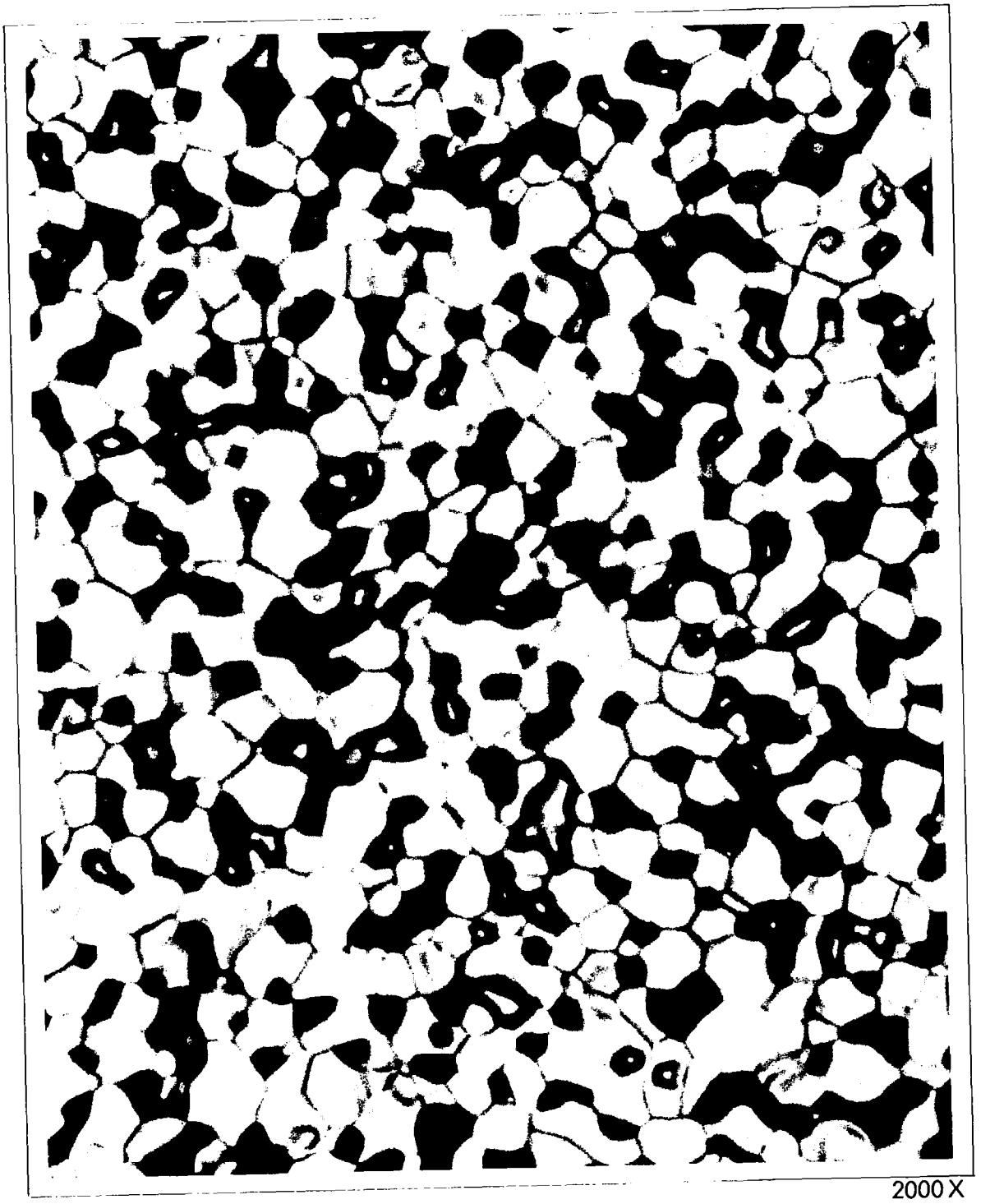

MICROGRAPH OF ORGDP IONIZER MATERIAL TESTED BY
TRW - SAMPLE 4848-82-1

Figure 25

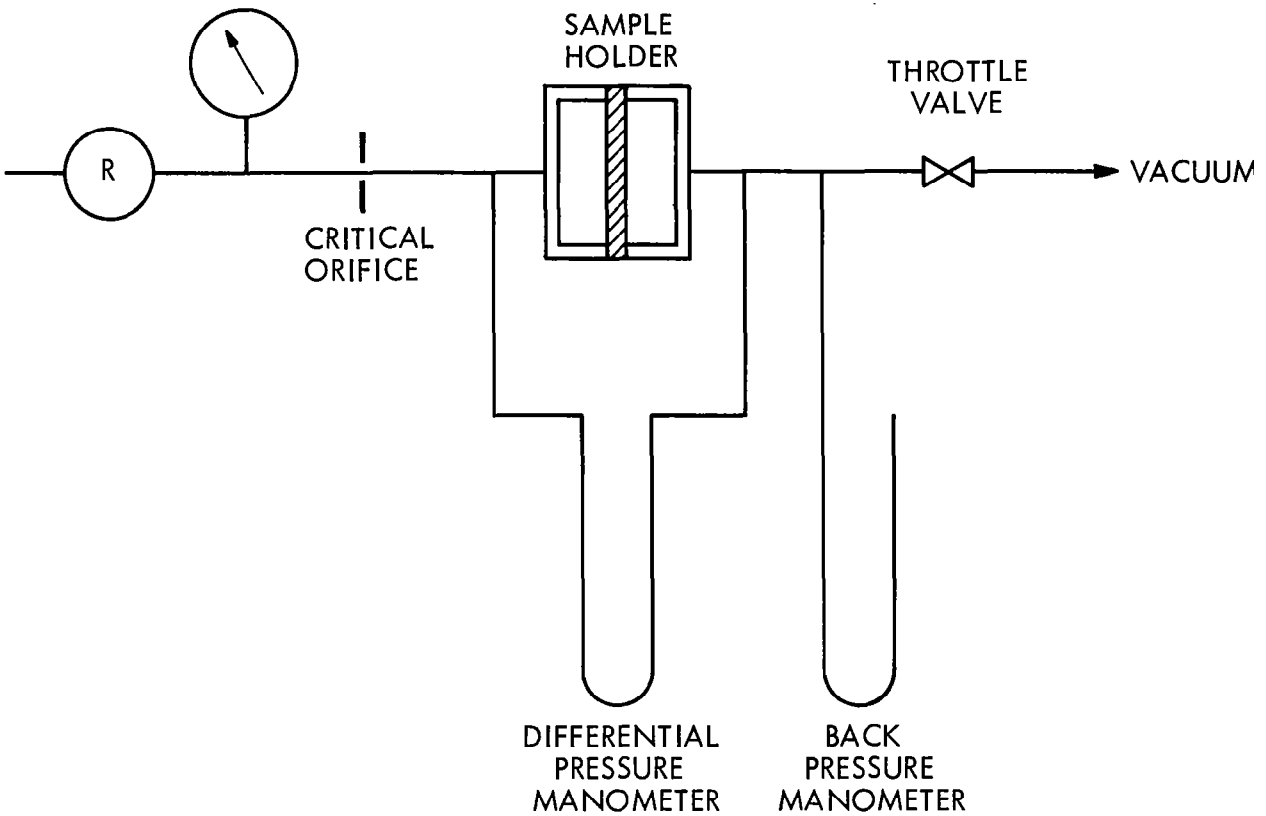

FLOW SYSTEM SCHEMATIC

Figure 26

material. Just enough pressure is applied to force the first bubble of air through the sample. This breakthrough pressure can then be related to the maximum pore size of the sample using an idealized capillary pore model.

In operation a layer of Freon-113 liquid approximately 1/8 in. in depth is poured on the sample and allowed to soak for about 10 - 15 seconds. Air pressure is slowly applied until bubbles appear on the sample surface. The pressure related to the appearance of one or more bubbles is used to calculate the maximum pore size of the sample. Freon-113 has a surface tension of 19.0 dynes per centimeter. The working equation used for determining the pore size from the bubble test was

$$r = \frac{28.6}{\Delta P}$$

where r is the pore radius in microns

ΔP is the differential pressure in centimeters of mercury.

An average pore size can also be estimated using this technique. This estimate is obtained by gradually increasing the pressure differential until the sample surface gives the appearance of being uniformly open to flow. However, this averaging technique is only applicable to material having a reasonably uniform pore size distribution. If the material contains flaws or large pores the liquid is agitated sufficiently to mask the bubble formation as the smaller pores are opened.

Permeability Scanning. Another means of determining uniformity which was investigated during the course of this contract is permeability scanning. In this technique a thermistor probe is moved across the surface of the sample and with air flowing through the sample, the variation in probe temperature caused by local velocity variation is interpreted as variations in permeability. Ideally, these data can then be plotted as iso-perms or lines of constant permeability on a scaled layout of the sample surface thus indicating graphically the degree of permeability uniformity existing in the sample. The permeability scanning development work is described in greater detail in Appendix IV.

Mercury Intrusion. Measurements on pore spectrum on the EOS slab were made with the Aminco-Winslo mercury porosimeter (6). This instrument measures the volume of mercury intruded into the pores of a sample as the pressure is gradually increased. Knowing the surface tension and contact angle of the mercury, it is then possible to compute a pore spectrum from the mercury intrusion data. The results of the mercury intrusion measurements for the EOS Block No. 1, Contract NAS3-5253 are shown in figure 27. Here the cumulative percent pore volume is shown as a function of sample pore radius. The median value of pore radius is obtained at the 50% value of the cumulative percent volume. Measurements are actually made to higher values of pore radius than that shown, depending upon the average pore radius of the sample and the purpose of the evaluation. Very little of the total pore volume lies in pores above 0.7 micron pore radius in this particular case. About 95% of the total pore volume is made up of pores having radii between 0.5 and 0.7 micron.

Radiography. Another method of uniformity determination in porous materials which was explored during this contract period is radiography. In general, radiography can be used to detect and to pinpoint relatively large flaws in a sample. It is very rapid and very effective in estimating down to 2% variations in density. Radiographs of the EOS Slab No. 1 are shown in figure 28. Penetrameters of 0.001 in. and 0.0003 in. tungsten foil are shown in position on these radiographs to demonstrate the density variation which can be detected by this method.

Narrow Beam Radiation Absorption Gauging. A much greater refinement than normal radiography is obtained by the use of narrow beam radiation absorption gauging. With equipment of this type density variations on the order of 0.2 to 0.5% can readily be determined. The radiation absorption gauging equipment is shown in figure 29*. The sample is framed in lead and is positioned on a moveable stage. A source of gamma rays, in this case iridium 192, is positioned on one side of the sample. A detector crystal of sodium iodide is positioned on the opposite side of the sample and in line with the beam emanating from the source. The test sample is then moved automatically between the source and the detector crystal. The output from the detector crystal is photomultiplied and

*Designed and constructed at the Y-12 Plant.

DWG. NO. G-66-607

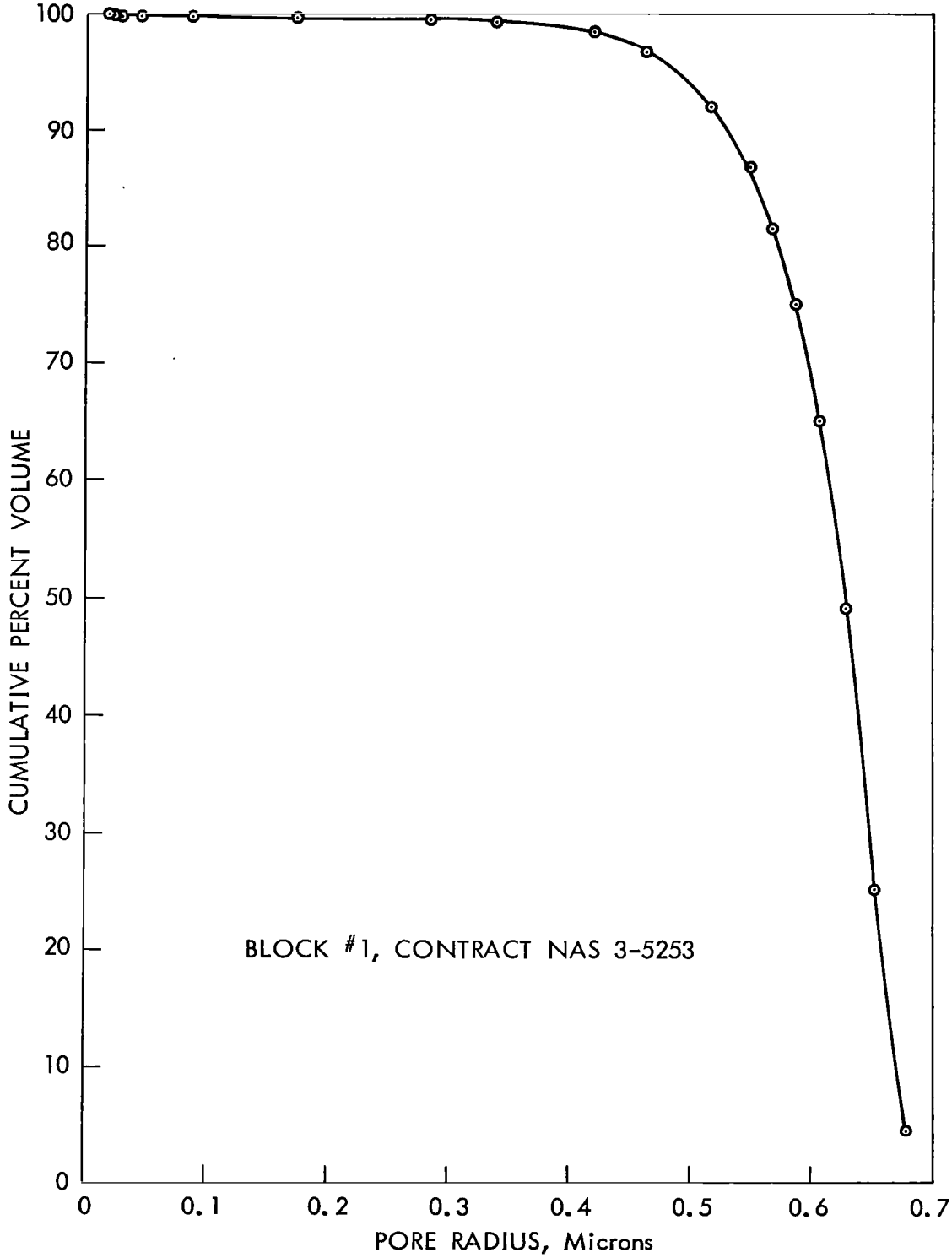

MERCURY INTRUSION DATA CURVE

Figure 27

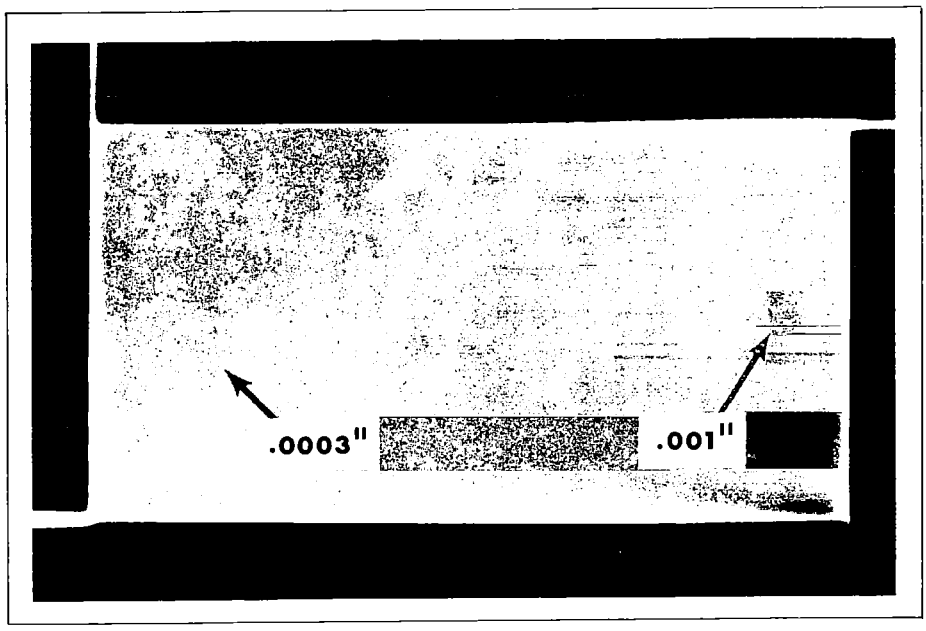

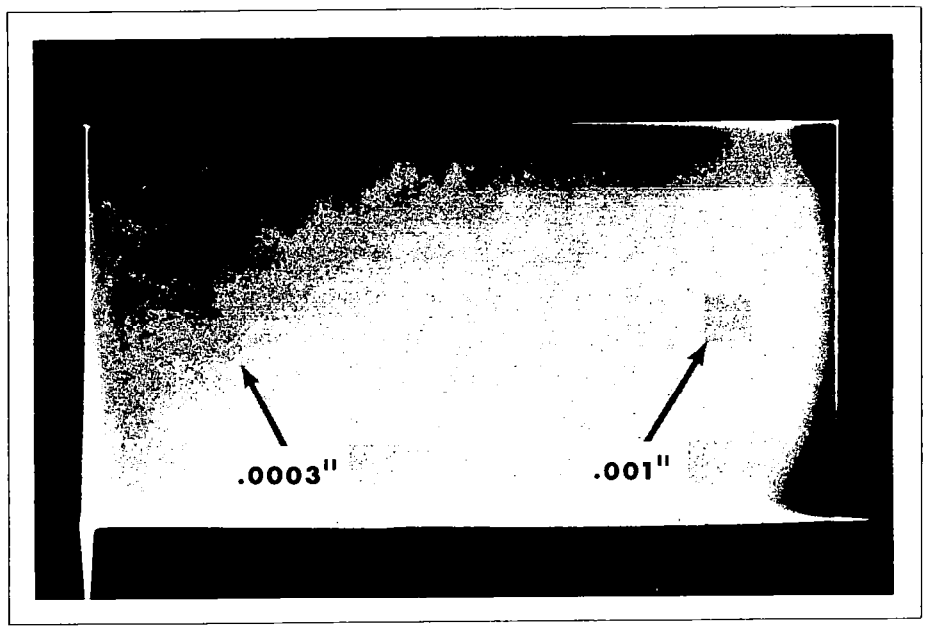

RADIOGRAPHS OF EOS SLAB NO. 1
WITH PENETRAMETERS SUPERIMPOSED

Figure 28

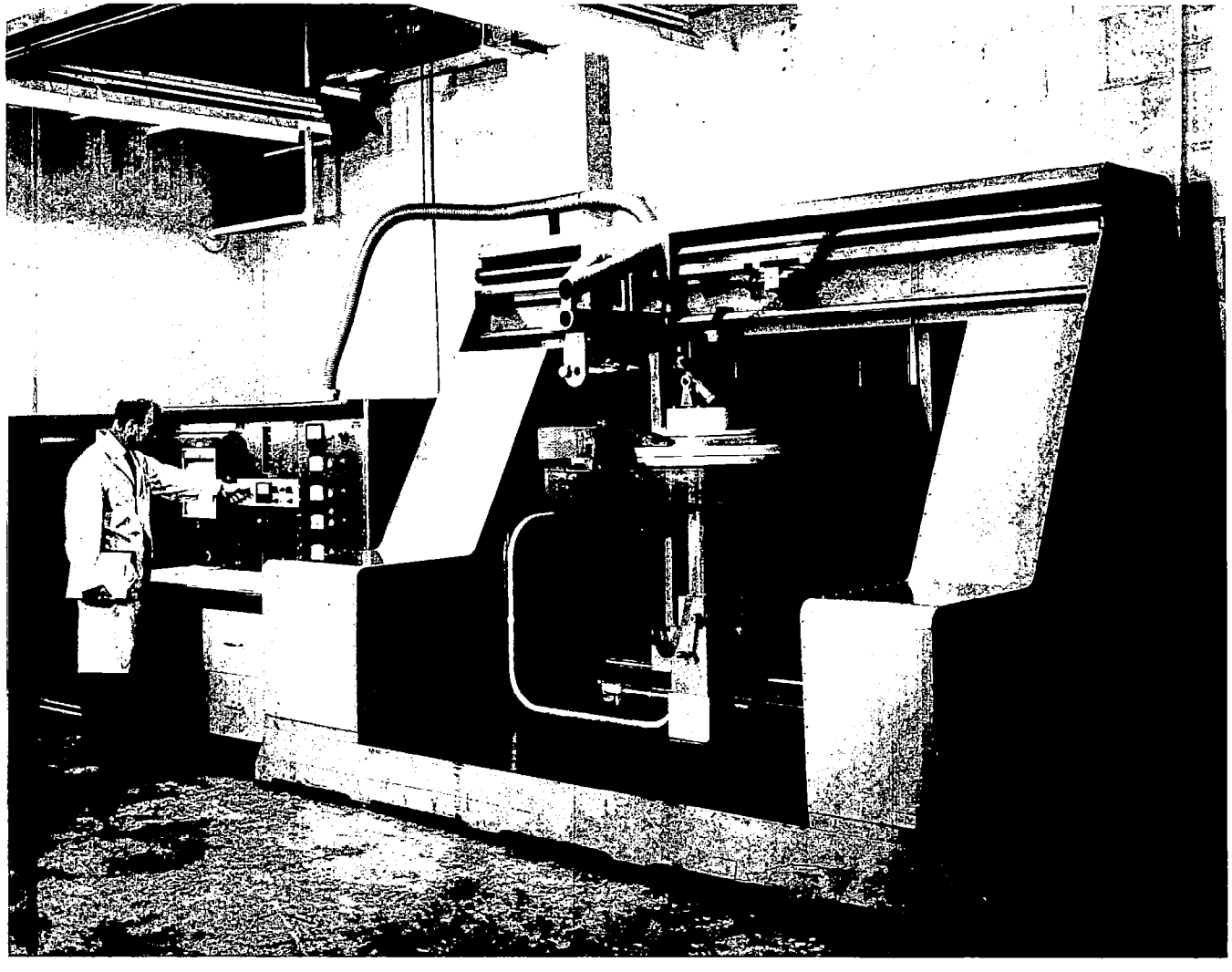

NARROW BEAM RADIATION ABSORPTION GAGE

Figure 29

SECRET

transmitted to an amplifier and recording system, where the intensity of the transmitted beam through the tungsten sample is recorded as a function of beam position in the sample as the sample is moved between the beam and the source.

A typical scan obtained with this type of equipment is shown in figure 30. Superimposed on the graph of the gauge output is a schematic diagram of the sample with a 1-mil penetrameter of tungsten foil in position on its surface. The gauge output remains relatively constant across the sample until the penetrameter enters the scanning field whereupon it increases rapidly by 23 chart divisions. This percentage increase in output corresponds almost exactly to the percentage increase in total sample thickness due to the thickness of the penetrameter. Therefore, a 1-mil change in sample thickness would produce a change of 23% of full scale on the chart and a change of 1 chart division would reflect a 0.1% change in sample thickness, which in this case would be 0.00004 in. Thus, it can be conservatively estimated that changes of 0.2% in equivalent sample thickness can be detected by this method.

One of the difficulties associated with a test of this type is in the gross nonuniformity of the material. Since very small variations can be detected, it is advantageous that the sample be of uniform thickness and that the faces be parallel. It is possible, however, to cancel out the variations in sample thickness by using micrometer measurements to determine sample thickness and then applying this correction to the recorded data of the intensity of the transmitted beam.

Mechanical Properties

The mechanical properties of the porous tungsten generated during this contract were determined by a transverse rupture test. The

DWG. NO. G-66-608

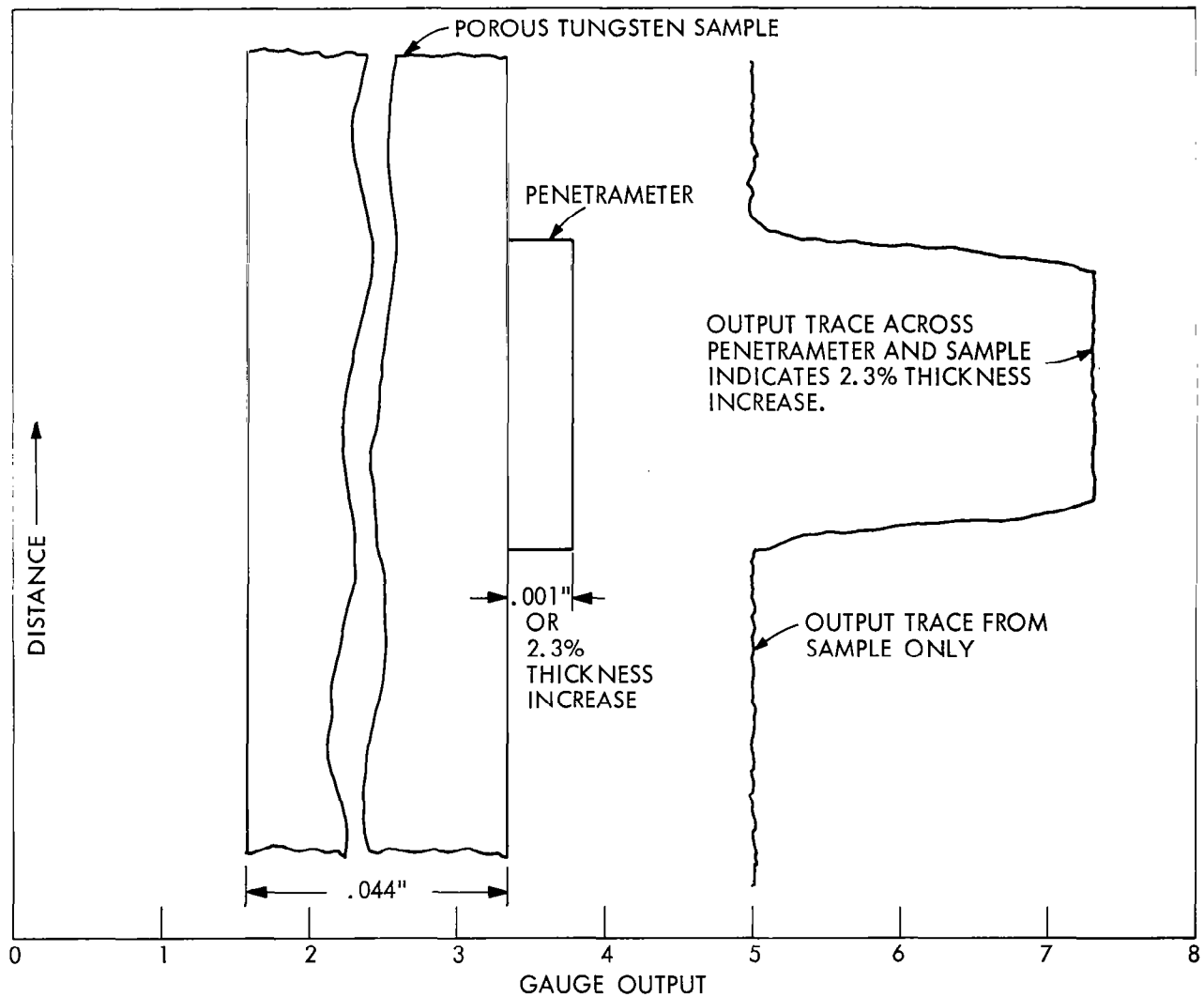

CORRESPONDENCE BETWEEN TUNGSTEN SAMPLE THICKNESS AND RECORDER OUTPUT IN NARROW BEAM RADIATION ABSORPTION GAUGING

Figure 30

by adding lead shot incrementally to a loading fixture and the strain is detected by a dial gauge calculated in ten-thousandths of an inch. With this equipment, the transverse rupture strength of porous tungsten of 65% of theoretical density was shown to be about 27,000 psi.

Ionization Tests

Although the determination of ionization characteristics of porous tungsten was not considered to be a part of the contract a sample was submitted to the STL Laboratories* at the request of NASA for the determination of its ionization characteristics. The sample which was submitted for button tests is sample 4848-82-1 listed in table X. A microscopic cross section of this material is shown in figure 23 at 2000X. The ionization characteristics of this sample were shown by STL to be almost identical to ionization characteristics obtained on a sample prepared by STL Laboratories from the same type and size of powder (4). Thus, it was demonstrated that ionizer materials generated under this contract using the forming methods described are at least equivalent to those produced by other contractors from similar powder using other methods.

VI. MATERIALS SELECTION AND EVALUATION

As was detailed in Section III, Direct Forming, the approach used in demonstrating the feasibility of the forming processes was to first use inexpensive angular powders, then to proceed to readily available spherical powders, and finally to incorporate into the process the best possible classified spherical powders. The purpose of this section is to summarize the properties of all the powders used and to indicate the relative importance of each to the program.

The properties of all of the powders used to fabricate ionizer materials during the contract period are shown in table XI. Figure 31 shows cross-sectional micrographs of each of these powders. Each powder is identified by a number and a descriptive title indicating the manufacturer and type of powder. The powders are angular unless described as microspheres. The Micromerograph data are tabulated to

*Now known as TRW Systems.

TABLE XI

PROPERTIES OF TUNGSTEN POWDERS USED IN IONIZER MATERIALS FABRICATION

Powder Number	Description	Utilization	Relative Importance	Micromerograph Analysis, μ			Surface Area,	Spectroscopic Analysis						
				0% <	50% <	100% <	sq.m./g.	Al	Ca	Co	Cr	Cu	Fe	K
4766-54	Sylvania M-30 Unclassified	Direct Forming and Hot Pressing	Major	0.6	2.4	21	0.361	---	5	---	10	< 1	---	
4868-10	Firth Sterling Unclassified, 25 lb. lot	Direct Forming	Major	0.4	3.0	20	0.215	10	10	---	2	7	15	150
4868-12	Firth Sterling Unclassified, 100 lb. lot	Hot Pressing	Minor	0.4	3.1	27	0.230	---	10	---	---	3	40	1
4894-36	Metals and Refining Co. Unclassified	Direct Forming	Minor	0.7	4.3	34	0.171	5	20	10	16	4	34	5
4868-20-5	Firth Sterling Classified	Direct Forming and Hot Pressing	Major	0.8	3.2	8.2	0.205	< 1	1	< 3	32	---	> 100	
4868-14	Linde Microspheres Precut, 4.2 μ	Direct Forming and Hot Pressing	Major	0.9	3.8	15	0.136	3	15	---	17	10	30	5
4868-16	Linde Microspheres Precut, 5.0 μ	Direct Forming and Hot Pressing	Major	1.1	4.8	15	0.102	3	15	---	17	10	30	5
4868-18	Linde Microspheres Precut, 5.8 μ	Direct Forming and Hot Pressing	Major	1.1	5.5	15	0.093	3	15	---	11	10	25	5
4868-38	Linde Microspheres Unclassified	None	Minor	1.1	5.1	34	0.098	9	15	---	15	7	17	5
4868-66	Linde Microspheres Classified, 4.2 μ	Direct Forming	Major	1.1	4.1	20	0.10	7	20	10	10	10	20	1
4868-2	General Electric Microspheres, 6.5 μ	Hot Pressing	Minor	1.1	6.5	15	0.14	---	100		25	3	100	10
4868-8	General Electric Microspheres, 9.1 μ	Hot Pressing	Minor	0.9	9.1	34	0.13	< 1	< 1	< 3	< 3	5	50	

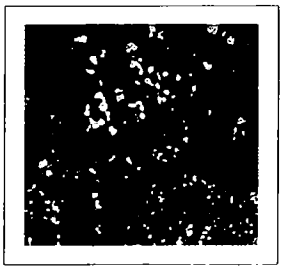

4766-54

Sylvania M-30
Unclassified

4868-10

Firth Sterling
Unclassified, 25 lb. Lot

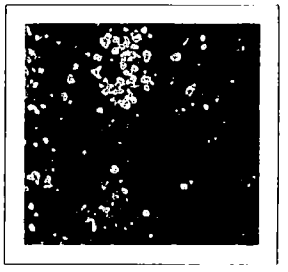

4868-12

Firth Sterling
Unclassified, 100 lb. Lot

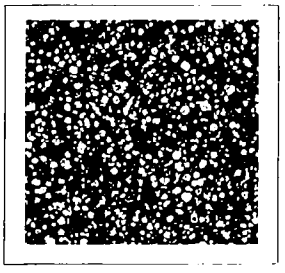

4868-20-5

Firth Sterling
Classified

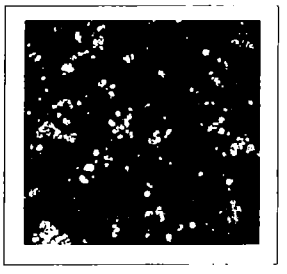

4894-36

Metals and Refining Co.
(M and R)

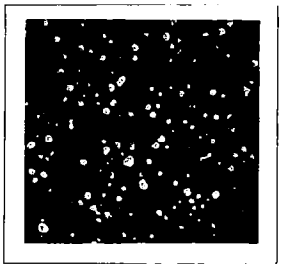

4868-14

Linde Microspheres
Precut, 4.2 μ

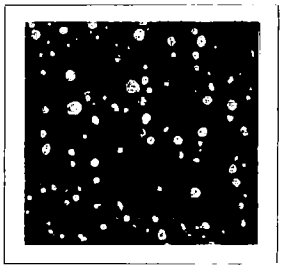

4868-16

Linde Microspheres
Precut, 5.0 μ

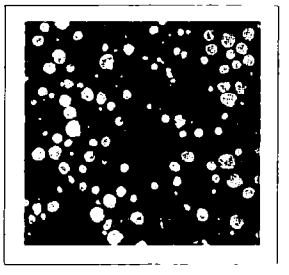

4868-18

Linde Microspheres
Precut, 5.8 μ

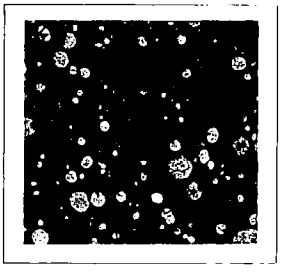

4868-38

Linde Microspheres
Unclassified

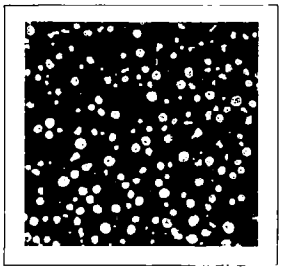

4868-66

Linde Microspheres
Classified, 4.2 μ

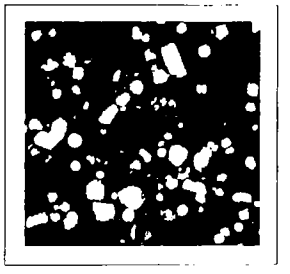

4868-2

General Electric
Microspheres, 6.5 μ

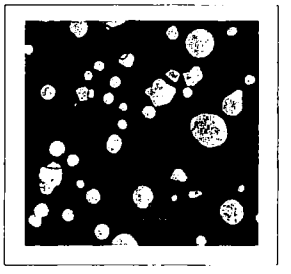

4868-8

General Electric
Microspheres, 9.1 μ

CROSS SECTION MICROGRAPHS AT 345X OF
TUNGSTEN POWDERS USED IN IONIZER FABRICATION

Figure 31

indicate a relative particle size. In some instances this is not completely descriptive since direct particle count data show differences in particle size distribution which are not apparent from the Micromerograph results. Nitrogen surface area (BET method) is also shown as an indication of particle size. A semiquantitative spectrochemical analysis for selected elements is shown to indicate the relative purity of the powders.

Angular Powders, Unclassified

The Sylvania M-30 unclassified powder (No. 4766-54) and the Firth Sterling unclassified, 25 lb. lot (No. 4868-10) are considered to be of major importance to the program because they were the first powders used to demonstrate the feasibility of the direct forming process. The Firth Sterling unclassified powder, 100 lb. lot (No. 4868-12) was of minor importance as a material for fabrication. It was purchased as a feed material for classification into fractions for further use. The Metals and Refining Co. unclassified powder (No. 4894-36) was used late in the program, primarily due to its availability, to demonstrate the fabrication of larger shapes (1/8 in. x 2-1/4 in. x 6 in.) and was not considered seriously as having direct application in the program.

Angular Powders, Classified

The 100-lb. lot of Firth Sterling unclassified powder was classified into six fractions for use in the program. Only one of these fractions (No. 4868-20-5) was considered at the time to be in the proper size range. It was used extensively in direct forming tests to attempt to show that a classified angular powder could be successfully fabricated.

Spherical Powders, Unclassified

Unclassified spherical powders were of relatively minor importance in actual fabrication. The Linde microspheres, unclassified (No. 4868-38) were purchased as a 40-lb. lot to a specification of 75% by weight less than 10 microns. This powder was then classified by Vortec Products Company into 17 fractions for subsequent use. The two

General Electric powders (Nos. 4868-2 and 4868-8) were available in small quantities only and were used only in hot-pressing tests.

Spherical Powders, Classified

The three powders listed as Linde microspheres, precut (Nos. 4868-14, 4868-16, and 4868-18) were of major importance to the program. They were purchased from the Linde Division of Union Carbide Corporation to a size distribution specification and were intended to demonstrate the applicability of classified spherical powders in the direct forming process. These powders were immediately available from Linde and are of particular interest because they are from the same lots of classified fractions which had been supplied to TRW Systems for their use in ionizer fabrication under an Air Force Contract (4).

While the sharpness of the particle size distributions is not as good as desired, these powders were valuable in developing the fabrication conditions. Ionizer material made from the 5.8 micron powder, No. 4868-18, was tested for ionization characteristics by TRW Systems under contract to NASA, as described elsewhere in this report. In order to fully identify these powders, the Micromerograph supplied by Linde with the powders is shown in figure 32. Each curve is identified by the Linde designation as well as the ORGDP number and the TRW Systems number (4). These powders were also used in fabricating preforms for hot-pressing as described in Section IV.

The powder listed as Linde microspheres, classified, 4.8 μ (No. 4868-66) is one of the cuts made by Vortec Products Company from the 40-lb. lot of unclassified Linde microspheres (No. 4868-38). It was considered to be one of the most desirable powders for fabrication and was successfully made into ionizer material late in the program by the direct forming method, thus demonstrating the applicability of the process with sharply classified powders.

The classification and evaluation of the 40-lb. lot of Linde microspheres is described in detail in Appendix III, Classification of Spherical Tungsten Powders. Evaluation of the three Linde precut powders is included for comparison.

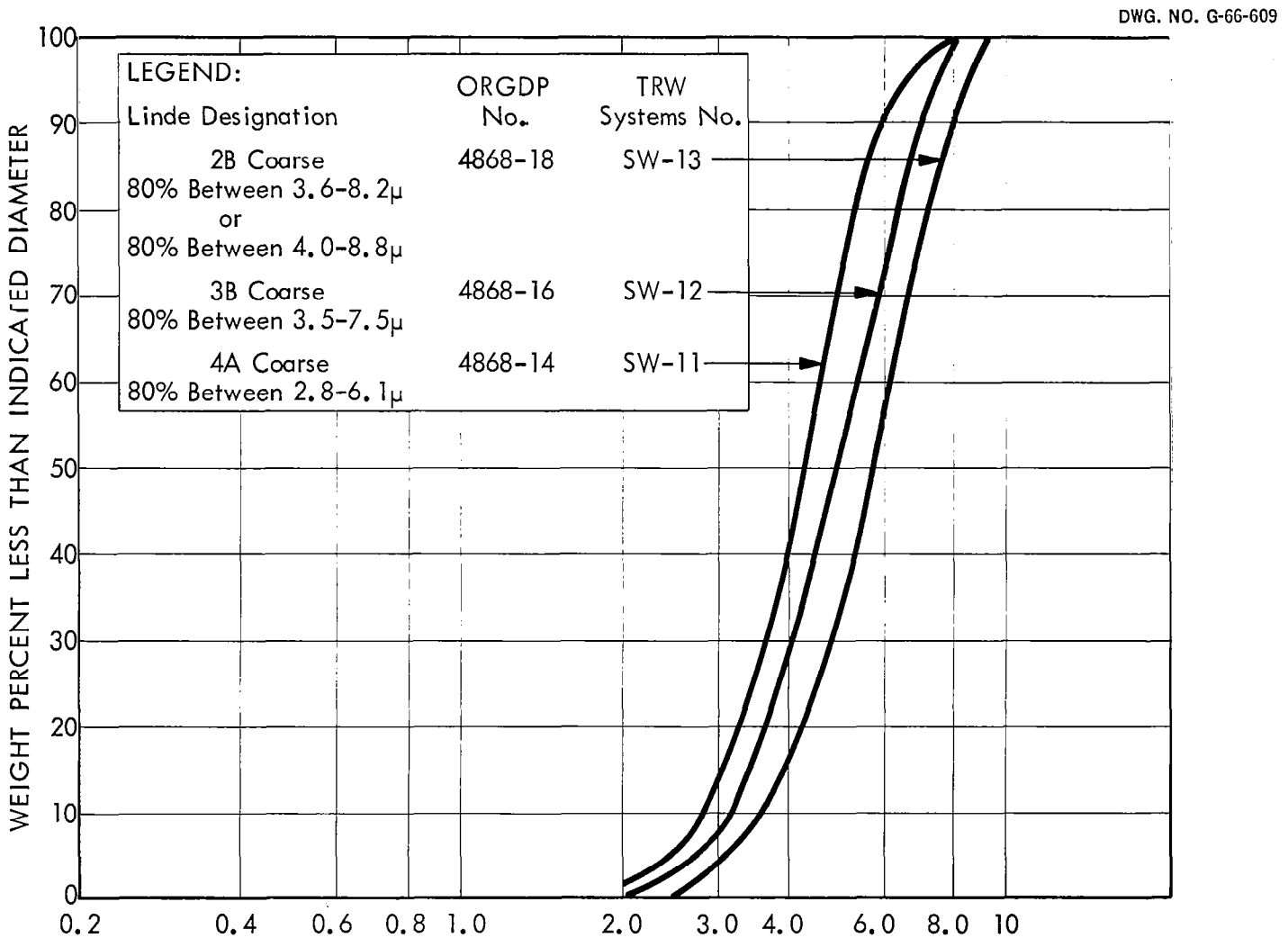

MICROMEROGRAPH PARTICLE SIZE DISTRIBUTION OF
LINDE SPHERICAL TUNGSTEN POWDERS, LOT 2044-6

Figure 32

VII. ACKNOWLEDGMENTS

This contract was performed under the technical management of Thomas J. Riley of the NASA Lewis Research Center. His assistance in providing program direction and his participation in many helpful discussions is gratefully acknowledged. Technical management at ORGDP was provided by C. J. King and H. E. Trammell. Their technical advice and general encouragement contributed significantly to the success of this program.

Much of the preliminary work in applying porous materials technology to the preparation and evaluation of ionizer materials was done by E. M. Foley, David Gray, L. E. Hutchison and D. E. White. Their interest and diligence provided the background for this work and their contribution is gratefully acknowledged. The technical assistance of C. E. Weaver during the first half of the contract period is also acknowledged.

The help of many members of the Technical Division as well as other divisions in the plant is appreciated. Particular acknowledgment is due to Allene George for metallography and H. S. Clinton for particle counting.

Early work in the development of the permeability scanning device was done by W. O. Gentry, H. A. Kermicle, and J. Farquharson. Development to its present state was done by J. A. Cochran, T. E. Zava, and W. T. Collins.

The appendix on the calculation of the transmission coefficient was prepared by D. E. Fain. His assistance in this area of the program is appreciated. Radiography and Narrow Beam Radiation Absorption Gauging were performed by L. M. Fitzgerald and W. H. Moehl of the Y-12 Plant. G. E. Lassiter assisted in many areas of the program. He did all of the hot pressing, assisted in the forming and sintering as well as data handling. His aid is inestimable and is gratefully acknowledged.

BIBLIOGRAPHY

1. LaChance, M., Kuskevisc, G., and Thompson, B., Porous Ionizer Development and Testing, NASA CR-54016 (EOS 3720-Final), Electro-Optical Systems, Inc., Pasadena, California, May 12, 1964.

2. Turk, R. R., and McKee, W. E., Ion Engine Supporting Research and Evaluation, Vol. I, Materials Studies, NASA CR-54411, November, 1965, Hughes Research Laboratories, Malibu, California.

3. Graham, John W., Development of Stabilized Porous Tungsten for Ion Emitters, AMA F9-1-00-20, Astro Met Associates, Inc., January 29, 1964.

4. Kirkpatrick, M. E., and Mendelson, R. A., Final Report on the Development of High Performance Porous Tungsten Ionizers, AFML-TR-65-215, July, 1965, TRW Systems (Contract AF 33(657)-11726) MMP-No. 8-158.

5. Butler, C. K., Fabrication and Testing of Five (5) Porous Tungsten Blocks, EOS Report 5140-Final (NASA Contract NAS3-5253) 20 December 1964, Electro-Optical Systems, Inc., Pasadena, California.

6. Winslow, N. M., and Shapiro, J. J., "An Instrument for Measurement of Pore Size Distributions by Mercury Penetration," ASTM Bulletin, No. 236, 39-44 (1959).

7. Zimmerman, R. L., Berman, D., Garvin, H. L., Hammond, J. M., Ion Rocket Engine Development, Quarterly Progress Report No. 1, Hughes Research Laboratories, NAS 3-6271 (February, 1965).

8. Loeb, L. B., Kinetic Theory of Gases, McGraw-Hill Book Company, Inc., 1958.

9. Present, R. D., Kinetic Theory of Gases, McGraw-Hill Book Company, Inc., 1958.

10. Berman, A. S., and Lund., Proc. 2nd. Int. Conf., Geneva, September 1958, 4, 359 (1959).

11. Herdan, G., Small Particle Statistics, 1953, Elsevier Publishing Company, New York, New York.

APPENDIX I

THE CALCULATION OF TRANSMISSION COEFFICIENTS

Prepared by D. E. Fain

Definition and Theory

The concept of a transmission coefficient is an important one in comparing the properties of porous media or in predicting the flow of one gas from that of another. As defined in reference 2 the transmission coefficient is the ratio of the mass departure rate to the mass arrival rate or $C = \frac{\nu}{\mu}$, where C is the transmission coefficient, ν is the departure rate and μ is the arrival rate. The mass arrival rate is given as $\mu = \frac{\rho \bar{v}}{4}$, where ρ is the gas density and $\bar{v}$ is the molecular velocity. There are some difficulties associated with this definition unless pressures on the down stream side are always zero, since the transmission coefficient should reflect the probability of a molecule starting at one side and reaching the other side. To avoid these difficulties we should define the transmission coefficient as the ratio of the mass departure rate to the difference between the mass arrival rate on each side of the sample. That is, if there is a finite pressure on the down stream side there will be some backward flow (the net forward flow will be decreased).

Therefore $C = \frac{\nu}{\Delta\mu}$ would be a better definition, where $\Delta\mu = (\rho_1 - \rho_2) \frac{\bar{v}}{4}$ and ρ_1 is the gas density on the upstream side and ρ_2 is the gas density on the down stream side.

Although it was not specifically stated, this is the definition that was assumed in reference 7.

With this definition in mind we can now consider the equation for Poiseuille flow with slip. This is given in most standard texts on kinetic theory (8,9). For a capillary

$$W = \frac{\pi}{256}\left(\frac{d^4}{\ell}\right)\frac{M}{\eta RT}\left(P_1^2 - P_2^2\right) + \frac{2d^3}{3\bar{v}\ell}\left(P_1 - P_2\right)$$

W is the mass flow, d is the capillary diameter, ℓ the capillary length, M the molecular weight of the gas, η the viscosity, R the gas constant, T the absolute temperature, $\bar{v}$ the molecular velocity, P_1 the fore pressure and P_2 the back pressure.

The first term is the usual Poiseuille term and is the same as given in reference 7. The second term is the Maxwell slip term, which because of its approximate nature has been multiplied by a factor of $16/3\pi$ to make it consistent with the free molecular flow term. This equation is known to be inaccurate for long capillaries in the low pressure region because it does not predict the Knudsen minimum which is observed with long capillaries. However, a minimum is not observed with a porous material and an equation of the above form with appropriate factors for void fraction and tortuosity can be an accurate representation.

$$W = \left(\frac{\epsilon A d^2}{64\partial_1\ell}\right)\left(\frac{M}{\eta RT}\right)\left(P_1^2 - P_2^2\right) + \frac{8\epsilon A d}{3\pi\bar{v}\ell\partial_2}\left(P_1 - P_2\right)$$

ϵ is the void fraction, A the total sample area, ∂_1 a tortuosity factor for viscous flow, and ∂_2 a tortuosity factor for free molecular flow.

The permeability coefficient can be expressed as

$$K = \frac{W\ell}{A\Delta P} = \frac{\epsilon d^2 M}{64\partial_1\eta RT}\left(P_1 + P_2\right) + \frac{8\epsilon d}{3\pi\bar{v}\partial_2}$$

Now if the permeability coefficient is plotted against the sum of the fore and back pressures, a straight line will be obtained and the intercept at zero pressure summation is

$$K_o = \frac{8\epsilon d}{3\pi\bar{v}\partial_2}$$

This is the permeability coefficient in the limit of zero pressure or the free molecular flow permeability coefficient. Thus the

discharge rate is given by

$$\nu = \frac{K_o \Delta P}{\ell}$$

and $$\Delta\mu = \frac{\Delta_p \bar{v}}{4} = \frac{M\Delta P\bar{v}}{4RT}$$

Thus $$C = \frac{K_o \Delta P}{\ell} \cdot \frac{4RT}{M\bar{v}\Delta P}$$

or $$C = \sqrt{\frac{2\pi RT}{M}} \frac{K_o}{\ell}$$

also $$C = \frac{4RT}{\ell M\bar{v}} \cdot \frac{8\epsilon d}{3\pi\bar{v}\partial_2}$$

or $$C = \frac{4\epsilon d}{3\ell\partial_2}$$

Thus the transmission coefficient depends only on the physical structure of the porous sample. Theoretically there is some argument as to the numerical factors that occur in this equation. However, from the standpoint of characterization of a porous sample this is relatively unimportant. Since the transmission coefficient is independent of gas, any gas (air for example) can be used to determine the transmission coefficient which will then be the same for all gases. The permeability coefficient is measured at several different average pressures and then the zero pressure permeability coefficient is determined by the extrapolation of these data. The transmission coefficient is then calculated from the zero pressure permeability coefficient

$$C = \sqrt{\frac{2\pi RT}{M}} \frac{K_o}{\ell}$$

As derived here consistent units must be used in the calculations. For example K_o must be in consistent cgs units. It has been common practice to calculate K in g./sec. cm. mm. of Hg. These values must be divided by $1.332 \times 10^3 \frac{\text{dynes}}{\text{cm}^2 \text{ mm. of Hg}}$ to give K in consistent cgs units of

seconds. We will use symbol K where consistent units are used and the symbol K' for values with units of g./sec. cm. mm. of Hg.

There are some small variations in C for different gases. Some experimental data showing some of these variations are given by Berman and Lund in reference 10.

Aside from the use of C for estimating the free molecular flow of different gases, a pore size can also be calculated. This pore size must have associated with it an unknown shape factor ∂_1. However, for porous materials made from similar material and near the same void fraction, this factor is probably very nearly the same and thus this pore size could be used to compare similar porous material. This same argument can also be made concerning the Poiseuille term. A pore size with its associated shape factor can be calculated from the slope of the K vs ΣP curve. This slope is proportional to the square of the pore diameter and could be used in the same way as the pore size determined from the intercept of the K vs ΣP curve.

The shape factor associated with the Poiseuille term is probably not very much different from the shape factor associated with the free molecular flow term. Therefore, by taking the ratio of the slope of the K vs ΣP curve to the intercept these shape factors will approximately cancel each other and a number more nearly proportional to the actual pore size can be obtained. Although some reservation must be retained, the pore size determined from this ratio can more reliably be used to compare pore size of different materials. This latter pore size is the one quoted by ORGDP as the flow determined pore size.

Comparison With Other Methods of Calculating Transmission Coefficients

Although there are decided advantages to using the above for determining transmission coefficients, it does require slightly more complex apparatus to obtain the necessary data. The following is a description of how data obtained in this way may also be used to calculate transmission coefficients equivalent to those given in references 1 and 7.

The data are obtained using a constant flow system. The flow is maintained constant with a critical orifice upstream from the sample. The pressure drop is measured across the sample with several different back pressures. The permeability coefficient is then calculated from the formula

$$K' = \frac{W\ell}{A\Delta P}$$

where W is the mass flow in g./sec., A is the area in sq. cm., ℓ is the sample thickness in cm., and ΔP is the pressure drop across the sample in mm. of Hg. The permeability coefficient K' is then plotted against the sum of the fore pressure and back pressure for the measured points. These points should lie on a straight line. Thus by obtaining a least square straight line through these data the permeability coefficient at any pressure can be calculated.

The method of reference 1 for measuring flow is with an average pressure drop across the sample of 38 cm. of Hg. If we assume that the measurements are made at an atmospheric pressure of 76 cm. of Hg, then the back pressure on the sample is 76 cm. of Hg; the average fore pressure is 114 cm. of Hg; and the pressure summation is 190 cm. of Hg. Thus the permeability coefficient equivalent to the reference 1 conditions can be calculated from this data. It should be recognized that variations in atmospheric pressure will make small variations in the measurements. The variations to be expected can be estimated from the curves.

The equivalent reference 1 calculations of the transmission coefficients can now be made from the formula

$$C = \frac{\nu}{\mu}$$

$$\nu = \frac{K}{\ell}\Delta P \quad \text{and} \quad \mu = \frac{\rho\bar{v}}{4}$$

or

$$C = 4\,\frac{K\Delta P}{\rho\bar{v}\ell}$$

For dry air flow at 25°C.

$$C = 7.33 \times 10^4 \frac{K\Delta P}{\ell P}$$

and for the reference 1 conditions, ΔP = 38 cm. of Hg, P = 114 cm. of Hg, and ΣP = 190.

Thus $C = 18.3 \frac{K'}{\ell}$ where now K' is the value from the curve at ΣP = 190 in the usual units of g./sec. cm. mm. of Hg. To make the calculation of reference 1 we may start directly with their equation 12 on page 52.

$$\tau = \frac{0.00491}{d} \left[\frac{W/A}{\Delta P}\right]$$

Where W is the mass flow in g./sec., A is the area in sq. cm., ΔP is the pressure difference across the sample to obtain the flow W in mm. of Hg, and d is the pore diameter of the sample in cm.

Now $$\frac{W/A}{\Delta P} = \frac{K'}{\ell}$$

Thus the necessary permeability coefficient corresponding to the reference 7 conditions can be obtained from the permeability coefficient curve. The reference 7 conditions are slightly different from those of reference 1; therefore, for the same sample a slightly different permeability will be obtained. The reference 7 conditions assuming an atmospheric pressure of 76 cm. of Hg are an average ΔP of 28 cm. of Hg (11 inches), average fore pressure 104 cm. of Hg, back pressure 76 cm. of Hg, and summation pressure of 180 cm. of Hg. Using these conditions a permeability coefficient can be obtained from the curves and using that permeability coefficient we can calculate τ by

$$\tau = \frac{0.00491}{d} \frac{K'}{\ell}$$

where K' is in units of g./sec. cm. mm. of Hg.

At this point it is difficult to decide what pore diameter should be used in the above formulae. The pore diameters determined by the several different methods such as mercury intrusion, micrographic measurements, ratio of void volume to surface area, or flow measurements are sometimes quite different. Thus some variation in estimates of the transmission coefficients should be expected when this method is used.

APPENDIX II

AUXILIARY TASKS

During the program, techniques and processes were investigated which did not ultimately become a major part of the work. In addition, materials were produced and supplied to NASA which, while not directly relating to the specific goals of this contract, were of interest in the more general area of porous tungsten technology. This phase of the program activity is summarized in this appendix.

Mercury Flow Control. During the course of the contract, the applicability of some of the porous materials generated under this contract in other NASA programs became apparent. There was an interest by NASA in porous tungsten discs of much higher permeability than was ordinarily available for use as a mercury flow control for electron bombardment ion engine experiments. As a result of this interest, three samples of porous tungsten of about 65% of theoretical density were sent to the Lewis Research Center for evaluation. These samples were found to be satisfactory for this application and a small contract for the production of a larger amount of material of even higher void fraction was initiated. NASA had originally desired this material in the form of a porous tungsten rod 1/4 in. in diameter and was interested in about 40 linear inches of this material. In addition to this, the permeability target was to be about twice that of any material previously supplied. It was felt by NASA that a rod would be preferable for an application of this type in that it would be relatively simple to Elox machine 0.040 in. thick discs from a rod and thus obtain maximum useful material from the material supplied. The particular powder to be used was not defined nor was it limited to spherical powder although spherical powder was used in the test samples which were provided. Although ORGDP personnel felt that such a rod could be provided ultimately, it was determined that considerably more development would be necessary than had originally been expected. At the concurrence of NASA it was decided to provide flat material of more proven uniformity which could be tested at ORGDP and which could be more readily fabricated by established techniques. At the close of the contract

period, this material was being prepared and on December 15, 1965, 80 linear inches of porous tungsten 1 in. wide x 0.060 in. thick, having a transmission coefficient of approximately 1×10^{-3} with a void fraction averaging 0.48 was delivered to NASA Lewis Research Center for use as a mercury flow control in electron bombardment ion engine experiments.

Fiber Production. As the result of an expressed interest by NASA a process for the production of porous tungsten fibers was developed. The interest which NASA had in this work was several fold. First it was desired to consider the possibility of producing solid tungsten fibers or fibers of other materials to be used in other NASA programs for the fiber strengthening of high temperature, high strength materials. Secondly, there was an interest in such a material for use in an advanced propulsion technique whereby large particles of material would be stripped from a small wire and accelerated as a means of propulsion. Thirdly, there was interest in using porous tungsten fibers or wires for the measurement of work function and ionization characteristics. In the normally described methods of measuring work function or ionization characteristics commercially available drawn tungsten wire is used. As is well known, wires of this type have a very pronounced fiber texture. Conversely, porous tungsten wires should have a random orientation. Since it is also well known that the work function of tungsten is strongly dependent upon the crystallographic planes which are exposed at the surface it is reasonable to assume that work function measurements on drawn wire should be highly dependent on the orientation of the wire. Work function measurements made on porous wire should not have this disadvantage and the data obtained therefrom should be much more directly applicable to work function measurements on buttons or finished ionizers.

Fibers varying in diameter from 0.002 in. to 0.010 in. were produced during this contract period. They were sintered at up to 2000°C. in hydrogen and were shown to be very strong and able to support their own weight in bending. Micrographs of these fibers are shown in figure 33 and a cross section of one of the fibers is shown in figure 34. The void fraction of these fibers is on the order of 0.50. They were produced from spherical tungsten powders.

25X A-2171

2 MIL AND 4 MIL FIBERS

Figure 33

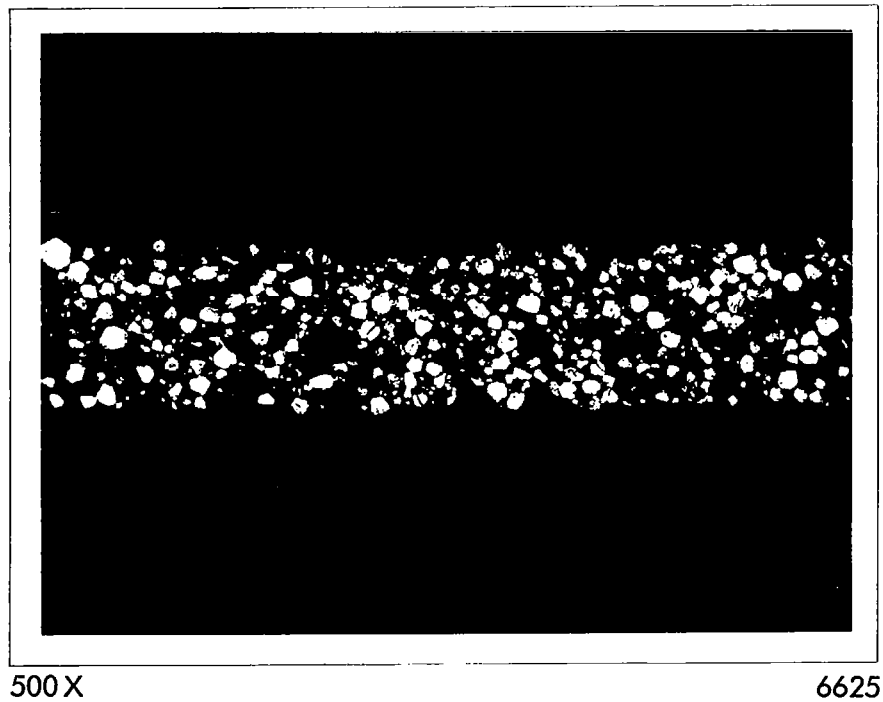

500X 6625

SECTION OF 2 MIL FIBER

Figure 34

Porous Tungsten Tubes. Two porous tungsten tubes were requested by NASA for an undisclosed application. The tubes supplied were approximately 6 in. long x 3/8 in. dia. x 0.015 in. thick. Their properties are listed in table XII and are also included in the comparative evaluation of table X, Section V, Ionizer Evaluation.

TABLE XII

PROPERTIES OF POROUS TUNGSTEN TUBES

Sample Designation	Density, Percent of Theoretical	Permeability* x 10^5	Pore Diameter, microns		
			Flow Test Average	Bubble Test Maximum	Bubble Test Average
4848-62-1	81.7	0.0021	0.62	0.95	0.58
4848-62-2	78.5	0.0027	0.59	0.76	0.58

*Permeability is in grams/sec./cm./mm. Hg

Powder Pack Work. One of the preliminary evaluations in the program concerned the applicability of a Firth Sterling powder with a particle size of about 3.0 microns (No. 4868-10). In order to determine the characteristics of sintered material made from this powder, it was considered desirable to blend with the powder various percentages of carbon, which would help to maintain the porosity and which could be removed at a later stage. A summary of the data obtained in this preliminary study is shown in table XIII. As can be seen, the green void fraction is directly proportional to the percentage of carbon which is added to the tungsten powder and also the sintered void fraction increases with the amount of carbon. The change in void fraction with sintering also is a function of this parameter. The pore diameter appears to be less dependent on the carbon percentage although the effect of void fraction on pore size is not shown in this comparison. It was determined that this powder was not satisfactory for use in this process because of the fact that it was an unclassified powder containing a large number of

fines and upon sintering to the void fraction range of interest, a large number of very small pores were developed, which was undesirable.

TABLE XIII

TUNGSTEN-CARBON POWDER PACK PROPERTIES

Carbon, %	Green Void Fraction	Sintered Void Fraction	Change in Void Fraction	Pore Diameter, microns
0	0.458	0.317	0.141	1.6
1	0.458	0.314	0.144	1.9
2	0.482	0.328	0.154	1.3
3	0.519	0.351	0.168	1.3

Isostatic Pressing. In other early work it was felt that the best possible uniformity might be obtained in an ionizer structure by incorporating isostatic pressing in the forming process. This procedure would make isostatic pressing one step in the process and would be as follows. First the material would be formed into a flat or a shape as desired; secondly it would be isostatically pressed to give initial consolidation beyond that obtained in the forming process; thirdly, it would be hot-pressed to give further uniformity; and finally it would be sintered to final size and shape at high temperature in hydrogen. After some initial work it was determined, however, that isostatic pressing produced some difficulties in that upon subsequent sintering some nonuniformities developed which were not anticipated and for this reason, isostatic pressing was not emphasized during most of the contract. It was found later, however, that the nonuniformities which developed could be avoided by a simple procedure. Therefore isostatic pressing appears to have promise and will be investigated in the future.

In the isostatic pressing work, a number of flat samples were pressed at pressures up to 60,000 psi. and sintered from 1800° to 2000°C. The sintered void fractions obtained on this material are shown in

table XIV. Other data which show the shrinkage which occurred during pressing and subsequent sintering of additional samples are shown in table XV. Shaped samples and flat samples were pressed during this second study. The die used to press shaped samples from flats is shown in figure 35. Examples of the shapes produced are shown in figures 36 and 37. It is apparent that in most cases the isostatically pressed materials were sintered to much too low a void fraction to be usable. Also due to the fact that an unclassified powder was used in most of this early work, the development of low void fraction and small pore size precluded the successful evaluation of this technique as a forming method. Therefore, it is desirable to incorporate classified spherical powder into a process involving isostatic pressing.

TABLE XIV

VOID FRACTION SUMMARY ON ISOSTATICALLY PRESSED AND SINTERED FLAT SAMPLES

Sample No.	Isostatic Pressure, psi.	Sintering Temperature, °C.	Sintered Void Fraction
4867-15- 1	10,000	1800	0.403
4867-15- 2	10,000	1900	0.378
4867-15- 3	10,000	2000	0.283
4867-15- 5	25,000	1800	0.337
4867-15- 6	25,000	1900	0.277
4867-15- 7	25,000	2000	0.246
4867-15- 9	40,000	1800	0.336
4867-15-10	40,000	1900	0.309
4867-15-11	40,000	2000	0.258
4867-15-13	50,000	1800	0.302
4867-15-14	50,000	1900	0.327
4867-15-15	50,000	2000	0.232
4867-15-17	60,000	1800	0.359
4867-15-18	60,000	1900	0.240
4867-15-19	60,000	2000	0.243

TABLE XV

SHRINKAGE DATA SUMMARY ON ISOSTATICALLY PRESSED AND SINTERED SAMPLES

Sample No.	Sintering Temperature, °C.	Sintered Void Fraction	Linear Shrinkage, percent	
			Due to Pressing	Total (Pressing and Sintering)
4867-65-1*	1800	0.289	***	12.8
4867-60-3*	1900	0.181	***	16.3
4867-60-4*	2000	0.140	***	17.5
4867-60-7*	1800	0.178	6.0	17.1
4867-60-8*	1900	0.123	6.3	18.4
4867-60-9*	2000	0.092	6.2	19.9
4867-61-2**	1800	0.228	5.2	14.6
4867-61-3**	1800	0.212	5.3	15.8
4867-61-4**	1900	0.155	7.3	18.8
4867-61-5**	2000	0.109	6.2	19.8

*Ionizer shape samples.

**Flat sheet samples.

***Samples were not isostatically pressed.

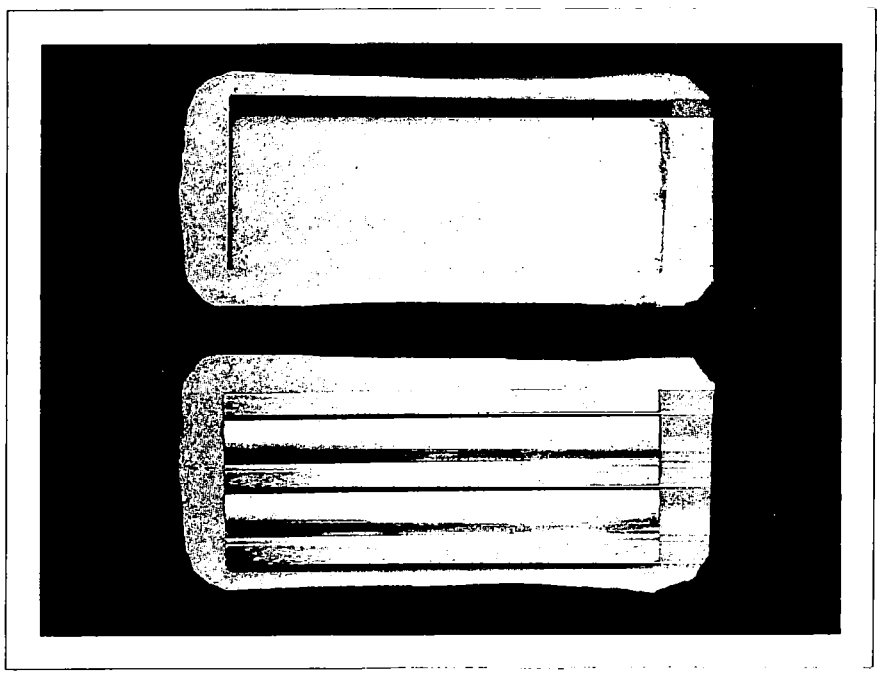

1 X A-2142

STEEL DIE FOR PRESSING SHAPE

Figure 35

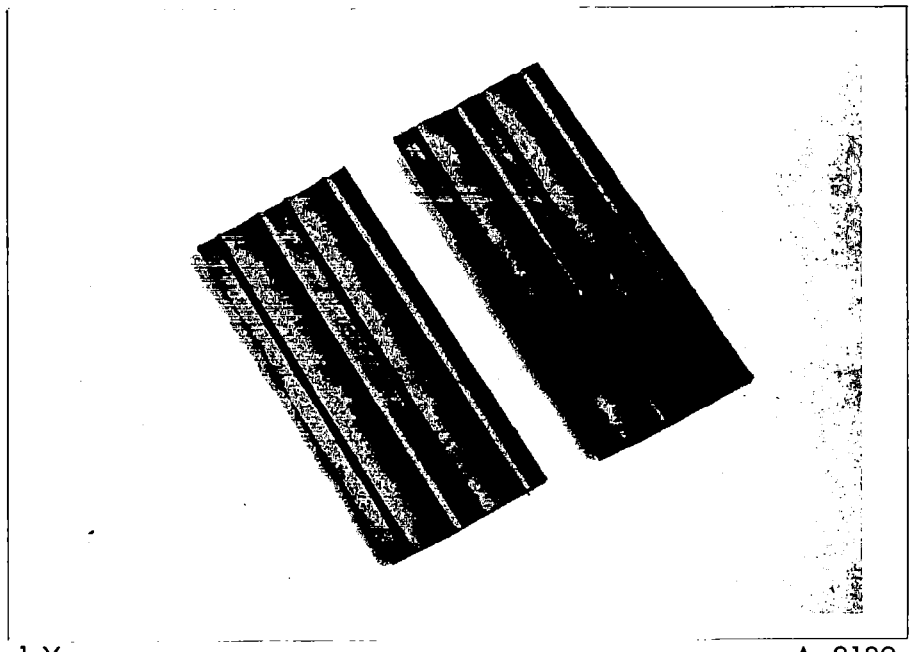

1 X A-2139

SHEET SAMPLES PRESSED ON STEEL DIE - TOP VIEW

Figure 36

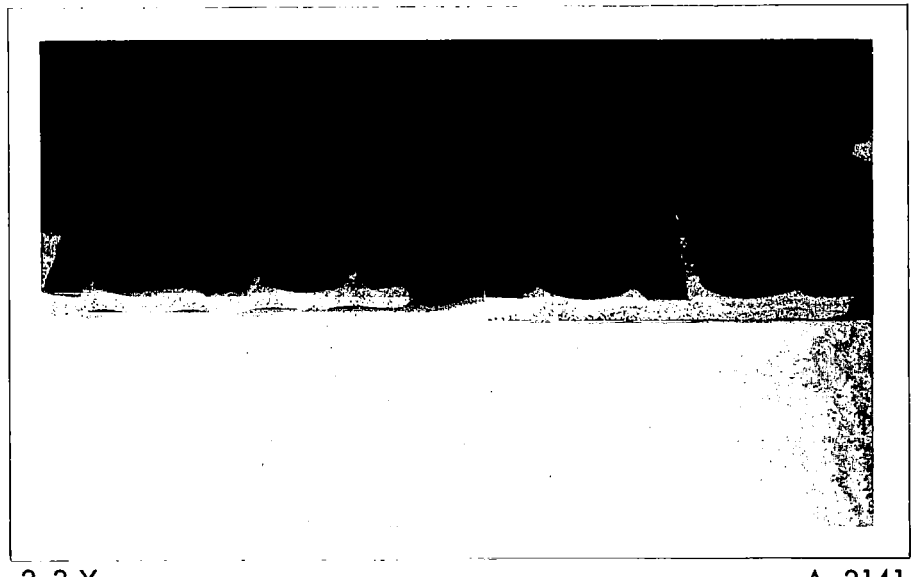

2.3 X A-2141

SHEET SAMPLES PRESSED ON STEEL DIE - END VIEW

Figure 37

APPENDIX III

CLASSIFICATION OF SPHERICAL TUNGSTEN POWDER

As the program developed, it became apparent that tungsten microspheres could be used in the direct forming process. However, in order to evaluate more fully the effect of powder particle size and particle size distribution on the forming variables and the resultant ionizer properties, additional quantities of powder were required. To meet this need, forty pounds of spherical tungsten powder was purchased from the Linde Division of Union Carbide Corporation. The classification and evaluation of this powder is described in this appendix.

Starting Powder

This powder was bought with the intent that it would be classified by Vortec Products Company into various cuts for use in subsequent ionizer fabrication. It was purchased to a particle size specification of 75% by weight less than 10 microns. Total impurities were not to exceed 500 ppm. Figure 38 shows the particle size distribution of the 40 lbs. of spherical tungsten as received from Linde. These curves compare a weight distribution by Micromerograph, a weight distribution by Coulter counter and a weight distribution calculated from particle count. It is apparent that by any of the three methods of particle size analysis the powder meets the specification requirement of 75% by weight less than 10 microns. The weight distribution calculated from particle count indicates a smaller number of large particles than is shown by the Micromerograph or by the Coulter Counter. This is attributed to the fact that in the particle counting method agglomerates are not counted as single large particles but are either ignored or the individual particles making up the agglomerate are counted. For the end use of the powder, this is felt to be a valid evaluation since the shape of the particles making up the agglomerate is spherical and the adjoining particles should form around the agglomerate to provide uniform packing. In addition most, if not all, of the agglomerates must be loosely bound or else they would appear as off-size particles in the classified fractions, which was not the case.

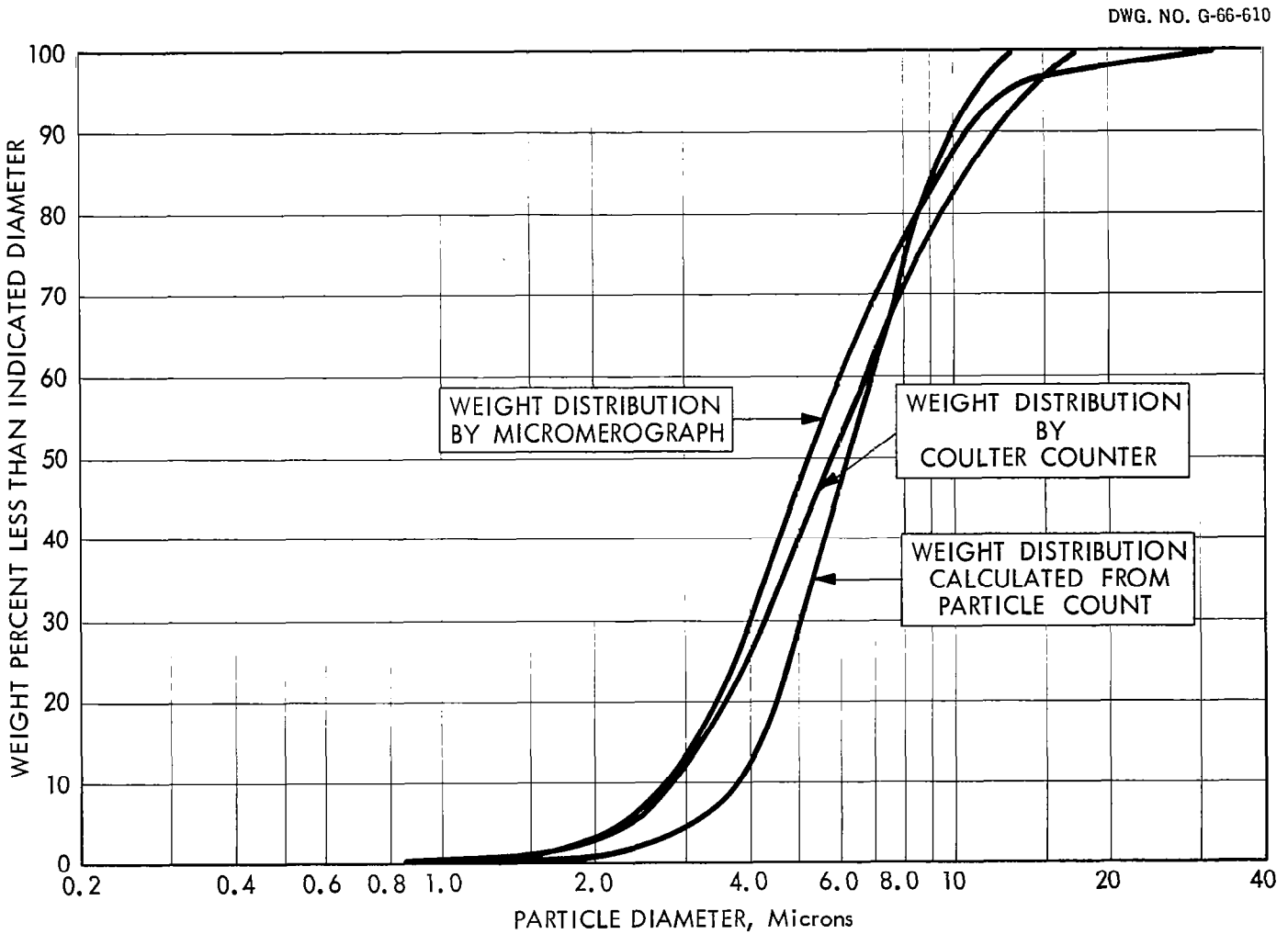

PARTICLE SIZE DISTRIBUTION OF
LINDE SPHERICAL TUNGSTEN POWDER,
LOT 2044-27, ORGDP NO. 4868-38

Figure 38

The weight distribution by Coulter Counter shows a smaller average particle size than does the distribution calculated by particle count but larger than that shown by the Micromerograph. The same applies to the indication of large particles by the three methods.

The chemical purity of the as-received powder is detailed in a following paragraph.

Classification

The classification schedule as requested from Vortec Products Company is shown in table XVI. This is also shown in figure 39 where the vertical lines represent the requested cut points. The powder was generally cut into the size fractions as requested. In addition, Vortec made an attempt to get sharper cuts on some of the fractions by making several passes through the classifier at varying cut points. The results of their evaluation are shown in the data summary in table XVII received from Vortec Products Company and in figure 40 with ORGDP powder numbers and micrographs added for each sample. Those cuts which were made a second time resulted in very low yield. Cuts of substantial quantities of powder were obtained in the range of 3 to 4 microns and up. In the 2-1/2-to 3-micron range approximately one pound of powder was obtained but in the 3- to 4-, 4- to 5-, 5- to 6-, and 7- to 8-micron ranges sufficient powder was obtained for considerable evaluation.

Evaluation

Evaluation of these cuts of classified powder included the following:

1. Particle size distribution by microscopic counting.
2. Particle size distribution by Micromerograph.

TABLE XVI

CLASSIFICATION REQUIREMENTS FOR FORTY POUNDS OF SPHERICAL TUNGSTEN POWDER 4868-38

Particle Size Fraction, microns, by Micromerograph	Estimated Product Yield, lb.
Less than 2.8	4.0
2.8 - 3.2	2.4
3.2 - 4.0	5.6
4.0 - 5.0	7.2
5.0 - 6.0	5.2
6.0 - 7.0	3.6
7.0 - 8.0	2.8
8.0 - 9.0	2.4
9.0 - 11.0	3.6
11.0 - 30.0	3.2
	40.0

Chemical Purity: All classified fractions of each powder shall be 99.9+% pure tungsten.

DWG. NO. G-66-612

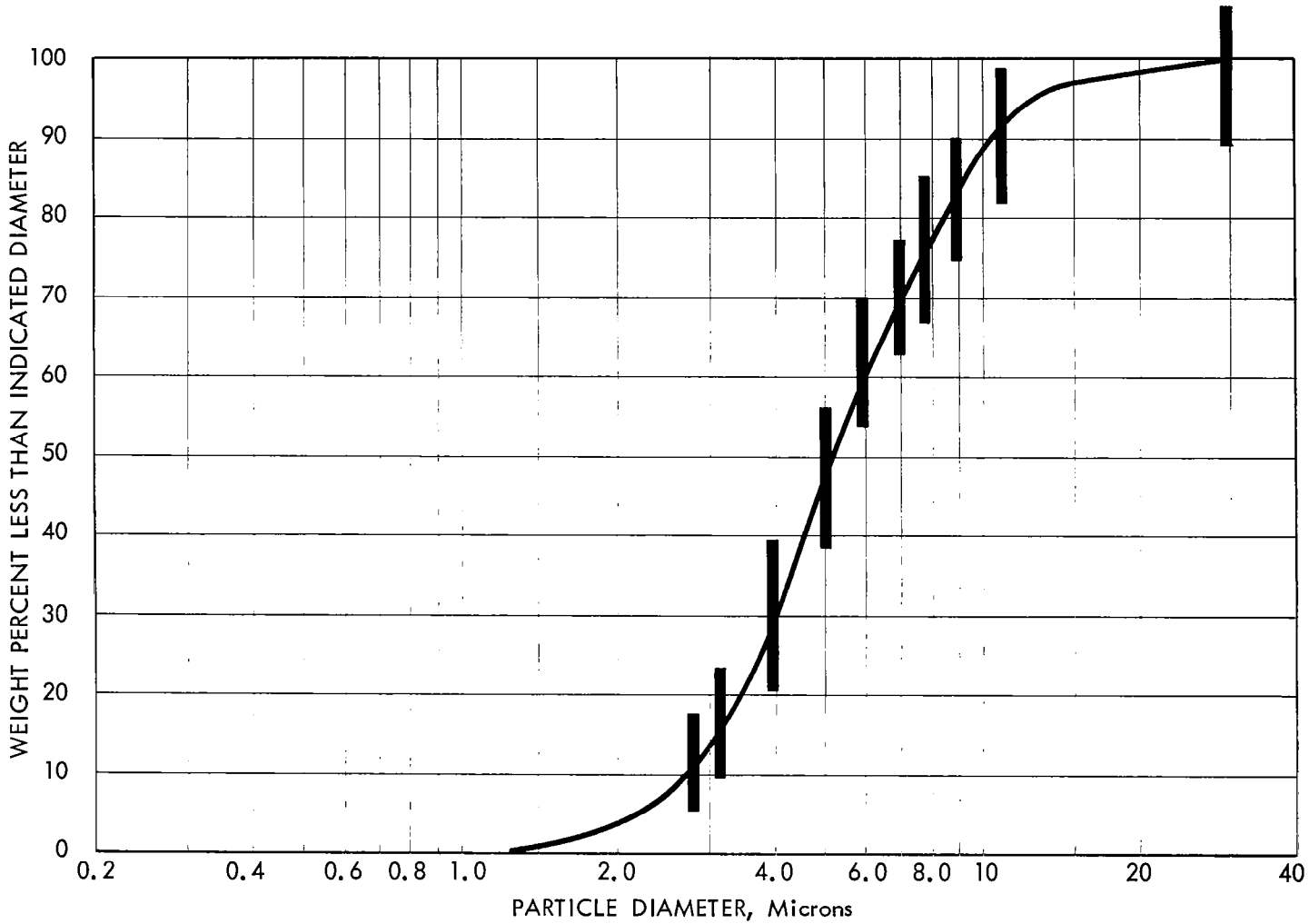

MICROMEROGRAPH PARTICLE SIZE DISTRIBUTION OF
LINDE SPHERICAL TUNGSTEN POWDER,
LOT 2044-27, ORGDP NO. 4868-38

Figure 39

TABLE XVII

POWDER CLASSIFICATION SUMMARY RECEIVED FROM VORTEC PRODUCTS COMPANY

ORGDP No.	Particle Size Fraction, microns	C-1 Throttle Setting	Product Yield, grams	% of Total Classified
4868-84	+ 11-30	+ 37%	1473.5	9.67
4868-82	+ 9-11	+ 30-37%	142.5	
		Clean Up Above (2nd)		5.16
4868-80	+ 9-11	+ 30-37%	645	
4868-78	+ 8-9	- 30%	124	
		Clean Up Above (2nd)		6.95
4868-76	+ 8-9	+ 25-30%	934	
4868-74	+ 7-8	+ 20-25%	1253.5	8.24
4868-72	+ 6-7	+ 15-20%	2067.5	13.55
4868-70	+ 5-6	- 15%	167	
		Clean Up Above (2nd)		16.85
4868-68	+ 5-6	+ 10-15%	2395.5	
4868-66	+ 4-5	+ 5-10%	2782.5	18.90
4868-64	+ 4-5	- 5%	95	
		Clean Up Above (2nd)		
4868-62	+ 3-4	+ 0-5%	2001	13.14
4868-60	+ 3-4	- 0%	692.5	4.55
		From Cut Above (2nd)		
4868-58	+ 2.5-3	- 0% (1st)	305	2.00
4868-56	+ 2.5-3	- 0%	106	0.70
4868-54	2 to 3	- 0% (3rd)	25	0.17
4868-52	- 2.8	- 0% w/insert	29	0.18

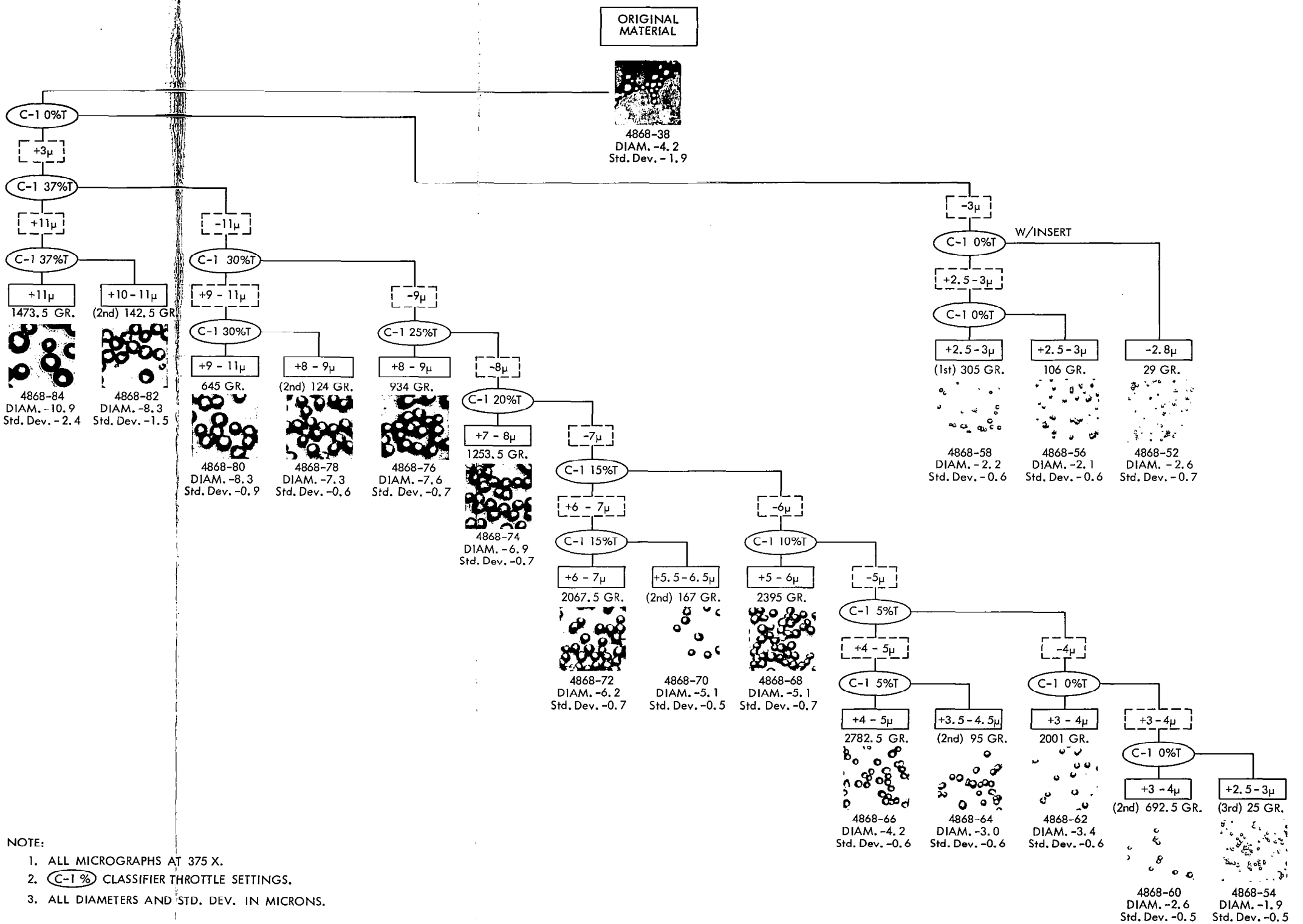

NOTE:

1. ALL MICROGRAPHS AT 375 X.
2. (C-1 %) CLASSIFIER THROTTLE SETTINGS.
3. ALL DIAMETERS AND STD. DEV. IN MICRONS.

CLASSIFICATION OF TUNGSTEN MICROSPHERES

Figure 40

~~SECRET~~

Microscopic Particle Size Distribution. Samples of the powders were dispersed on glass slides and photographed with transmitted light using a bench microscope with a 10X apochromatic objective and a 10X hyperplane eyepiece to give a magnification of 200X with the camera bellows adjustment. The resulting photographic plates were then enlarged to 500X to give prints 8-1/2 x 11. Prints were then made on thin transparent paper. Particle counts were made with the Carl Zeiss TGZ3 Particle Size Analyzer.

The TGZ3 Particle Size Analyzer employs a circular measuring mark which can be quickly varied in size to correspond exactly to the size of a particle in the field of the photograph. The operator matches the circle diameters with a particle and presses a foot switch. Simultaneously, a pin pierces the particle image on the print to indicate that it has been counted, and the count is registered in the proper size interval on the counter. After the desired number of counts have been made, it is only necessary to read from the counter the number of particles recorded in each size interval. By then making the appropriate correction for magnification, a particle diameter-frequency table is obtained.

About 2000 particles were counted for the unclassified powder, and about 500 for the classified powders. From these data, a particle size distribution was calculated. A computer program was developed to calculate the following: 1) weight distribution from particle count, 2) mean particle diameter, 3) mean total surface, 4) mean total weight. The variance, standard deviation, skewness and kertosis were also calculated for each function. Input data included the range limits as well as the average particle diameter so that either incremental or cumulative distributions could be plotted from the data. The calculation of surface area was intended to give information relating the experimental surface area obtained from the adsorption of nitrogen and krypton (BET method) to the theoretical value of surface area.

In addition to the microscopy used for counting, the various cuts were examined at 500X in reflected light. This examination revealed the sphericity of the particles and gave more information about agglomeration. Each of the powders was photographed at 500X with this "high-lighted"

effect. These micrographs are included, along with the shadowgraphs, in the summary for each powder.

Micromerograph Particle Size Distribution. The Sharples Micromerograph was used to obtain a quick indication of the average particle size. The deagglomerator was set for maximum shear and the pressure was set at 200 psi. Prior to running these samples, a standard sample was run in order to assure reliable results.

Surface Area. The surface area or specific surface per gram, was determined on each powder using well-established BET procedures and using both nitrogen and krypton as the adsorbates. Nitrogen is routinely used for high surface area powders whereas krypton gives more accurate results for larger powders with their attendant lower surface area.

Spectrochemical Analysis. Sensitivities for spectrochemical analysis are given in table XVIII. Several spectrochemical procedures are required to attain the sensitivities shown. These include a direct burn method for calcium, carrier distillation procedures for the common metals, the cupferron group separation, zinc reduction separation for the platinum group, and an ammonia precipitation separation for the rare earth elements.

Carbon Analysis. The percentage of carbon in tungsten is determined by the combustion-conductometric method. The sample is heated in a tube furnace in a stream of pure oxygen at 1400°C. The carbon is oxidized to carbon dioxide, which is absorbed in barium hydroxide solution. The decrease in conductance is measured and the amount of carbon in the sample is determined from a previously prepared calibration curve. The range is 0 to 100 micrograms of carbon with a lower limit of 5 micrograms.

Tapped Density. The packed or tapped density was obtained with the Numinco Tapak Volumeter. This instrument imparts a sharp tapping action to a 100-cc. graduate containing the powder to be measured. Tapping is continued until no further change in volume is noted. About 35 cc. of powder was used in these tests and the number of taps was standardized at 7500.

TABLE XVIII

ACHIEVED SENSITIVITIES FOR THE SPECTROCHEMICAL PROCEDURES FOR IMPURITIES IN TUNGSTEN

Element	Limit of Detection	Element	Limit of Detection	Element	Limit of Detection
Ag	1	Hg	2	Sn	1
Al	1	In	1	Sr	1
As	3	Ir	1	Ta	1
Au	1	K	1	Th	0.5
B	1	Li	1	Ti	1
Ba	1	Mg	1	Tl	1
Be	0.1	Mn	1	V	1
Bi	1	Mo	1	Zn	15
Ca	1	Na	5	Zr	1
Cb	1	Ni	1	Rare Earths	
Cd	1	P	5		
Co	3	Pb	1	Ce	1
Cr	3	Pd	1	Dy	0.5
Cs	10	Pt	1	Er	0.5
Cu	0.1	Rb	5	Eu	0.5
Fe	1	Rh	1	Gd	0.5
Ga	1	Ru	1	Ho	0.5
Ge	1	Sb	1	La	0.5
Hf	1	Si	1	Lu	0.5
				Nd	0.5
				Pr	0.5
				Sm	0.5
				Tb	0.5
				Tm	0.5
				Yb	0.5

Summary. A summary of the properties of each powder is given in figures 41 thru 61 and the table facing each figure. Cumulative distributions by particle count, by weight calculated from particle count and by Micromerograph are shown for each powder. An incremental frequency distribution, although not as useful for most purposes, is also shown. The shadowgraphs of the type used for particle counting and highlighted micrographs are also included. The prints were made originally at 500X and were reduced to the magnification shown in reproduction.

Data on the unclassified starting powder as received from Linde are shown first, figure 41. Following this are the data summaries on the cuts obtained on this 40 lbs. of powder, figures 42 thru 58. Finally, for comparison are data on the three cuts of microspheres purchased from Linde early in the contract, figures 59 thru 61. Average values for the particle size parameters are summarized in table XXXX.

The results of the chemical and spectrochemical analyses of the powder both before and after classification are shown in tables XXXXI and XXXXII. The cut selected for analysis after classification is one containing a relatively large amount of material. The largest increase in impurity is seen from table XXXXI to be carbon which has increased from 42 ppm. to 220 ppm. This is thought to occur from the abrading action of the tungsten particles on a polyurethane coating on the rotor and other parts of the classifier. This is not considered serious in view of the demonstrated reduction in carbon accomplished by sintering in high purity hydrogen. Even with carbon at this level, the total impurity level is almost within the specifications for the original powder. The greatest increases appear to be in calcium, magnesium, and silicon which is not surprising considering the residence time in the classifier and the relatively large abrading forces which result during classification.

Figure 62 compares the surface area of the microspheres obtained experimentally from nitrogen and krypton adsorption with that obtained by summing the surface area obtained in each increment of powder from the count data. As a line of reference, the surface area calculated

Pages 120 through 161 illustrate Particle Size Distribution and Photomicrographs of Tungsten Microspheres with corresponding Powder Properties

ORGDP NO. 4868-38

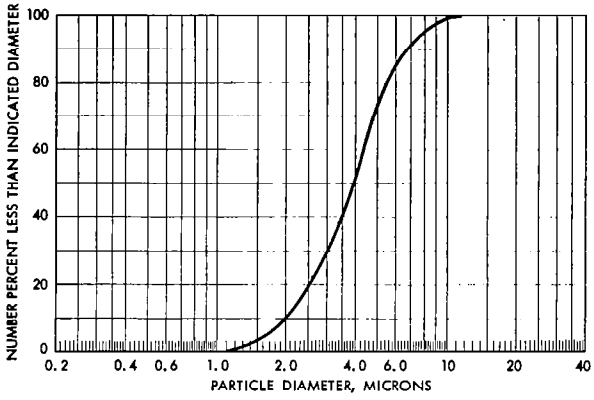

A. Cumulative Number Percent by Particle Count

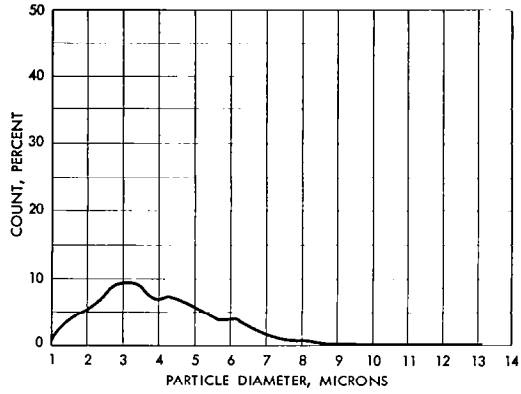

D. Frequency Plot from Particle Count

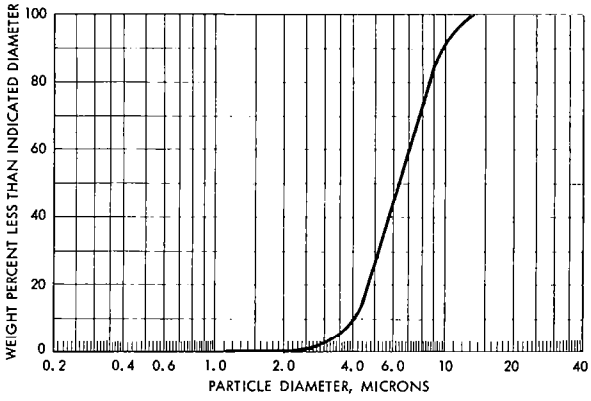

B. Cumulative Weight Percent Calculated from Particle Count

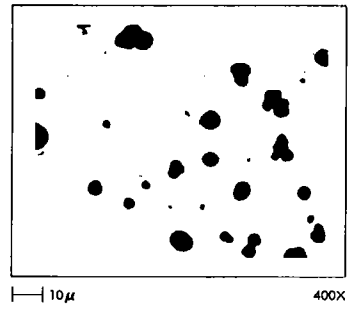

E. Shadowgraphs for Particle Counting

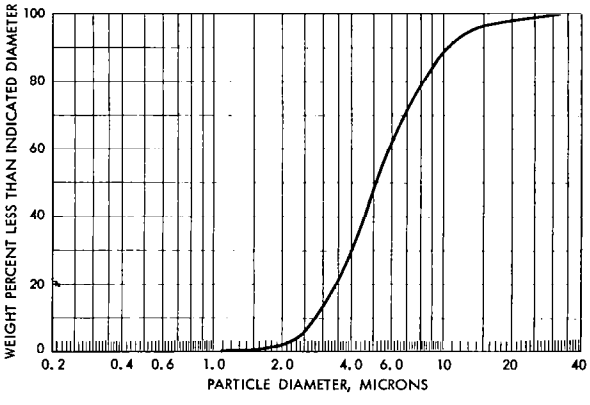

C. Cumulative Weight Percent by Micromerograph

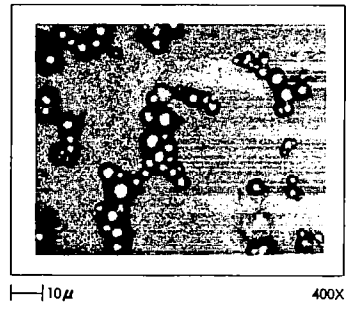

F. Highlighted Micrographs

PARTICLE SIZE DISTRIBUTIONS AND
PHOTOMICROGRAPHS OF TUNGSTEN MICROSPHERES

Figure 41

POWDER PROPERTIES

IDENTIFICATION: Original Material ORGDP NO. 4868-38

SIZE:

Particle Count, Arithmetic Mean Diameter	4.2	Microns
Arithmetic Standard Deviation	1.9	Microns
Micromerograph Mean Diameter	5.2	Microns
Weight Percent Calculated from Particle Count, Mean Diameter	6.5	Microns
Calculated from Nitrogen Surface Area	3.2	Microns
Calculated from Krypton Surface Area	2.9	Microns

SURFACE AREA:

From Nitrogen Adsorption	0.098	sq. m./g
From Krypton Adsorption	0.106	sq. m./g

TAPPED DENSITY	--	g./cc
CARBON CONTAMINATION	42	ppm

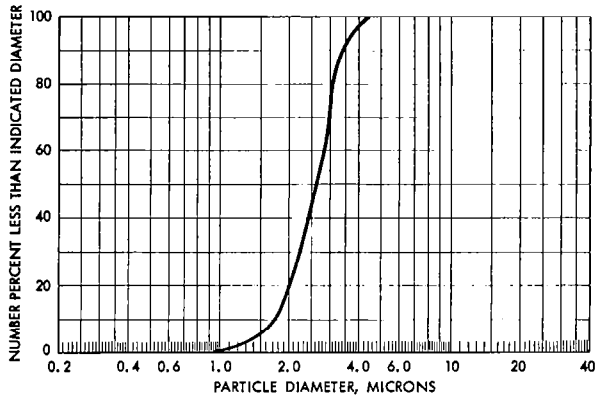

A. Cumulative Number Percent by Particle Count

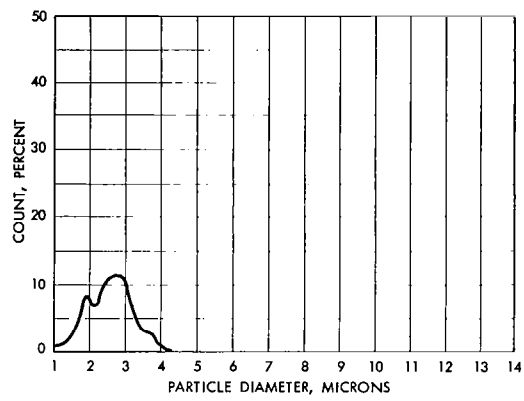

D. Frequency Plot from Particle Count

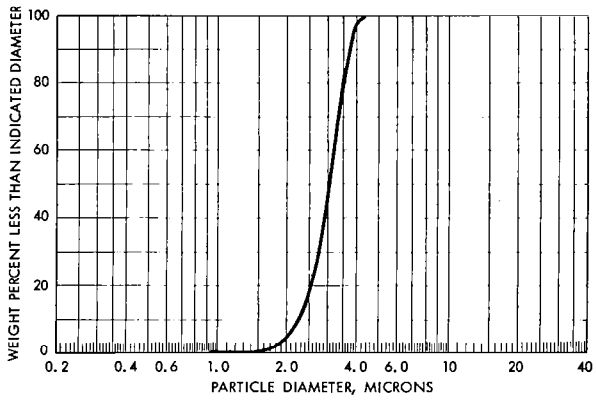

B. Cumulative Weight Percent Calculated from Particle Count

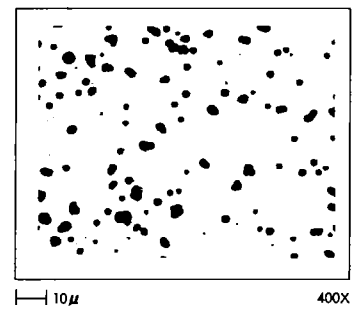

E. Shadowgraphs for Particle Counting

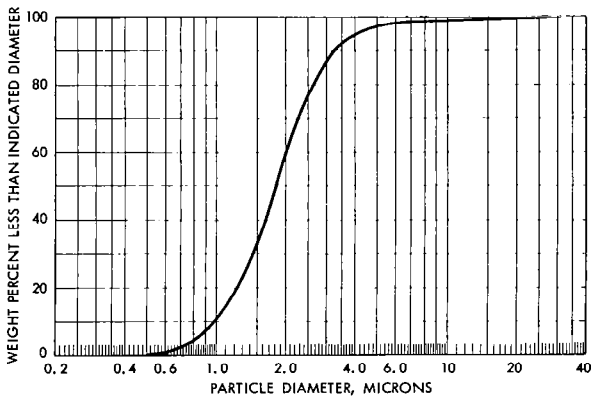

C. Cumulative Weight Percent by Micromerograph

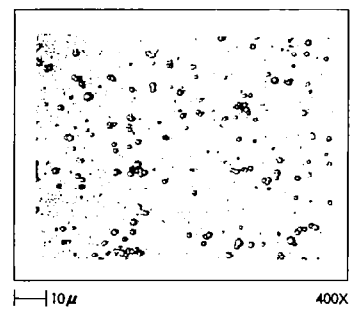

F. Highlighted Micrographs

PARTICLE SIZE DISTRIBUTIONS AND
PHOTOMICROGRAPHS OF TUNGSTEN MICROSPHERES

Figure 42

POWDER PROPERTIES

IDENTIFICATION: -2.8 _____ ORGDP NO. 4868-52

SIZE:

Particle Count, Arithmetic Mean Diameter	2.6	Microns
Arithmetic Standard Deviation	0.7	Microns
Micromerograph Mean Diameter	1.8	Microns
Weight Percent Calculated from Particle Count, Mean Diameter	3.0	Microns
Calculated from Nitrogen Surface Area	0.9	Microns
Calculated from Krypton Surface Area	1.0	Microns

SURFACE AREA:

From Nitrogen Adsorption	0.334	sq.m./g
From Krypton Adsorption	0.316	sq.m./g

TAPPED DENSITY -- g./cc

CARBON CONTAMINATION _____ ppm

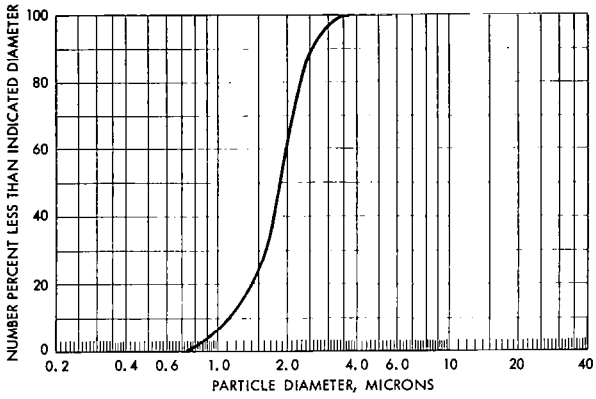

A. Cumulative Number Percent by Particle Count

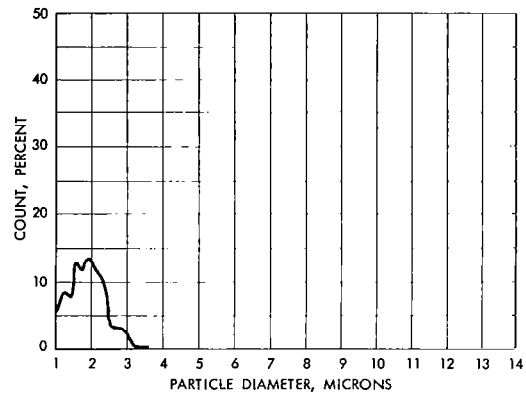

D. Frequency Plot from Particle Count

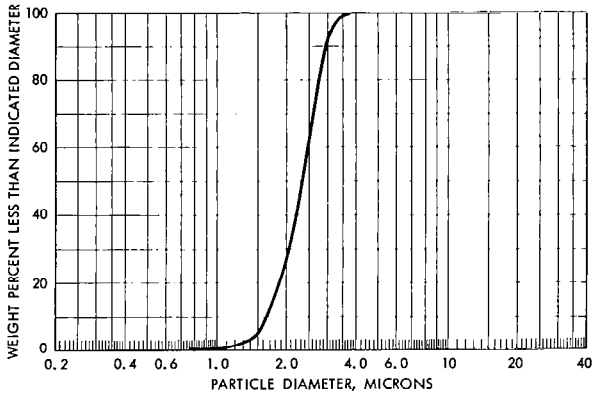

B. Cumulative Weight Percent Calculated from Particle Count

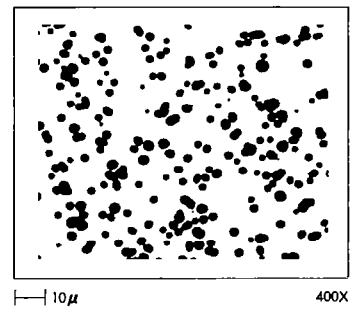

E. Shadowgraphs for Particle Counting

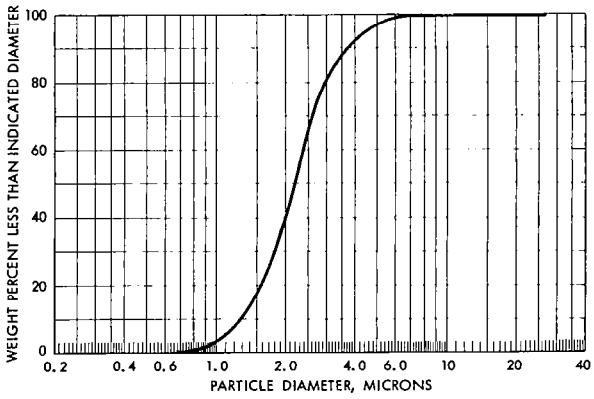

C. Cumulative Weight Percent by Micromerograph

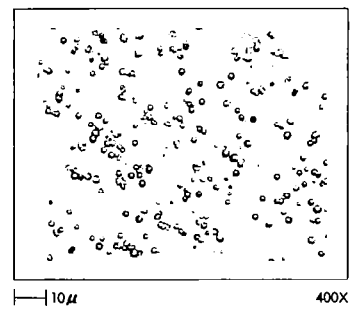

F. Highlighted Micrographs

PARTICLE SIZE DISTRIBUTIONS AND
PHOTOMICROGRAPHS OF TUNGSTEN MICROSPHERES

Figure 43

POWDER PROPERTIES

IDENTIFICATION: 2-3, 3rd ORGDP NO. 4868-54

SIZE:

Particle Count, Arithmetic Mean Diameter	1.9	Microns
Arithmetic Standard Deviation	0.5	Microns
Micromerograph Mean Diameter	2.2	Microns
Weight Percent Calculated from Particle Count, Mean Diameter	2.3	Microns
Calculated from Nitrogen Surface Area	1.2	Microns
Calculated from Krypton Surface Area	1.3	Microns

SURFACE AREA:

From Nitrogen Adsorption	0.253	sq. m./g
From Krypton Adsorption	0.241	sq. m./g

TAPPED DENSITY -- g./cc

CARBON CONTAMINATION _____ ppm

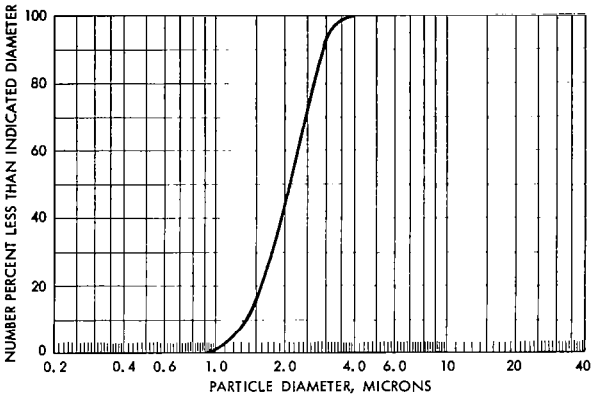

A. Cumulative Number Percent by Particle Count

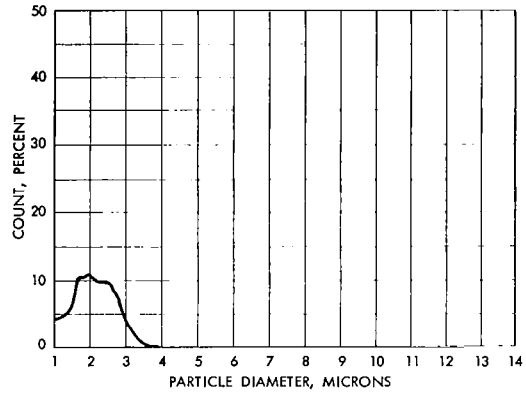

D. Frequency Plot from Particle Count

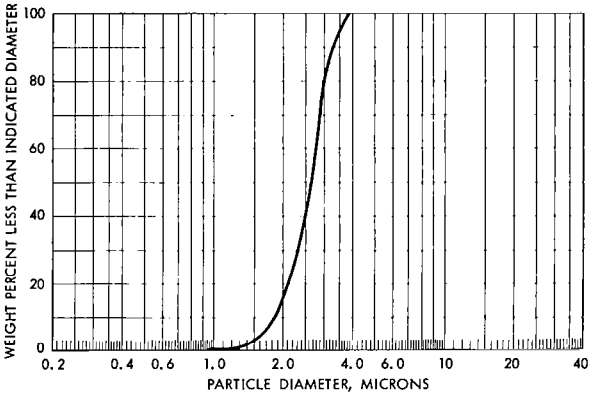

B. Cumulative Weight Percent Calculated from Particle Count

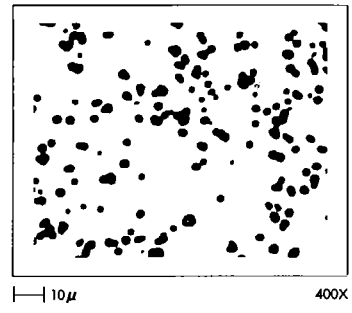

E. Shadowgraphs for Particle Counting

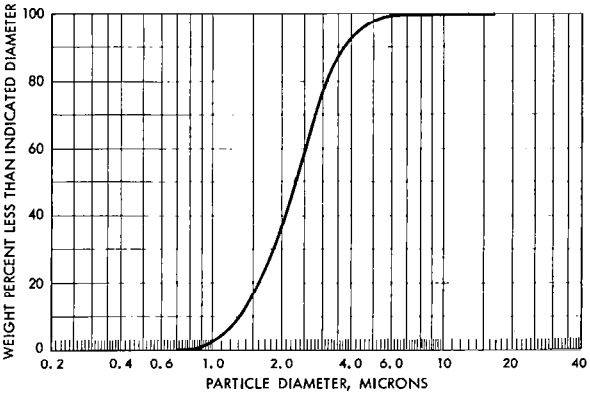

C. Cumulative Weight Percent by Micromerograph

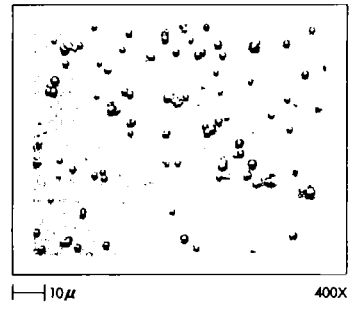

F. Highlighted Micrographs

PARTICLE SIZE DISTRIBUTIONS AND
PHOTOMICROGRAPHS OF TUNGSTEN MICROSPHERES

Figure 44

POWDER PROPERTIES

IDENTIFICATION: + 2.5-3 ORGDP NO. 4868-56

SIZE:

Particle Count, Arithmetic Mean Diameter	2.1	Microns
Arithmetic Standard Deviation	0.6	Microns
Micromerograph Mean Diameter	2.3	Microns
Weight Percent Calculated from Particle Count, Mean Diameter	2.6	Microns
Calculated from Nitrogen Surface Area	1.4	Microns
Calculated from Krypton Surface Area	1.3	Microns

SURFACE AREA:

From Nitrogen Adsorption	0.225	sq. m./g
From Krypton Adsorption	0.238	sq. m./g

TAPPED DENSITY -- g./cc

CARBON CONTAMINATION ppm

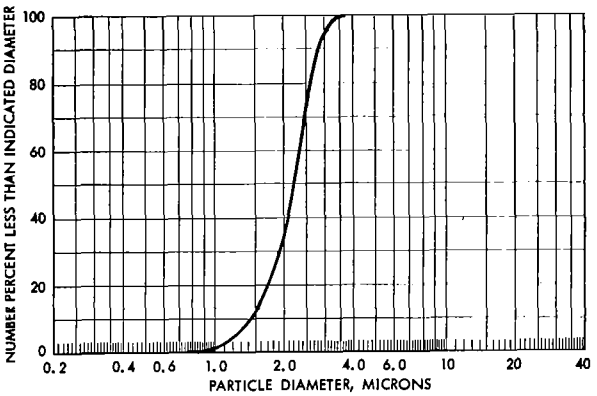

A. Cumulative Number Percent by Particle Count

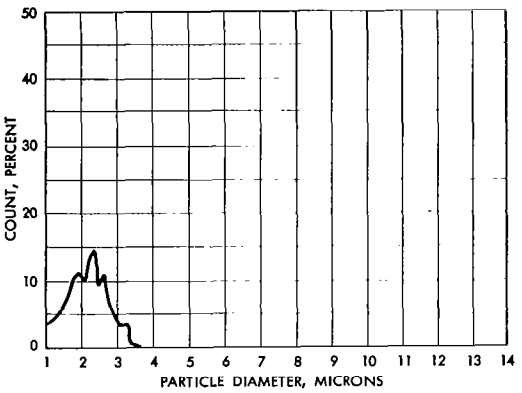

D. Frequency Plot from Particle Count

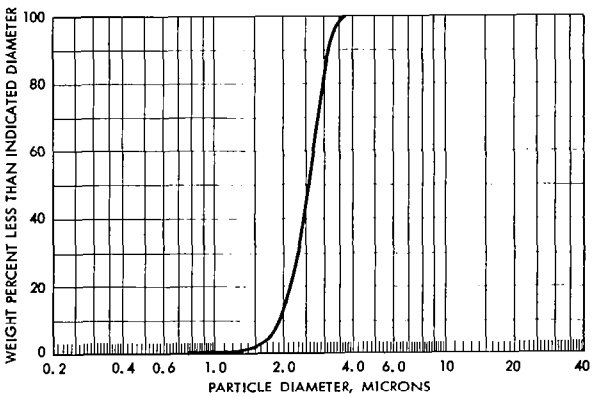

B. Cumulative Weight Percent Calculated from Particle Count

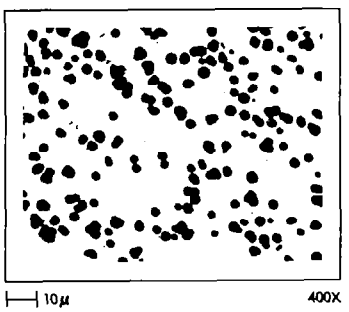

E. Shadowgraphs for Particle Counting

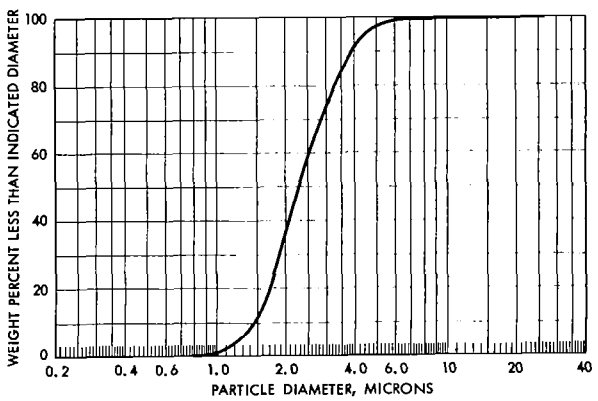

C. Cumulative Weight Percent by Micromerograph

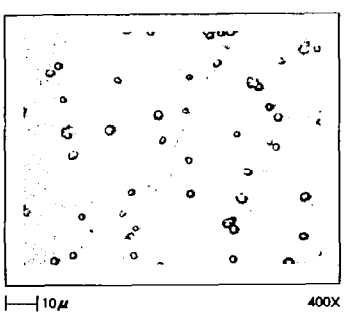

F. Highlighted Micrographs

PARTICLE SIZE DISTRIBUTIONS AND
PHOTOMICROGRAPHS OF TUNGSTEN MICROSPHERES

Figure 45

POWDER PROPERTIES

IDENTIFICATION: + 2.5-3, 1st _____ ORGDP NO. 4868-58

SIZE:

Particle Count, Arithmetic Mean Diameter	2.2	Microns
Arithmetic Standard Deviation	0.6	Microns
Micromerograph Mean Diameter	2.4	Microns
Weight Percent Calculated from Particle Count, Mean Diameter	2.6	Microns
Calculated from Nitrogen Surface Area	1.3	Microns
Calculated from Krypton Surface Area	1.4	Microns

SURFACE AREA:

From Nitrogen Adsorption	0.240	sq. m./g
From Krypton Adsorption	0.217	sq. m./g

TAPPED DENSITY	9.73	g./cc
CARBON CONTAMINATION	190	ppm

ORGDP NO. 4868-60

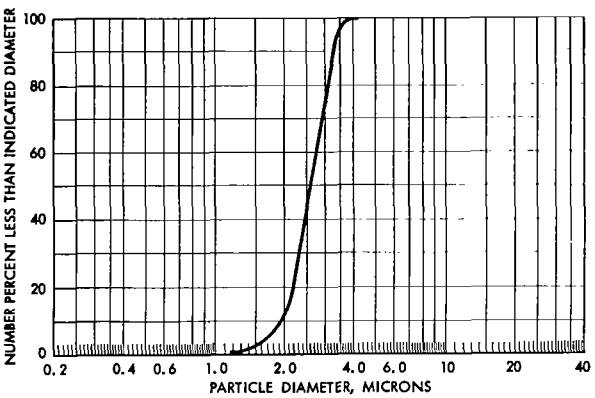

A. Cumulative Number Percent by Particle Count

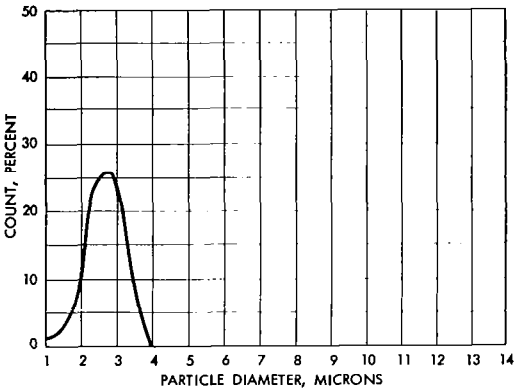

D. Frequency Plot from Particle Count

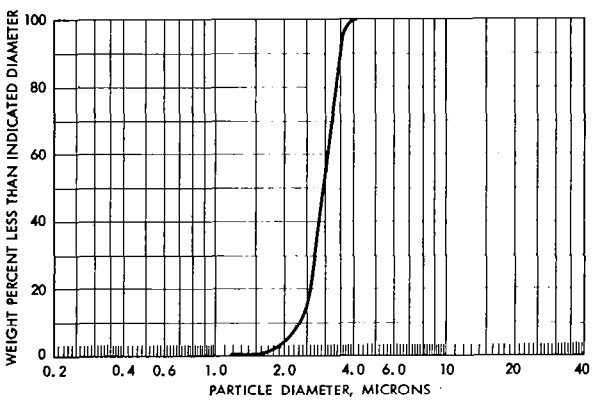

B. Cumulative Weight Percent Calculated from Particle Count

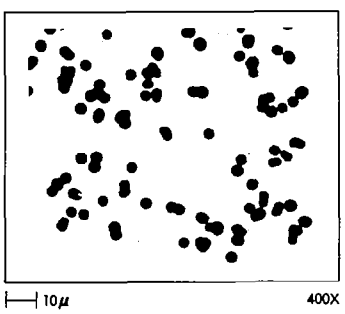

E. Shadowgraphs for Particle Counting

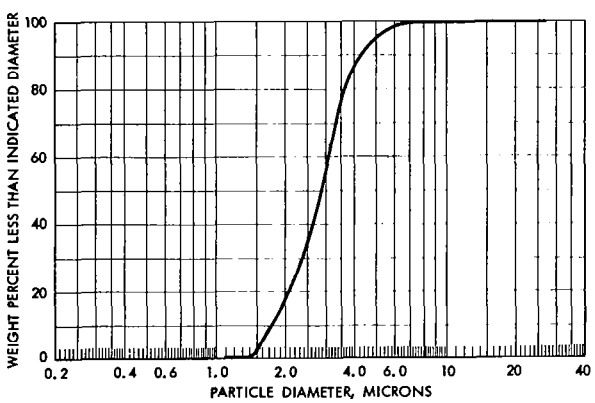

C. Cumulative Weight Percent by Micromerograph

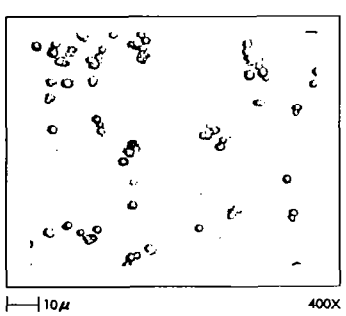

F. Highlighted Micrographs

PARTICLE SIZE DISTRIBUTIONS AND
PHOTOMICROGRAPHS OF TUNGSTEN MICROSPHERES

Figure 46

POWDER PROPERTIES

IDENTIFICATION: + 3-4, 2nd ORGDP NO. 4868-60

SIZE:		
Particle Count, Arithmetic Mean Diameter	2.6	Microns
Arithmetic Standard Deviation	0.5	Microns
Micromerograph Mean Diameter	2.9	Microns
Weight Percent Calculated from Particle Count, Mean Diameter	3.1	Microns
Calculated from Nitrogen Surface Area	1.8	Microns
Calculated from Krypton Surface Area	2.2	Microns
SURFACE AREA:		
From Nitrogen Adsorption	0.169	sq. m./g
From Krypton Adsorption	0.140	sq. m./g
TAPPED DENSITY	10.54	g./cc
CARBON CONTAMINATION	100	ppm

ORGDP NO. 4868-62

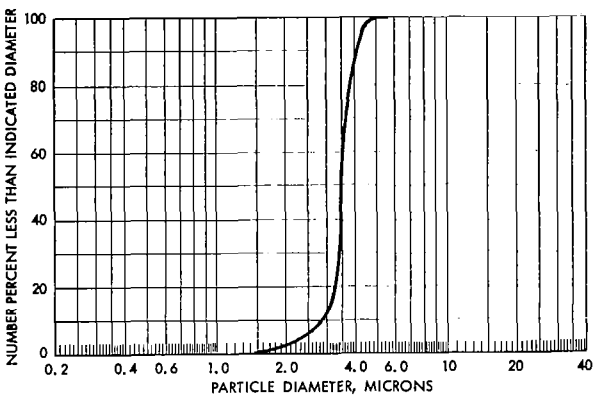

A. Cumulative Number Percent by Particle Count

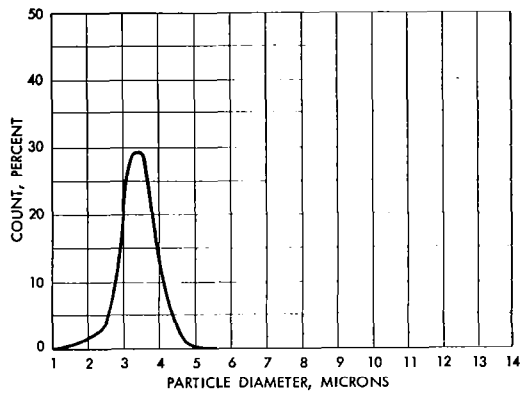

D. Frequency Plot from Particle Count

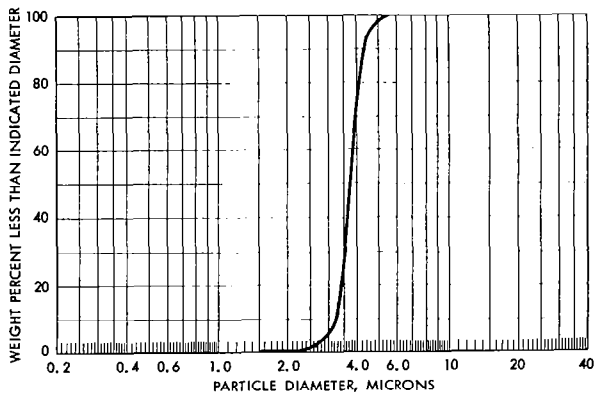

B. Cumulative Weight Percent Calculated from Particle Count

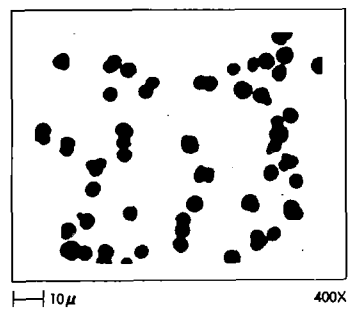

E. Shadowgraphs for Particle Counting

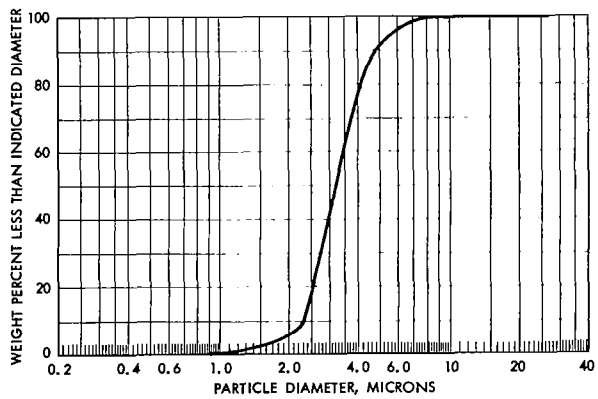

C. Cumulative Weight Percent by Micromerograph

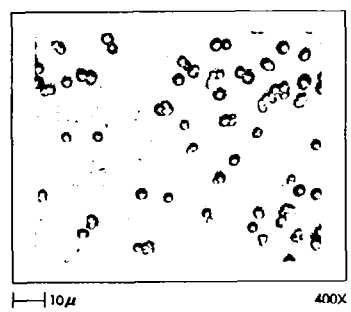

F. Highlighted Micrographs

PARTICLE SIZE DISTRIBUTIONS AND
PHOTOMICROGRAPHS OF TUNGSTEN MICROSPHERES

Figure 47

POWDER PROPERTIES

IDENTIFICATION: + 3-4 ORGDP NO. 4868-62

SIZE:

Particle Count, Arithmetic Mean Diameter	3.5	Microns
Arithmetic Standard Deviation	0.6	Microns
Micromerograph Mean Diameter	3.3	Microns
Weight Percent Calculated from Particle Count, Mean Diameter	3.7	Microns
Calculated from Nitrogen Surface Area	2.2	Microns
Calculated from Krypton Surface Area	2.8	Microns

SURFACE AREA:

From Nitrogen Adsorption	0.139	sq. m./g
From Krypton Adsorption	0.110	sq. m./g

TAPPED DENSITY	10.96	g./cc
CARBON CONTAMINATION	75	ppm

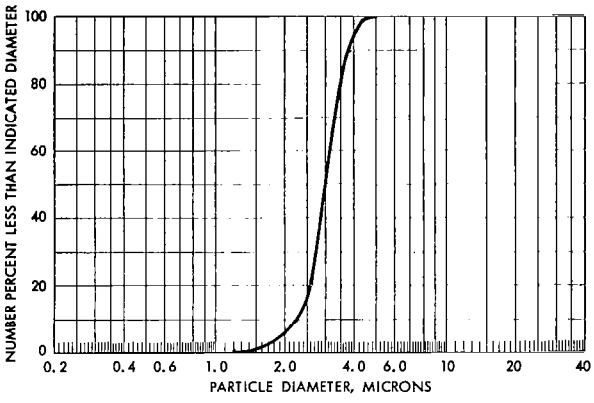

A. Cumulative Number Percent by Particle Count

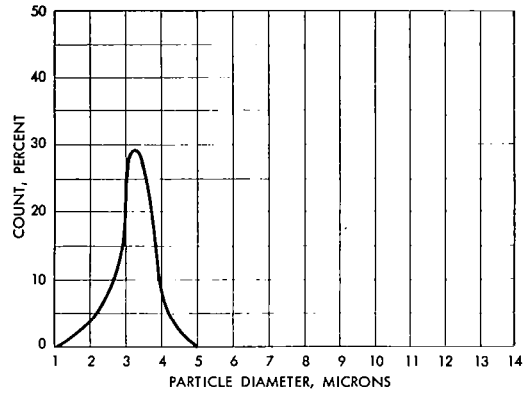

D. Frequency Plot from Particle Count

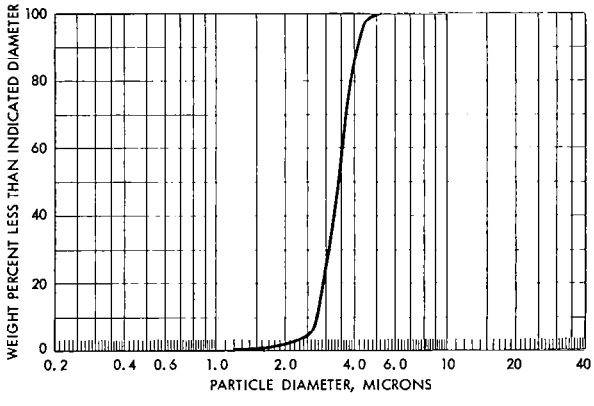

B. Cumulative Weight Percent Calculated from Particle Count

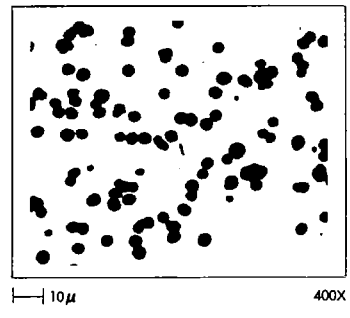

E. Shadowgraphs for Particle Counting

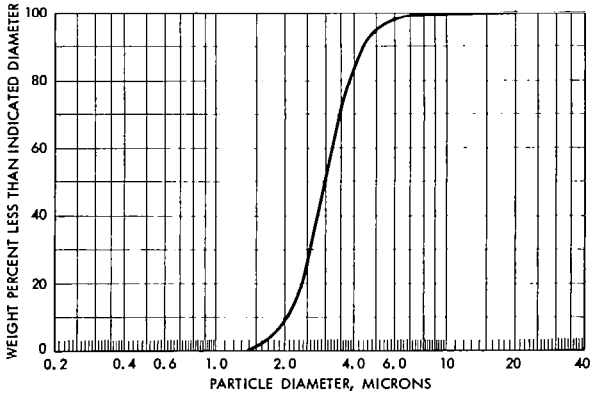

C. Cumulative Weight Percent by Micromerograph

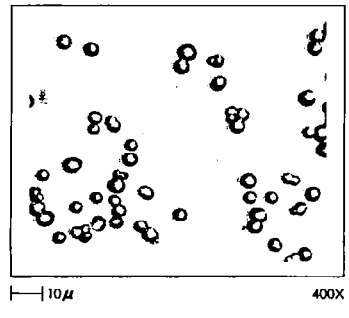

F. Highlighted Micrographs

PARTICLE SIZE DISTRIBUTIONS AND
PHOTOMICROGRAPHS OF TUNGSTEN MICROSPHERES

Figure 48

POWDER PROPERTIES

IDENTIFICATION: + 4-5, 2nd ORGDP NO. 4868-64

SIZE:

Particle Count, Arithmetic Mean Diameter	3.0	Microns
Arithmetic Standard Deviation	0.6	Microns
Micromerograph Mean Diameter	3.0	Microns
Weight Percent Calculated from Particle Count, Mean Diameter	3.3	Microns
Calculated from Nitrogen Surface Area	2.3	Microns
Calculated from Krypton Surface Area	2.4	Microns

SURFACE AREA:

From Nitrogen Adsorption	0.135	sq.m./g
From Krypton Adsorption	0.130	sq.m./g

TAPPED DENSITY -- g./cc

CARBON CONTAMINATION _____ ppm

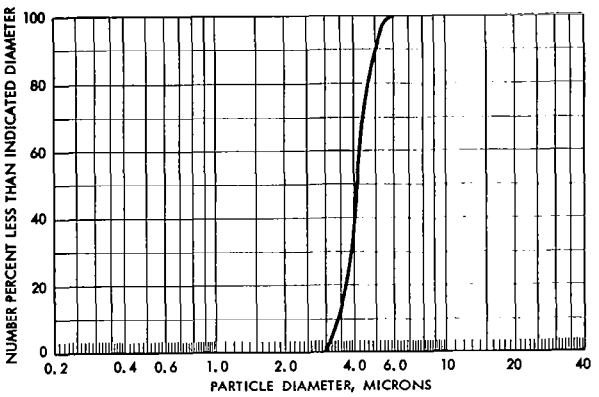

A. Cumulative Number Percent by Particle Count

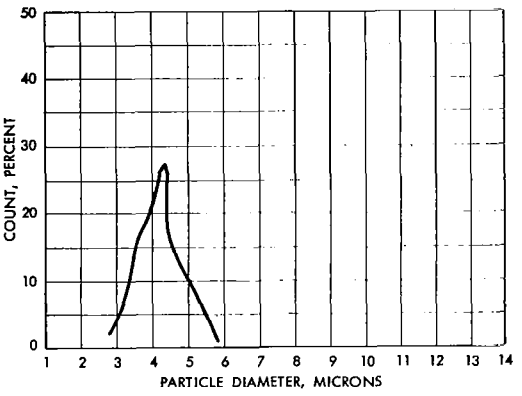

D. Frequency Plot from Particle Count

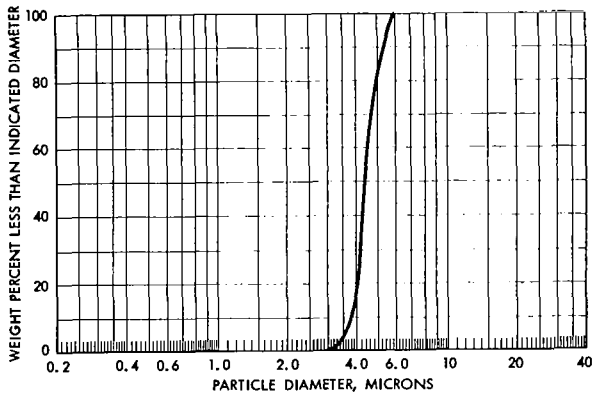

B. Cumulative Weight Percent Calculated from Particle Count

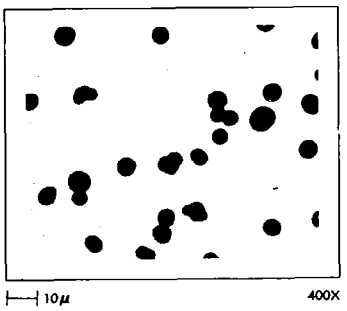

E. Shadowgraphs for Particle Counting

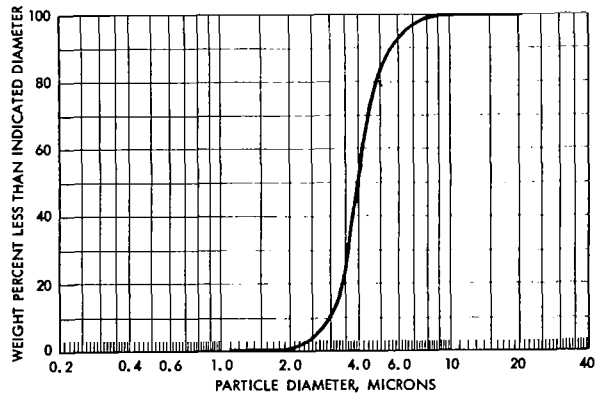

C. Cumulative Weight Percent by Micromerograph

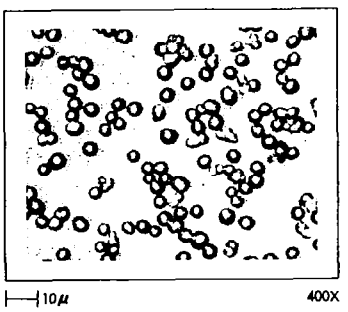

F. Highlighted Micrographs

PARTICLE SIZE DISTRIBUTIONS AND
PHOTOMICROGRAPHS OF TUNGSTEN MICROSPHERES

Figure 49

POWDER PROPERTIES

IDENTIFICATION: + 4-5 ORGDP NO. 4868-66

SIZE:

Particle Count, Arithmetic Mean Diameter	4.2	Microns
Arithmetic Standard Deviation	0.6	Microns
Micromerograph Mean Diameter	4.1	Microns
Weight Percent Calculated from Particle Count, Mean Diameter	4.2	Microns
Calculated from Nitrogen Surface Area	3.1	Microns
Calculated from Krypton Surface Area	3.3	Microns

SURFACE AREA:

From Nitrogen Adsorption	0.101	sq. m./g
From Krypton Adsorption	0.093	sq. m./g

TAPPED DENSITY 11.07 g./cc

CARBON CONTAMINATION _____ ppm

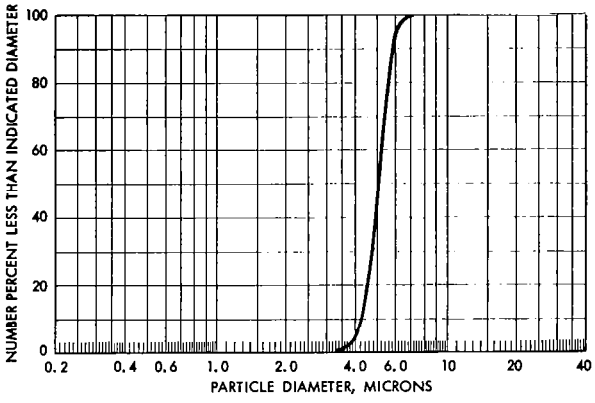

A. Cumulative Number Percent by Particle Count

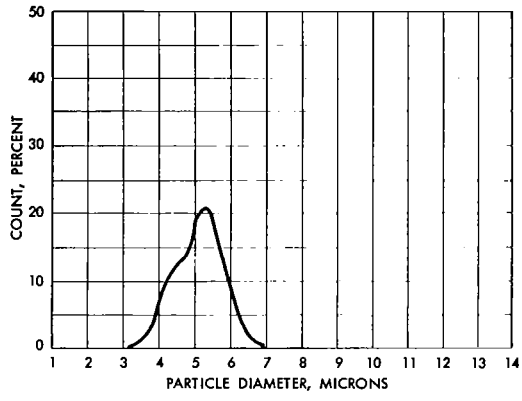

D. Frequency Plot from Particle Count

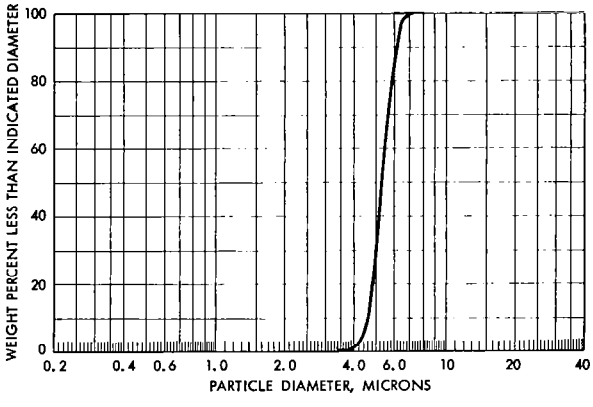

B. Cumulative Weight Percent Calculated from Particle Count

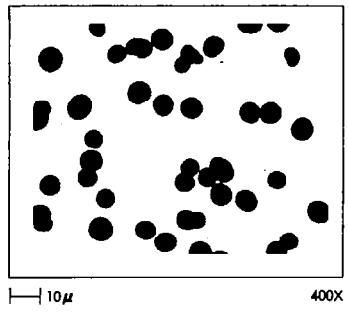

E. Shadowgraphs for Particle Counting

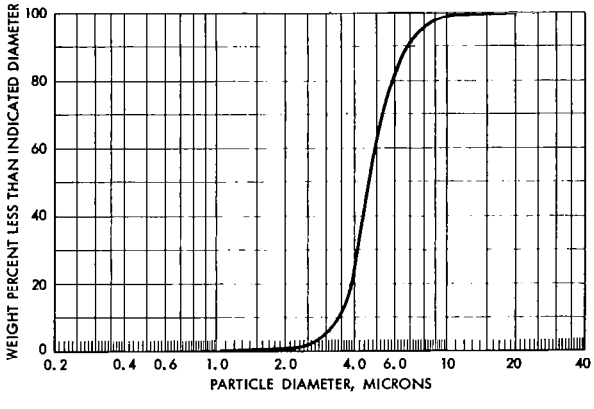

C. Cumulative Weight Percent by Micromerograph

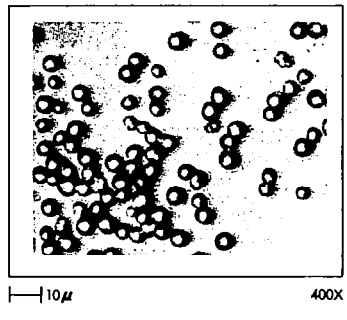

F. Highlighted Micrographs

PARTICLE SIZE DISTRIBUTIONS AND
PHOTOMICROGRAPHS OF TUNGSTEN MICROSPHERES

Figure 50

POWDER PROPERTIES

IDENTIFICATION: + 5-6 _____ ORGDP NO. 4868-68

SIZE:

Particle Count, Arithmetic Mean Diameter	5.1	Microns
Arithmetic Standard Deviation	0.6	Microns
Micromerograph Mean Diameter	4.7	Microns
Weight Percent Calculated from Particle Count, Mean Diameter	5.2	Microns
Calculated from Nitrogen Surface Area	4.0	Microns
Calculated from Krypton Surface Area	4.0	Microns

SURFACE AREA:

From Nitrogen Adsorption	0.078	sq. m./g
From Krypton Adsorption	0.077	sq. m./g

TAPPED DENSITY	10.72	g./cc
CARBON CONTAMINATION	_____	ppm

ORGDP NO. 4868-70

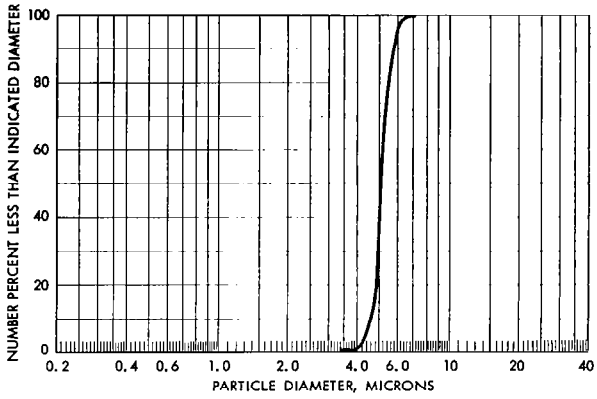

A. Cumulative Number Percent by Particle Count

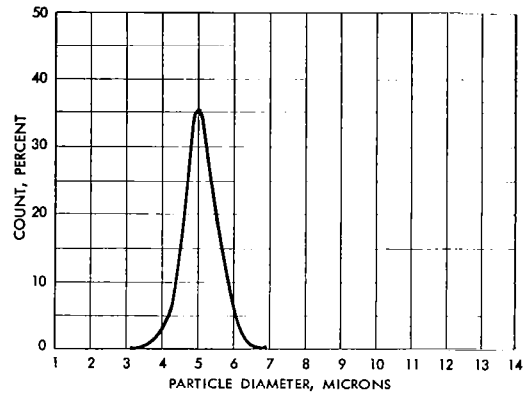

D. Frequency Plot from Particle Count

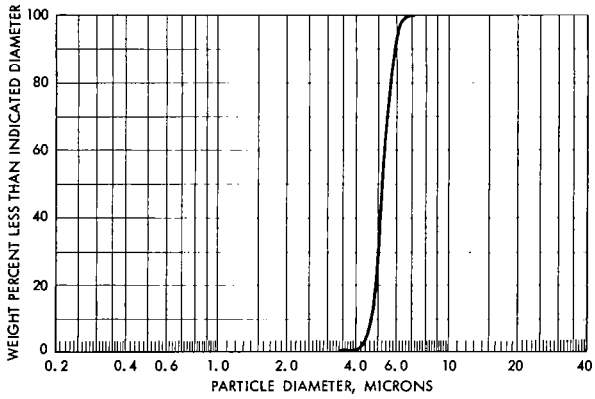

B. Cumulative Weight Percent Calculated from Particle Count

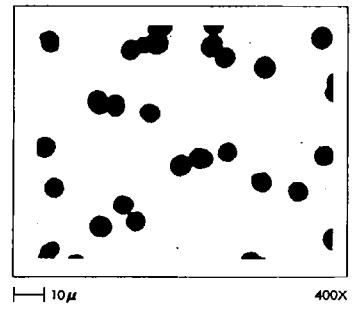

E. Shadowgraphs for Particle Counting

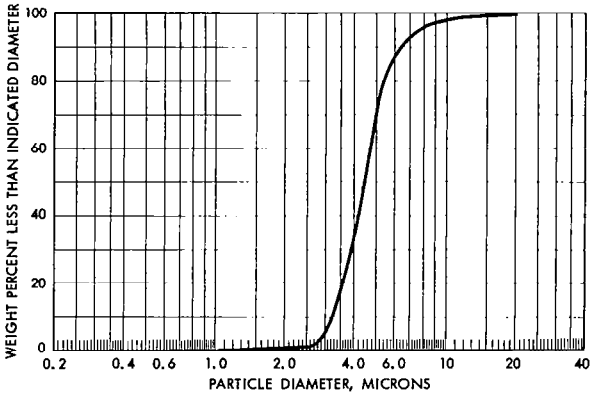

C. Cumulative Weight Percent by Micromerograph

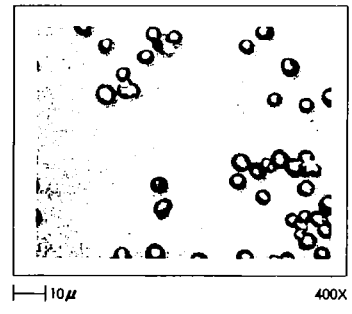

F. Highlighted Micrographs

PARTICLE SIZE DISTRIBUTIONS AND
PHOTOMICROGRAPHS OF TUNGSTEN MICROSPHERES

Figure 51

POWDER PROPERTIES

IDENTIFICATION: + 5-6, 2nd ORGDP NO. 4868-70

SIZE:

Particle Count, Arithmetic Mean Diameter	5.1	Microns
Arithmetic Standard Deviation	0.5	Microns
Micromerograph Mean Diameter	4.3	Microns
Weight Percent Calculated from Particle Count, Mean Diameter	5.2	Microns
Calculated from Nitrogen Surface Area	3.8	Microns
Calculated from Krypton Surface Area	4.8	Microns

SURFACE AREA:

From Nitrogen Adsorption	0.081	sq.m./g
From Krypton Adsorption	0.065	sq.m./g

TAPPED DENSITY -- g./cc

CARBON CONTAMINATION ____ ppm

ORGDP NO. 4868-72

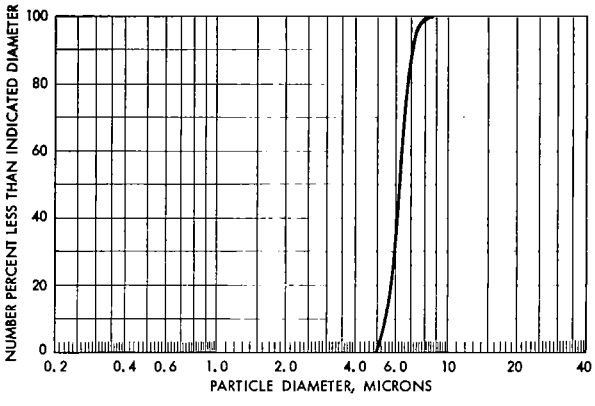

A. Cumulative Number Percent by Particle Count

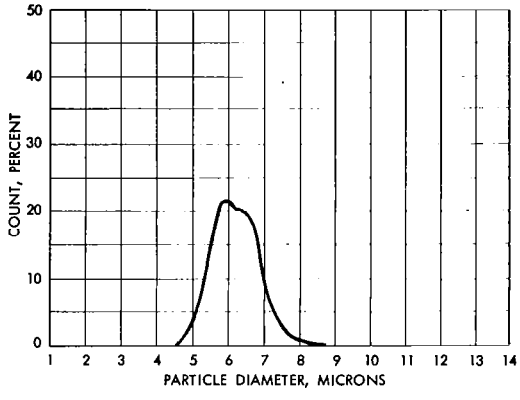

D. Frequency Plot from Particle Count

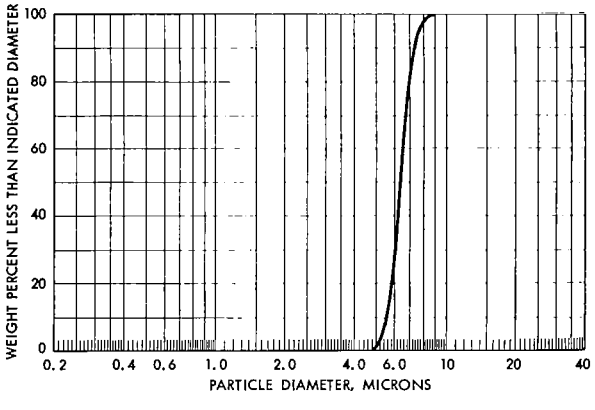

B. Cumulative Weight Percent Calculated from Particle Count

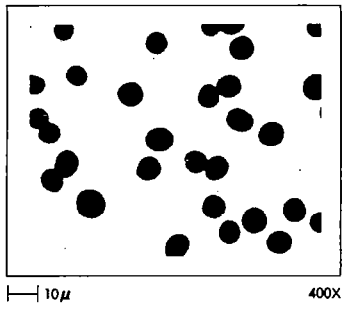

E. Shadowgraphs for Particle Counting

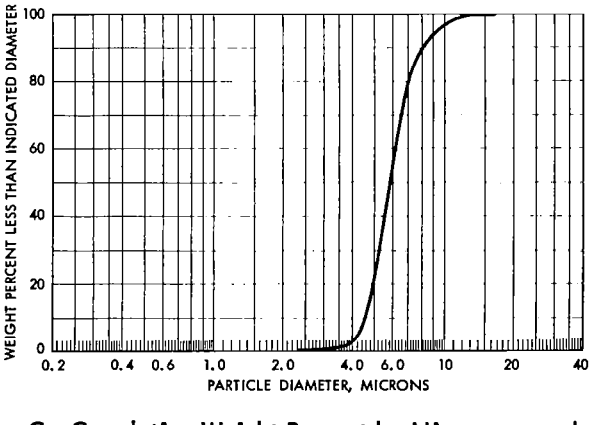

C. Cumulative Weight Percent by Micromerograph

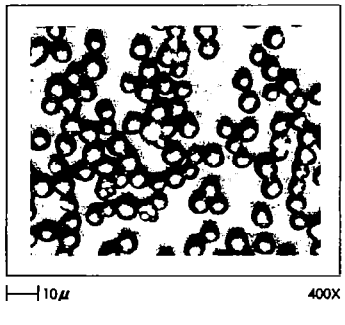

F. Highlighted Micrographs

PARTICLE SIZE DISTRIBUTIONS AND
PHOTOMICROGRAPHS OF TUNGSTEN MICROSPHERES

Figure 52

POWDER PROPERTIES

IDENTIFICATION: + 6-7 ORGDP NO. 4868-72

SIZE:

Particle Count, Arithmetic Mean Diameter	6.2	Microns
Arithmetic Standard Deviation	0.7	Microns
Micromerograph Mean Diameter	6.0	Microns
Weight Percent Calculated from Particle Count, Mean Diameter	6.4	Microns
Calculated from Nitrogen Surface Area	4.5	Microns
Calculated from Krypton Surface Area	5.4	Microns

SURFACE AREA:

From Nitrogen Adsorption	0.069	sq.m./g
From Krypton Adsorption	0.058	sq.m./g

TAPPED DENSITY	11.42	g./cc
CARBON CONTAMINATION	26	ppm

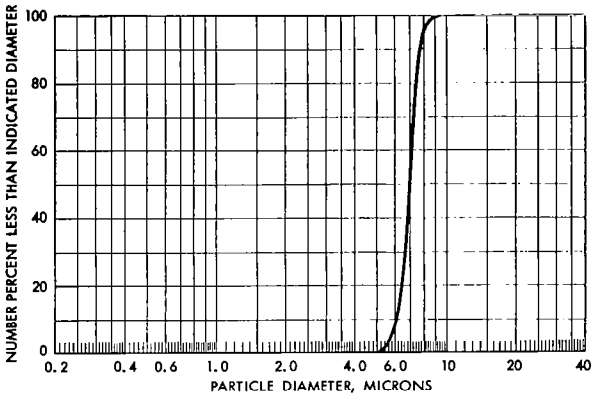

A. Cumulative Number Percent by Particle Count

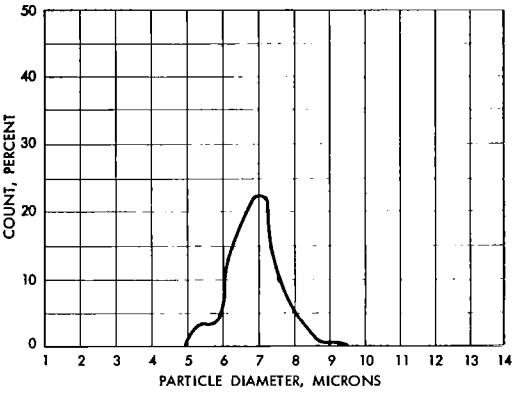

D. Frequency Plot from Particle Count

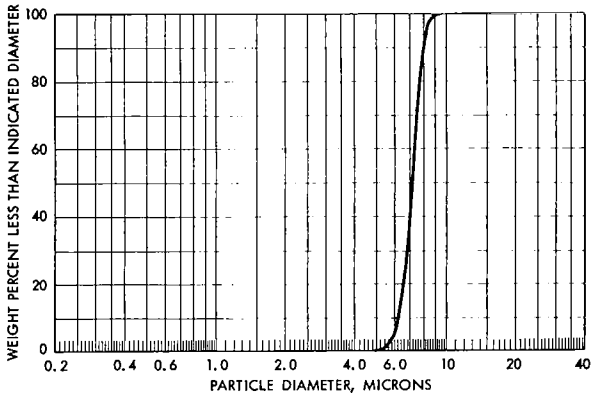

B. Cumulative Weight Percent Calculated from Particle Count

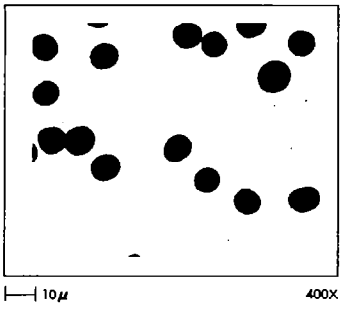

E. Shadowgraphs for Particle Counting

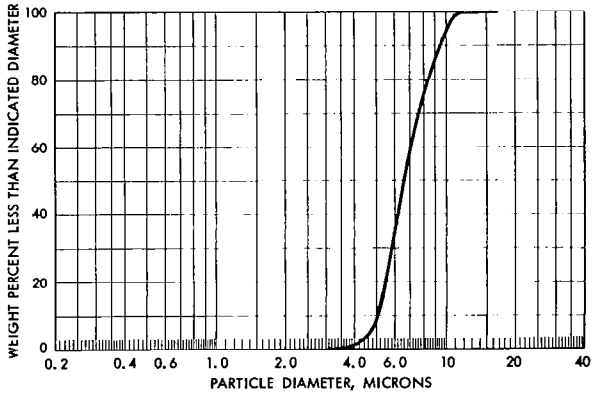

C. Cumulative Weight Percent by Micromerograph

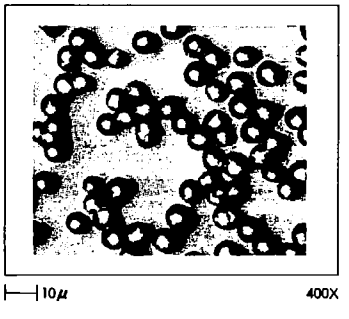

F. Highlighted Micrographs

PARTICLE SIZE DISTRIBUTIONS AND
PHOTOMICROGRAPHS OF TUNGSTEN MICROSPHERES

Figure 53

POWDER PROPERTIES

IDENTIFICATION: + 7-8 ORGDP NO. 4868-74

SIZE:

Particle Count, Arithmetic Mean Diameter	6.9	Microns
Arithmetic Standard Deviation	0.6	Microns
Micromerograph Mean Diameter	6.5	Microns
Weight Percent Calculated from Particle Count, Mean Diameter	7.3	Microns
Calculated from Nitrogen Surface Area	5.6	Microns
Calculated from Krypton Surface Area	5.9	Microns

SURFACE AREA:

From Nitrogen Adsorption	0.055	sq. m./g
From Krypton Adsorption	0.053	sq. m./g

TAPPED DENSITY	12.03	g./cc
CARBON CONTAMINATION	32	ppm

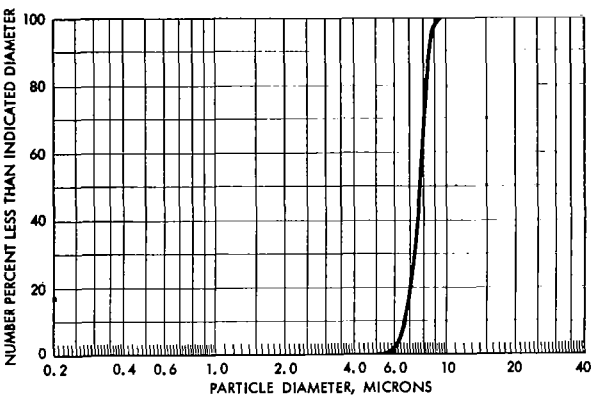

A. Cumulative Number Percent by Particle Count

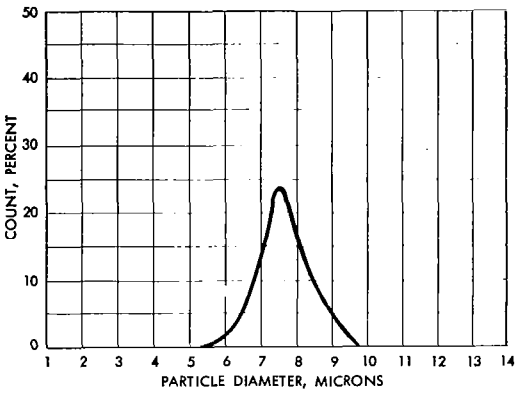

D. Frequency Plot from Particle Count

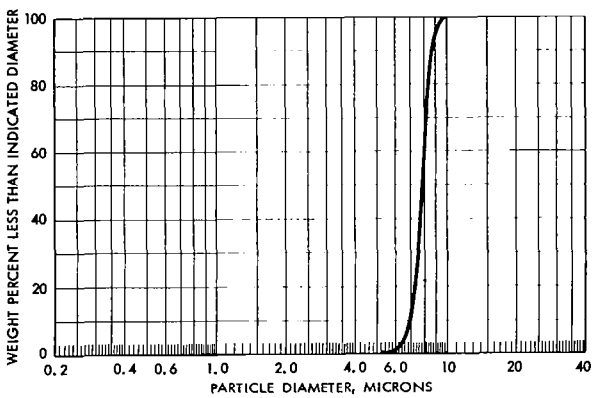

B. Cumulative Weight Percent Calculated from Particle Count

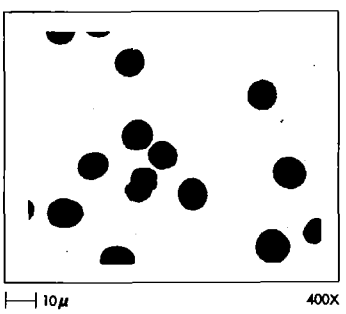

E. Shadowgraphs for Particle Counting

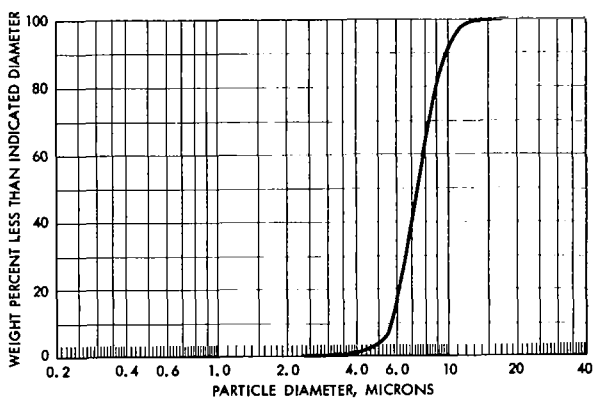

C. Cumulative Weight Percent by Micromerograph

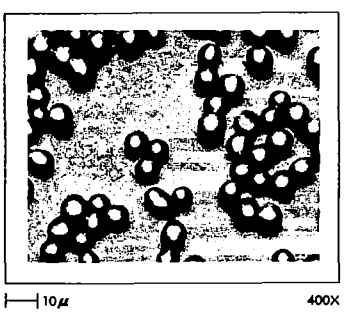

F. Highlighted Micrographs

PARTICLE SIZE DISTRIBUTIONS AND
PHOTOMICROGRAPHS OF TUNGSTEN MICROSPHERES

Figure 54

POWDER PROPERTIES

IDENTIFICATION: + 8-9 _____ ORGDP NO. 4868-76

SIZE:

Particle Count, Arithmetic Mean Diameter	7.6	Microns
Arithmetic Standard Deviation	0.7	Microns
Micromerograph Mean Diameter	7.4	Microns
Weight Percent Calculated from Particle Count, Mean Diameter	7.8	Microns
Calculated from Nitrogen Surface Area	5.6	Microns
Calculated from Krypton Surface Area	6.1	Microns

SURFACE AREA:

From Nitrogen Adsorption	0.055	sq. m./g
From Krypton Adsorption	0.051	sq. m./g

TAPPED DENSITY 11.90 g./cc

CARBON CONTAMINATION _____ ppm

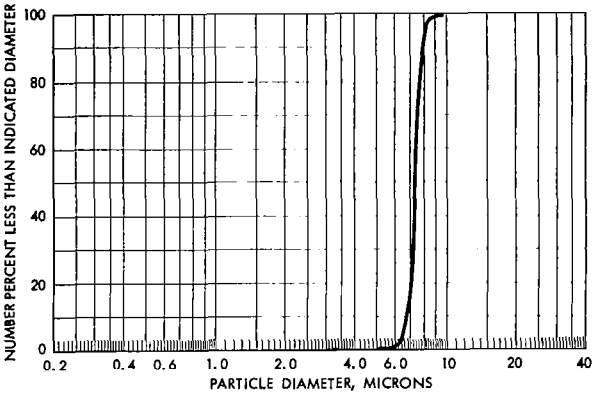

A. Cumulative Number Percent by Particle Count

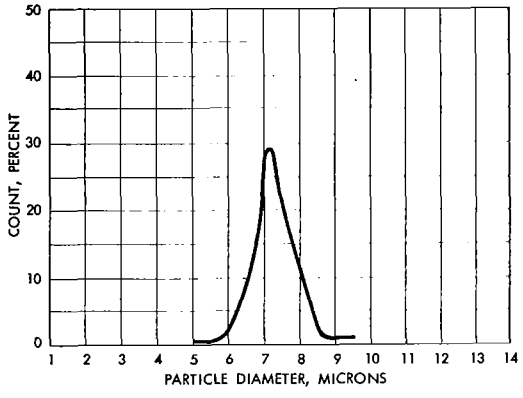

D. Frequency Plot from Particle Count

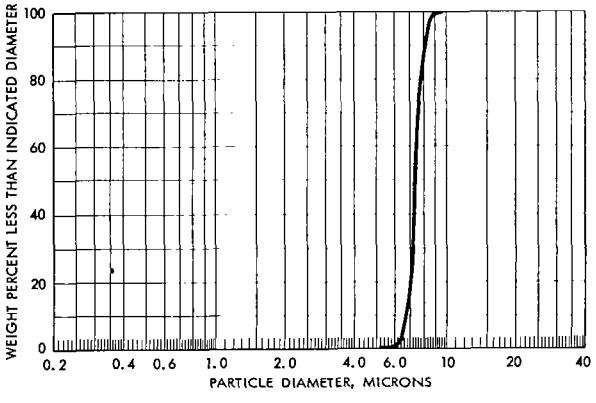

B. Cumulative Weight Percent Calculated from Particle Count

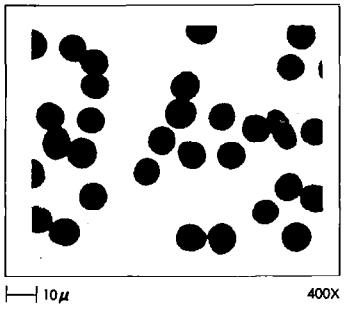

E. Shadowgraphs for Particle Counting

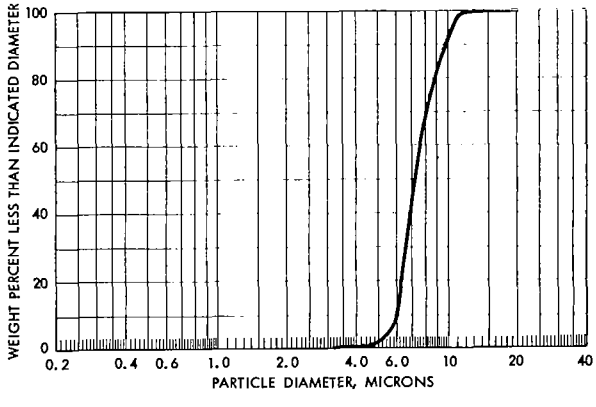

C. Cumulative Weight Percent by Micromerograph

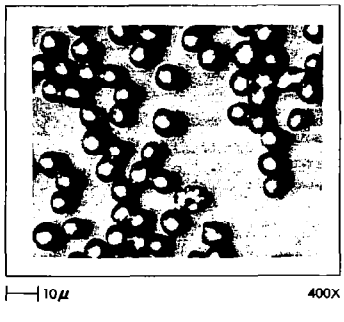

F. Highlighted Micrographs

PARTICLE SIZE DISTRIBUTIONS AND
PHOTOMICROGRAPHS OF TUNGSTEN MICROSPHERES

Figure 55

POWDER PROPERTIES

IDENTIFICATION: + 8-9, 2nd ORGDP NO. 4868-78

SIZE:

Particle Count, Arithmetic Mean Diameter	7.2	Microns
Arithmetic Standard Deviation	0.6	Microns
Micromerograph Mean Diameter	7.3	Microns
Weight Percent Calculated from Particle Count, Mean Diameter	7.3	Microns
Calculated from Nitrogen Surface Area	5.6	Microns
Calculated from Krypton Surface Area	6.2	Microns

SURFACE AREA:

From Nitrogen Adsorption	0.056	sq.m./g
From Krypton Adsorption	0.050	sq.m./g

TAPPED DENSITY	--	g./cc
CARBON CONTAMINATION		ppm

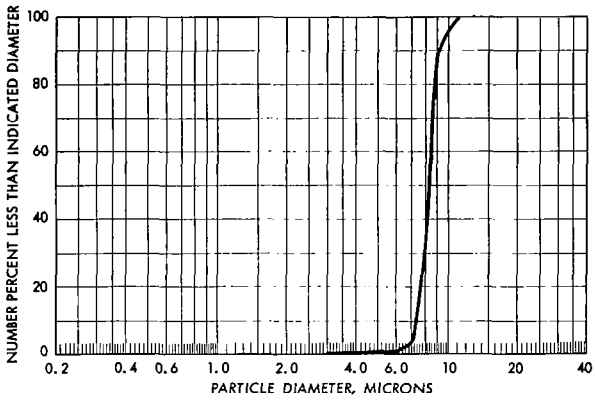

A. Cumulative Number Percent by Particle Count

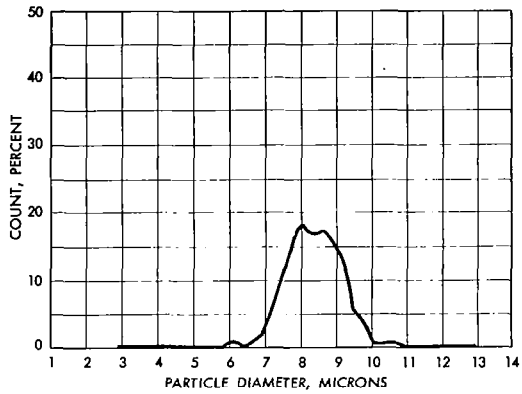

D. Frequency Plot from Particle Count

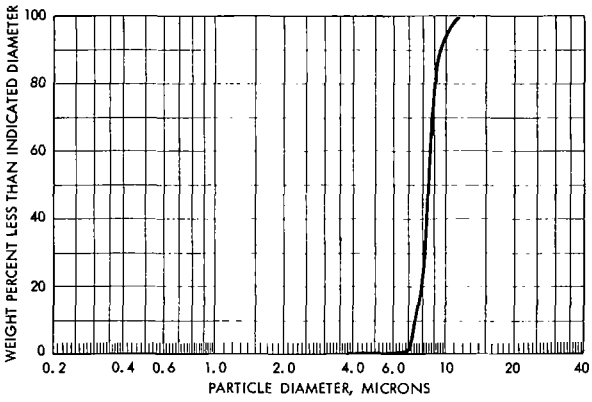

B. Cumulative Weight Percent Calculated from Particle Count

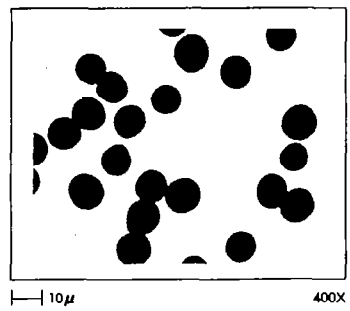

E. Shadowgraphs for Particle Counting

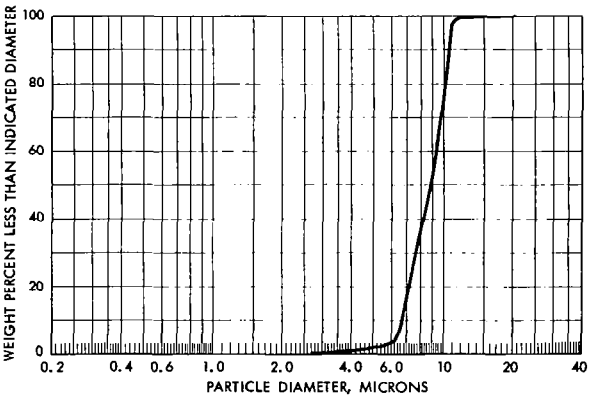

C. Cumulative Weight Percent by Micromerograph

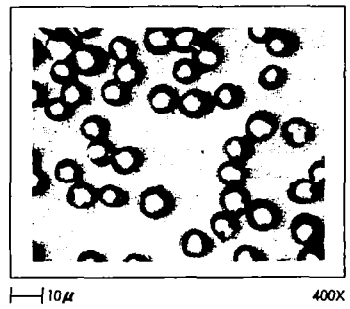

F. Highlighted Micrographs

PARTICLE SIZE DISTRIBUTIONS AND
PHOTOMICROGRAPHS OF TUNGSTEN MICROSPHERES

Figure 56

POWDER PROPERTIES

IDENTIFICATION: + 9-11 ORGDP NO. 4868-80

SIZE:

Particle Count, Arithmetic Mean Diameter	8.4	Microns
Arithmetic Standard Deviation	0.9	Microns
Micromerograph Mean Diameter	8.9	Microns
Weight Percent Calculated from Particle Count, Mean Diameter	8.5	Microns
Calculated from Nitrogen Surface Area	6.5	Microns
Calculated from Krypton Surface Area	9.1	Microns

SURFACE AREA:

From Nitrogen Adsorption	0.048	sq. m./g
From Krypton Adsorption	0.034	sq. m./g

TAPPED DENSITY	11.30	g./cc
CARBON CONTAMINATION	32	ppm

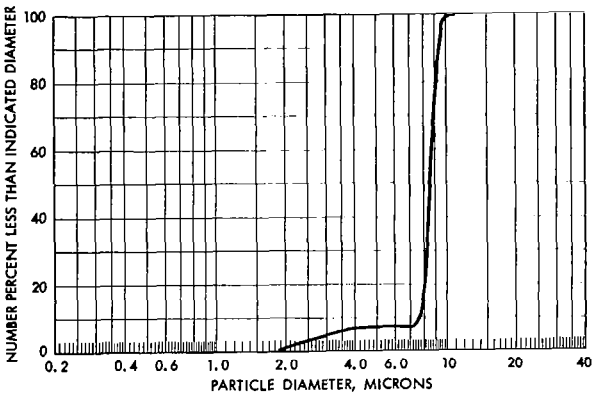

A. Cumulative Number Percent by Particle Count

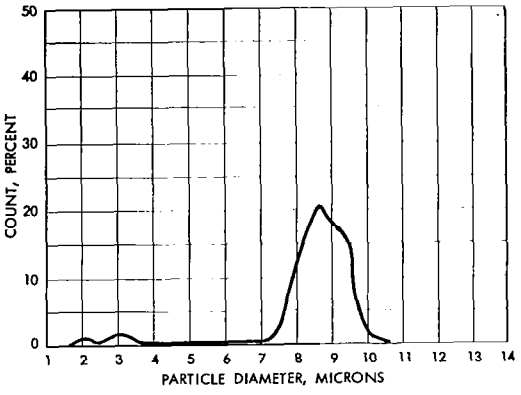

D. Frequency Plot from Particle Count

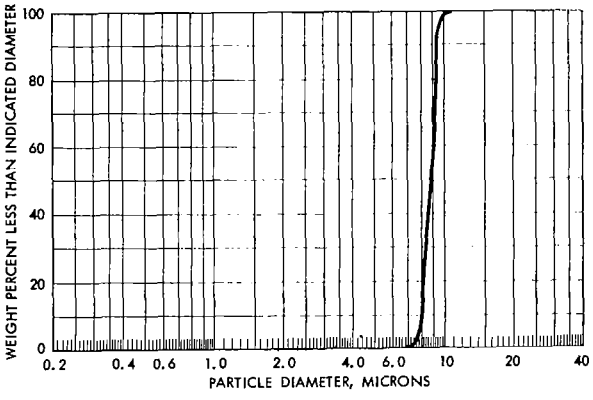

B. Cumulative Weight Percent Calculated from Particle Count

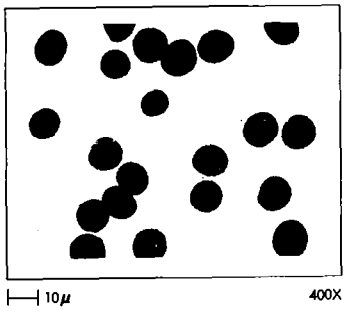

E. Shadowgraphs for Particle Counting

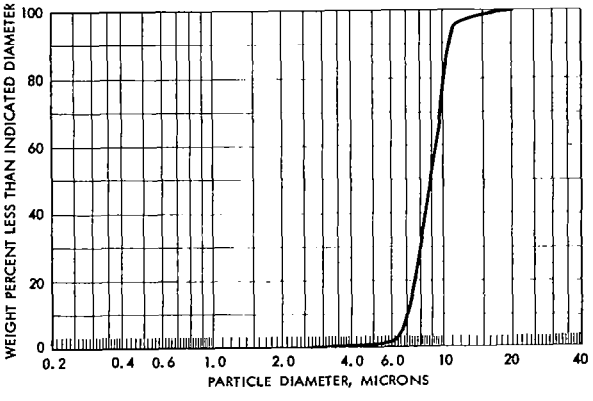

C. Cumulative Weight Percent by Micromerograph

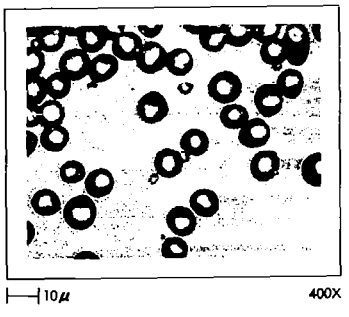

F. Highlighted Micrographs

PARTICLE SIZE DISTRIBUTIONS AND
PHOTOMICROGRAPHS OF TUNGSTEN MICROSPHERES

Figure 57

POWDER PROPERTIES

IDENTIFICATION: + 9-11, 2nd ORGDP NO. 4868-82

SIZE:

Particle Count, Arithmetic Mean Diameter	8.4	Microns
Arithmetic Standard Deviation	1.6	Microns
Micromerograph Mean Diameter	9.0	Microns
Weight Percent Calculated from Particle Count, Mean Diameter	8.8	Microns
Calculated from Nitrogen Surface Area	6.4	Microns
Calculated from Krypton Surface Area	6.8	Microns

SURFACE AREA:

From Nitrogen Adsorption	0.049	sq. m./g
From Krypton Adsorption	0.046	sq. m./g

TAPPED DENSITY -- g./cc

CARBON CONTAMINATION _____ ppm

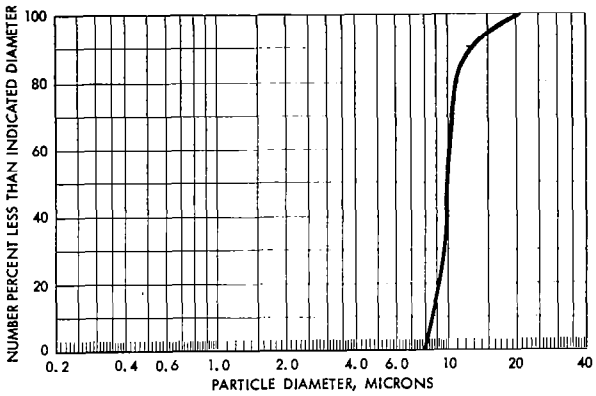

A. Cumulative Number Percent by Particle Count

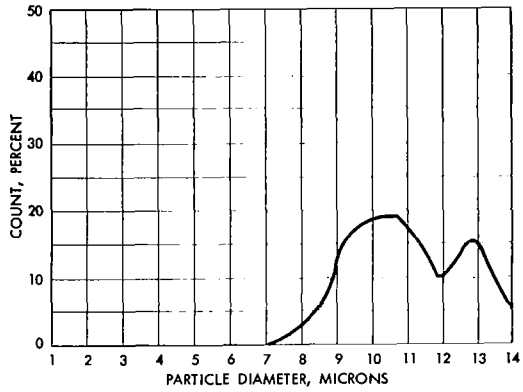

D. Frequency Plot from Particle Count

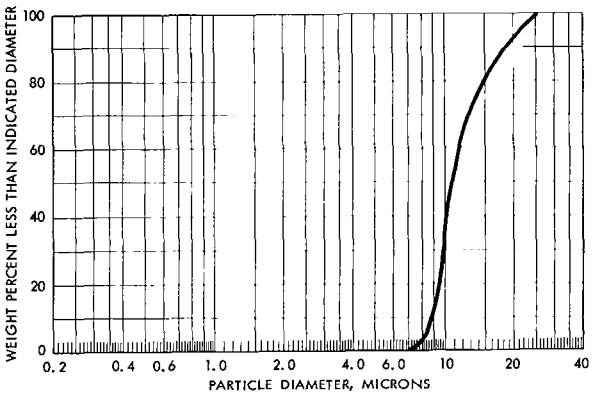

B. Cumulative Weight Percent Calculated from Particle Count

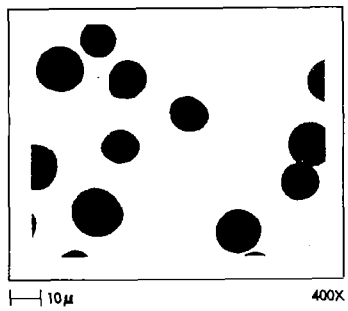

E. Shadowgraphs for Particle Counting

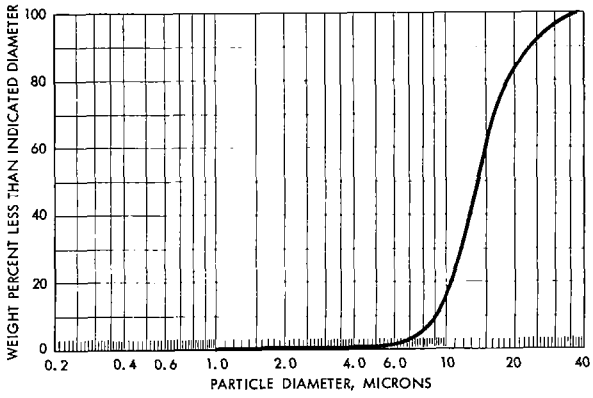

C. Cumulative Weight Percent by Micromerograph

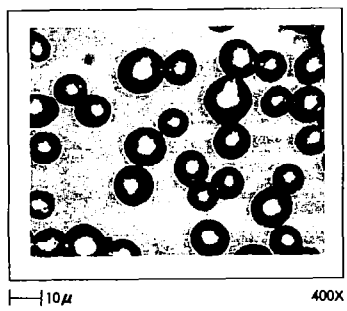

F. Highlighted Micrographs

PARTICLE SIZE DISTRIBUTIONS AND
PHOTOMICROGRAPHS OF TUNGSTEN MICROSPHERES

Figure 58

POWDER PROPERTIES

IDENTIFICATION: + 11-30 ORGDP NO. 4868-84

SIZE:

Particle Count, Arithmetic Mean Diameter	10.9	Microns
Arithmetic Standard Deviation	2.4	Microns
Micromerograph Mean Diameter	13.5	Microns
Weight Percent Calculated from Particle Count, Mean Diameter	12.0	Microns
Calculated from Nitrogen Surface Area	10.7	Microns
Calculated from Krypton Surface Area	9.4	Microns

SURFACE AREA:

From Nitrogen Adsorption	0.029	sq.m./g
From Krypton Adsorption	0.033	sq.m./g

TAPPED DENSITY	12.06	g./cc
CARBON CONTAMINATION	28	ppm

ORGDP NO. 4868-14

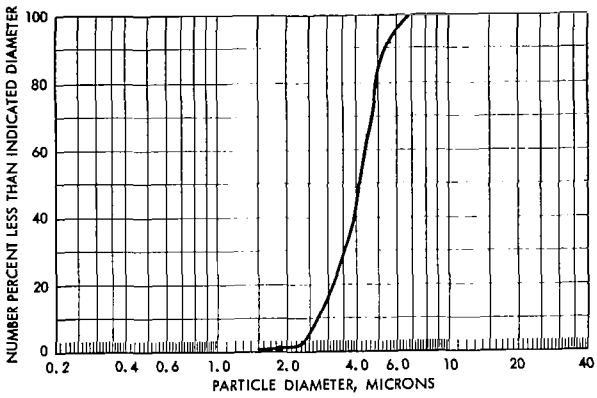

A. Cumulative Number Percent by Particle Count

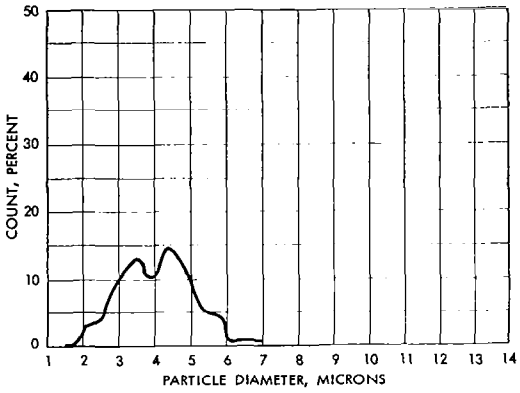

D. Frequency Plot from Particle Count

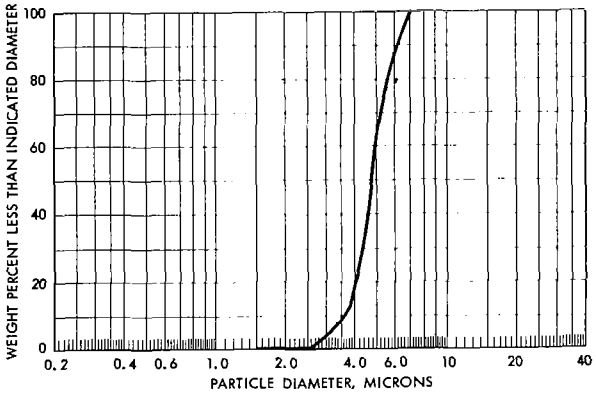

B. Cumulative Weight Percent Calculated from Particle Count

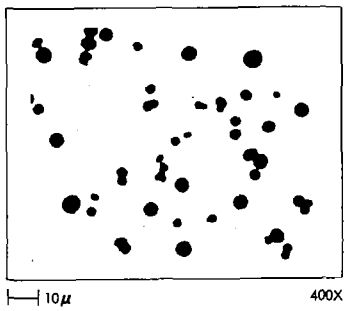

E. Shadowgraphs for Particle Counting

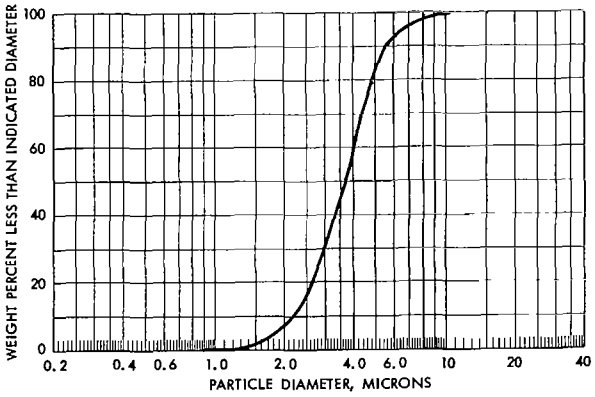

C. Cumulative Weight Percent by Micromerograph

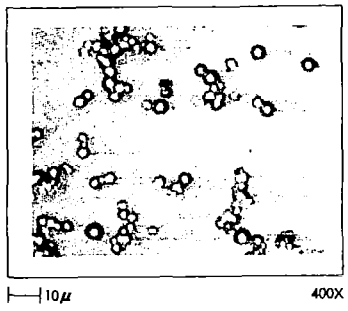

F. Highlighted Micrographs

PARTICLE SIZE DISTRIBUTIONS AND
PHOTOMICROGRAPHS OF TUNGSTEN MICROSPHERES

Figure 59

POWDER PROPERTIES

IDENTIFICATION: Linde Precut, 4A, Coarse ORGDP NO. 4868-14

SIZE:

Particle Count, Arithmetic Mean Diameter	4.1	Microns
Arithmetic Standard Deviation	1.0	Microns
Micromerograph Mean Diameter	3.8	Microns
Weight Percent Calculated from Particle Count, Mean Diameter	4.8	Microns
Calculated from Nitrogen Surface Area	2.3	Microns
Calculated from Krypton Surface Area	2.3	Microns

SURFACE AREA:

From Nitrogen Adsorption	0.136	sq.m./g
From Krypton Adsorption	0.138	sq.m./g

TAPPED DENSITY	10.1	g./cc
CARBON CONTAMINATION	--	ppm

ORGDP NO. 4868-16

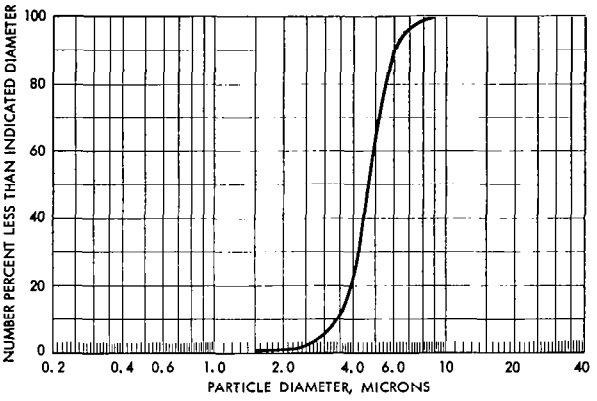

A. Cumulative Number Percent by Particle Count

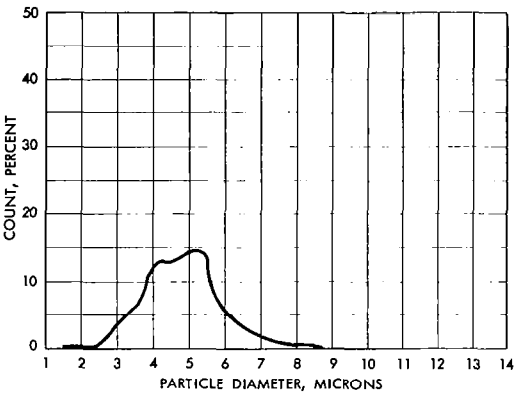

D. Frequency Plot from Particle Count

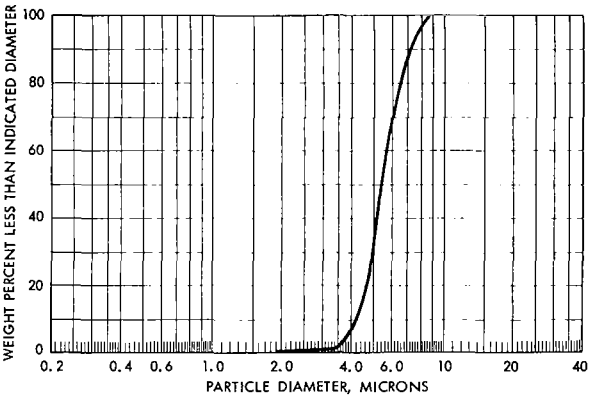

B. Cumulative Weight Percent Calculated from Particle Count

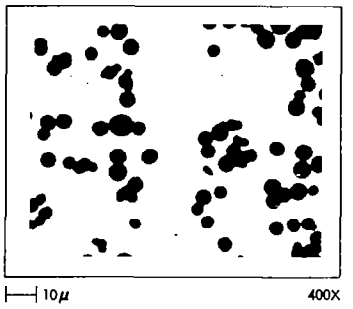

E. Shadowgraphs for Particle Counting

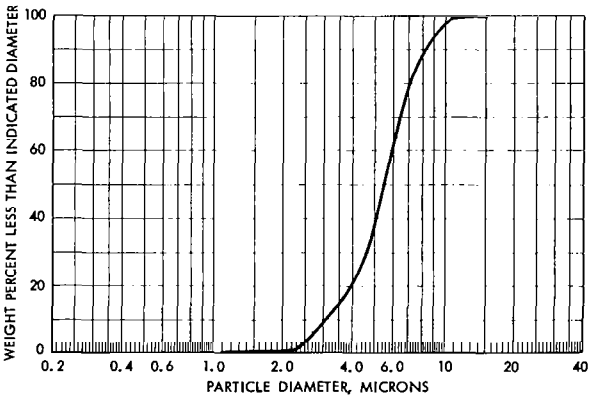

C. Cumulative Weight Per cent by Micromerograph

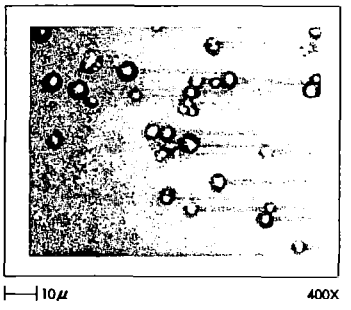

F. Highlighted Micrographs

PARTICLE SIZE DISTRIBUTIONS AND
PHOTOMICROGRAPHS OF TUNGSTEN MICROSPHERES

Figure 60

POWDER PROPERTIES

IDENTIFICATION: Linde Precut, 3B, Coarse ORGDP NO. 4868-16

SIZE:		
Particle Count, Arithmetic Mean Diameter	4.8	Microns
Arithmetic Standard Deviation	1.1	Microns
Micromerograph Mean Diameter	4.4	Microns
Weight Percent Calculated from Particle Count, Mean Diameter	5.4	Microns
Calculated from Nitrogen Surface Area	3.0	Microns
Calculated from Krypton Surface Area	2.5	Microns
SURFACE AREA:		
From Nitrogen Adsorption	0.102	sq.m./g
From Krypton Adsorption	0.126	sq.m./g
TAPPED DENSITY	10.3	g./cc
CARBON CONTAMINATION	--	ppm

ORGDP NO. 4868-18

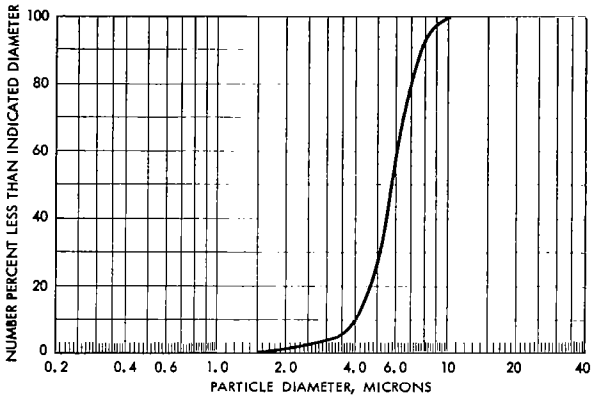

A. Cumulative Number Percent by Particle Count

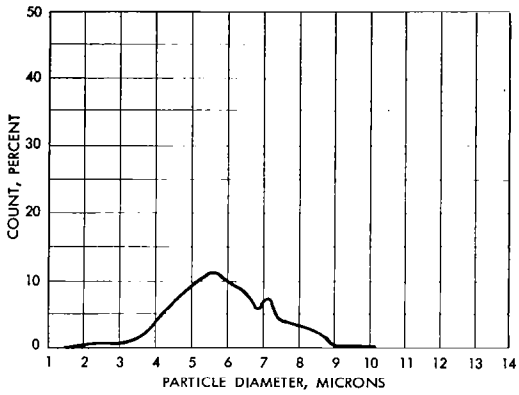

D. Frequency Plot from Particle Count

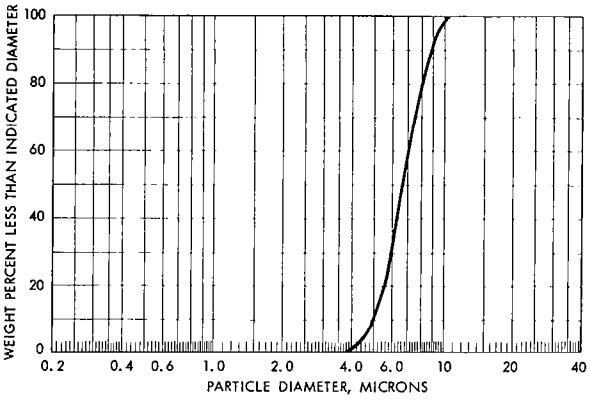

B. Cumulative Weight Percent Calculated from Particle Count

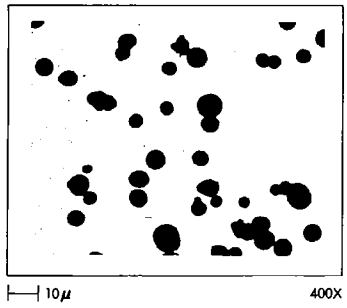

E. Shadowgraphs for Particle Counting

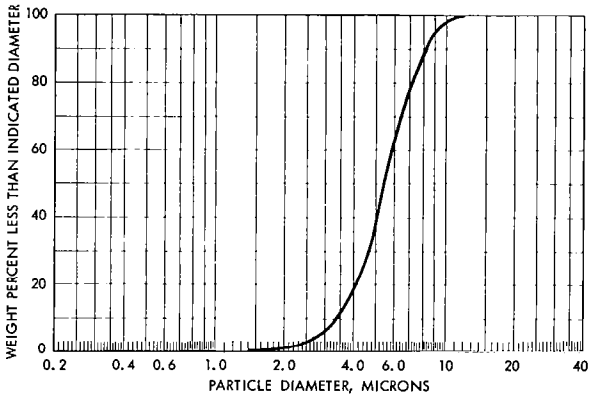

C. Cumulative Weight Percent by Micromerograph

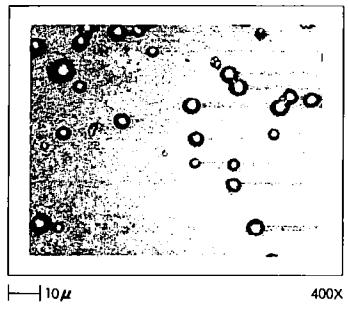

F. Highlighted Micrographs

PARTICLE SIZE DISTRIBUTIONS AND
PHOTOMICROGRAPHS OF TUNGSTEN MICROSPHERES

Figure 61

POWDER PROPERTIES

IDENTIFICATION: Linde Precut, 2B, Coarse ORGDP NO. 4868-18

SIZE:		
Particle Count, Arithmetic Mean Diameter	5.8	Microns
Arithmetic Standard Deviation	1.5	Microns
Micromerograph Mean Diameter	5.3	Microns
Weight Percent Calculated from Particle Count, Mean Diameter	7.1	Microns
Calculated from Nitrogen Surface Area	3.3	Microns
Calculated from Krypton Surface Area	3.9	Microns
SURFACE AREA:		
From Nitrogen Adsorption	0.093	sq. m./g
From Krypton Adsorption	0.079	sq. m./g
TAPPED DENSITY	10.5	g./cc
CARBON CONTAMINATION	--	ppm

TABLE XXXX

PARTICLE SIZE AND SURFACE AREA SUMMARY FOR SPHERICAL TUNGSTEN POWDERS

Powder Number	Description	Particle Size Data						Surface Area, sq.m./g.		
		Particle Count, Diameter, microns	Standard Deviation, microns	Weight from Count Diameter, microns	Micromerograph Diameter, microns	Nitrogen Surface Area Diameter, microns	Krypton Surface Area Diameter, microns	Nitrogen Adsorption	Krypton Adsorption	Calculated from Particle Count
4868-38	Original* Material	4.2	1.9	6.5	5.2	3.2	2.9	0.098	0.106	0.0525
4868-52	- 2.8	2.6	0.7	3.0	1.8	0.9	1.0	0.334	0.316	0.1075
4868-54	2-3, 3rd	1.9	0.5	2.3	2.2	1.2	1.3	0.253	0.241	0.1432
4868-56	+ 2.5-3	2.1	0.6	2.6	2.3	1.4	1.3	0.225	0.238	0.1267
4868-58	+ 2.5-3, 1st	2.2	0.6	2.6	2.4	1.3	1.4	0.240	0.217	0.1264
4868-60	+ 3-4, 2nd	2.6	0.5	3.1	2.9	1.8	2.2	0.169	0.140	0.1093
4868-62	+ 3-4	3.5	0.6	3.7	3.3	2.2	2.8	0.139	0.110	0.0856
4868-64	+ 4-5, 2nd	3.0	0.6	3.3	3.0	2.3	2.4	0.135	0.130	0.0958
4868-66	+ 4-5	4.2	0.6	4.2	4.1	3.1	3.3	0.101	0.093	0.0707
4868-68	+ 5-6	5.1	0.6	5.2	4.7	4.0	4.0	0.078	0.077	0.0589
4868-70	+ 5-6, 2nd	5.1	0.5	5.2	4.3	3.8	4.8	0.081	0.065	0.0596
4868-72	+ 6-7	6.2	0.7	6.4	6.0	4.5	5.4	0.069	0.058	0.0486
4868-74	+ 7-8	6.9	0.7	7.3	6.5	5.6	5.9	0.055	0.053	0.0441
4868-76	+ 8-9	7.6	0.7	7.8	7.4	5.6	6.1	0.055	0.051	0.0399
4868-78	+ 8-9, 2nd	7.2	0.6	7.3	7.3	5.6	6.2	0.056	0.050	0.0421
4868-80	+ 9-11	8.4	0.9	8.5	8.9	6.5	9.1	0.048	0.034	0.0364
4868-82	+ 9-11, 2nd	8.4	1.6	8.8	9.0	6.4	6.8	0.049	0.046	0.0354
4868-84	+11-30	10.9	2.4	12.0	13.5	10.7	9.4	0.029	0.033	0.0255
4868-14	Linde Pre-Cut** 4A Coarse	4.1	1.0	4.8	3.8	2.3	2.3	0.136	0.138	0.0676
4868-16	Linde Pre-Cut** 3B Coarse	4.8	1.1	5.4	4.8	3.0	2.5	0.102	0.126	0.0581
4868-18	Linde Pre-Cut** 2B Coarse	5.8	1.5	7.1	5.5	3.3	3.9	0.093	0.079	0.0475

*Linde Microspheres, 40 lb., Lot 2044-27.

**Purchased as classified fractions, Linde Microspheres, Lot 2044-6.

TABLE XXXXI

COMPARATIVE CARBON ANALYSIS OF SPHERICAL TUNGSTEN POWDER BEFORE AND AFTER CLASSIFICATION

	Sample 4868-38 As Received	Sample 4868-66 Classified
Carbon, ppm.	42	220

TABLE XXXXII

COMPARATIVE SPECTROCHEMICAL ANALYSIS OF SPHERICAL TUNGSTEN POWDER BEFORE AND AFTER CLASSIFICATION

Element	Concentration, ppm. Sample 4868-38	Sample 4868-66	Element	Concentration, ppm. Sample 4868-38	Sample 4868-66	Element	Concen Sample 4868
Li	---	< 1	Hf	< 1	< 1	Er	< 1
Na		< 5	Th	---		Eu	< 1
K	5	1	Sb	---	< 1	Ho	< 1
Rb	< 5	< 5	Bi	---	< 1	Gd	< 1
Cu	7	10	V	---	< 1	Ce	< 1
Ag	---	< 1	Ta	< 1	< 1	Nd	< 1
Ca	15	20	Cr	15	10	Dy	< 1
Sr	---	< 1	Mo	20	3	Tm	< 1
Ba	---	< 1	Mn	---	< 1	Sm	< 1
Be	---	< 0.1	Fe	17	20	Yb	< 1
Mg	11	15	Co	---	10	Lu	< 1
Zn	---	< 15	Ni	4	8	La	< 1
B	---	< 1	Rh	< 1	< 1	Tb	< 1
Al	9	7	Pd	< 1	< 1	Pr	< 1
Si	3	15	Ta	< 1	< 1		
Sn	---	< 1	Pt	< 1	4		
Ru	---	< 1	Cb	< 1	< 1		
Ti	---	< 1	Ga	< 1	< 1		
Zr	< 1	< 1					

--- Means "sought but not found."

4868-38 - As received Linde spherical tungsten, Lot 2044-27.

4868-66 - Classified by Vortec. Cut point 4 to 5 microns.

DWG. NO. G-66-613

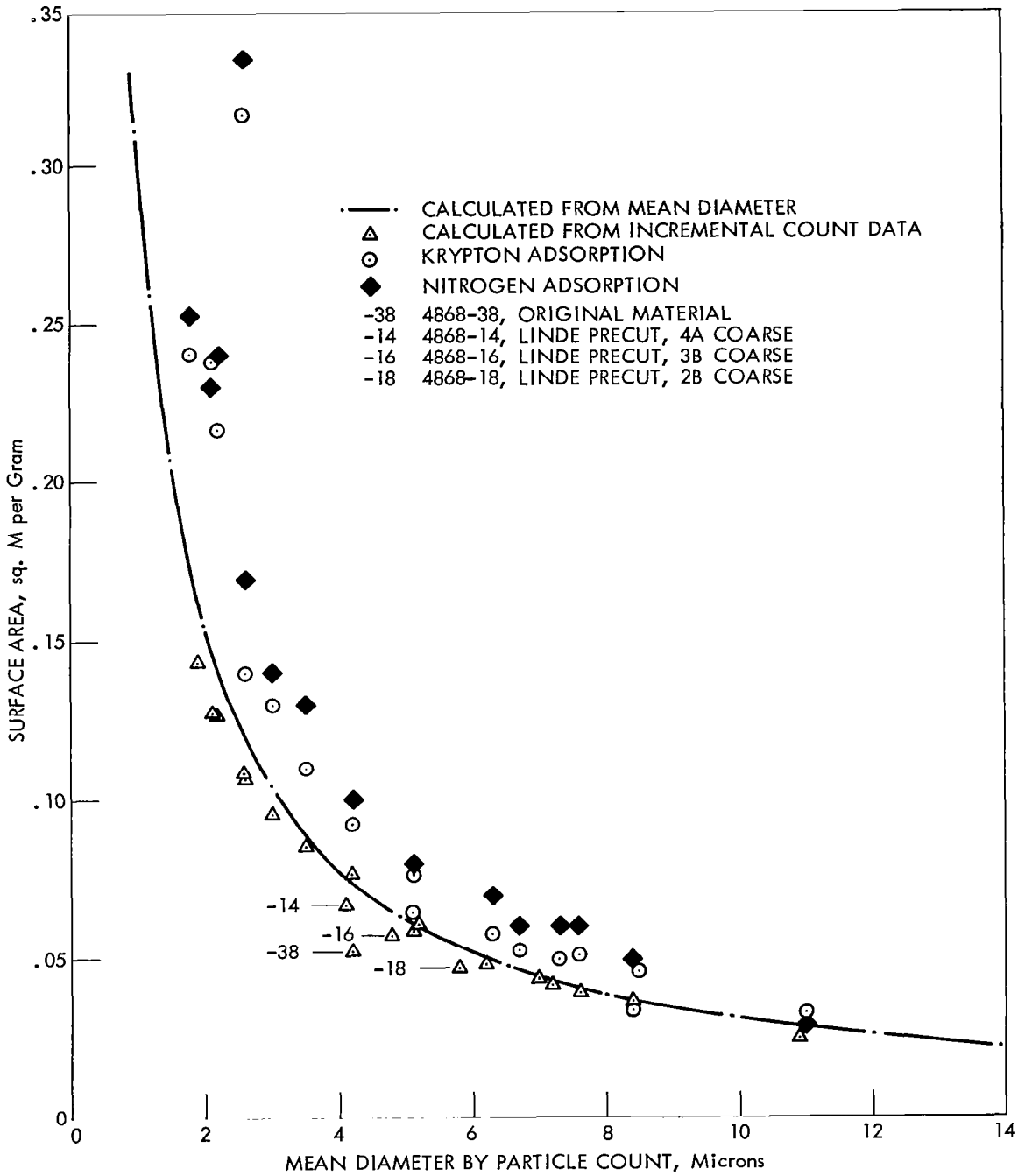

COMPARISON BETWEEN EXPERIMENTAL AND CALCULATED SURFACE AREAS FOR TUNGSTEN MICROSPHERES

Figure 62

from the mean diameter is shown. Obvious features of this comparison are as follows:

1. The surface area calculated from incremental count data agrees well with that calculated from the mean diameter, especially above 3 microns diameter for the sharp cuts.

2. The poorer the cut, the poorer the agreement between calculated and experimental values of surface area.

3. As the particle size increases, agreement between all of the types of surface area becomes better and is excellent at 10.5 microns.

The reason for the discrepancy between the experimental and calculated values is not known; however, there are several possibilities:

1. Particle count does not reveal very fine particles which contribute to high surface area. This is partially supported by the Micromerograph results.

2. Surface roughness or surface oxide gives a higher value of experimental surface area than would be calculated from the smooth sphere model.

The very high value of surface area for one of the 3-micron powders cannot be explained at this time.

Figure 63 compares the mean diameters calculated from surface area with the Micromerograph and particle count diameters. The line of equivalence serves as a reference. The most notable feature of this graph is the surprisingly good agreement between the mean diameter by Micromerograph and by particle count.

In summary it appears that the classification process does not introduce unacceptable impurities into the powders and that the classification is very efficient. The standard deviations achieved, especially in the 2- to 5-micron range are indicative of very closely sized spheres which should produce ionizers of high quality. Thus, there is available from this classification sufficient materials to produce ionizers having a wide range of pore size and pore density.

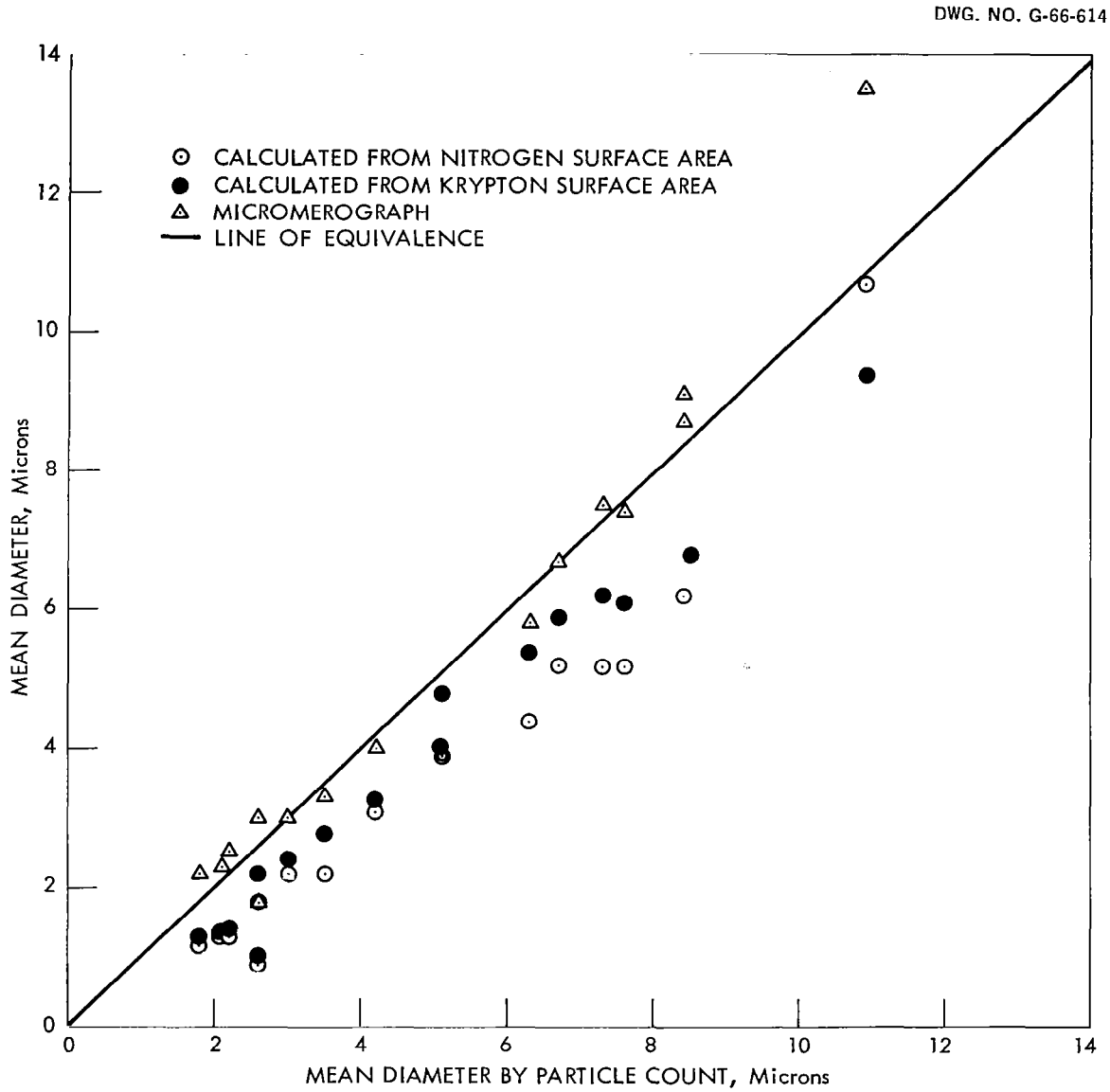

COMPARISON OF MEAN DIAMETERS FROM SURFACE AREA, MICROMEROGRAPH AND PARTICLE COUNT

Figure 63

APPENDIX IV

PERMEABILITY SCANNING

Prepared by J. A. Cochran

Standard flow tests measure the average flow properties of porous materials. They give little or no information about the variation of permeability throughout the sample. Photomicrographs and mercury intrusion data are helpful in estimating the uniformity. However, it is extremely difficult to translate these types of data to actual flow performance. Therefore, effort has been directed at the development of a permeability scanning test capable of detecting small permeability variations. Such a device would be a powerful tool in evaluating the effectiveness of methods aimed at improving the flow uniformity of porous ionizers.

The bubble test, described elsewhere, has been used successfully to obtain a gross estimate of permeability variations. Several methods were considered for more precise and quantitative measurements; of these the thermistor probe was selected as the most promising approach. It has two very important characteristics; the gas velocity from the surface pores is sensed directly, and great sensitivity can be obtained with thermistor devices.

The following paragraphs describe the results of work on the thermistor bridge permeability scanning technique. Although not perfected at this time, the method shows considerable promise and is being developed further. Current effort and future plans are discussed briefly at the end of this section.

The experiments performed during this contract period were primarily a scoping study to delineate the problems involved in the technique. Most of the work was concerned with probe-to-sample relationships and instrumental control. Thermistor probe design, although considered generally, has been deferred for future study. Discussion of the results is divided into three sections, each involving separate experiments and equipment.

1. Scanner Assembly Model 1 was used to examine several possible approaches to the general problem and to determine some of the specific difficulties.

2. A Thermistor Calibrator was made so that the relationship between thermistor bridge output and test gas velocity could be evaluated independently of the scanner assembly or the test sample characteristics.

3. Scanner Assembly Model 2 was used to evaluate some of the temperature and control problems encountered in the first model, and to provide design criteria for future work.

Scanner Assembly Model 1. A photograph of the scanner is shown in figure 64. This equipment consists of a thermistor probe located in a fixed horizontal position with vertical micrometer adjustment, a motor-driven sample mount to move the sample in the horizontal plane past the thermistor probe, and the necessary recording and control equipment. A plastic enclosure was mounted over the assembly to isolate the sample from the atmosphere. Figure 65 shows the thermistor probe positioned over an ionizer assembly. A reference thermistor shown to the left of the sample mount was used with the probe thermistor in a bridge circuit to obtain compensation for variations in ambient temperature.

Although the experimental variables were to be evaluated with this equipment, uncontrolled thermal variations seriously limited the maximum usable output sensitivity. In spite of this limitation, however, valuable experience was obtained with this scanner.

Helium and air were used as test gases. Tests were also made with mixtures of helium and air not only as the test gas, but as an atmosphere on the probe side of the sample. The high sensitivity of the probe to gas concentration and the difficulty of maintaining constant concentrations made this approach unsatisfactory. Even though the greater thermal conductivity of helium results in greater sensitivity, concentration measurements indicated that it would be difficult to prevent diffusion of air into the test chamber. Based on these findings the work was confined to the use of air as the test gas.

PHOTO

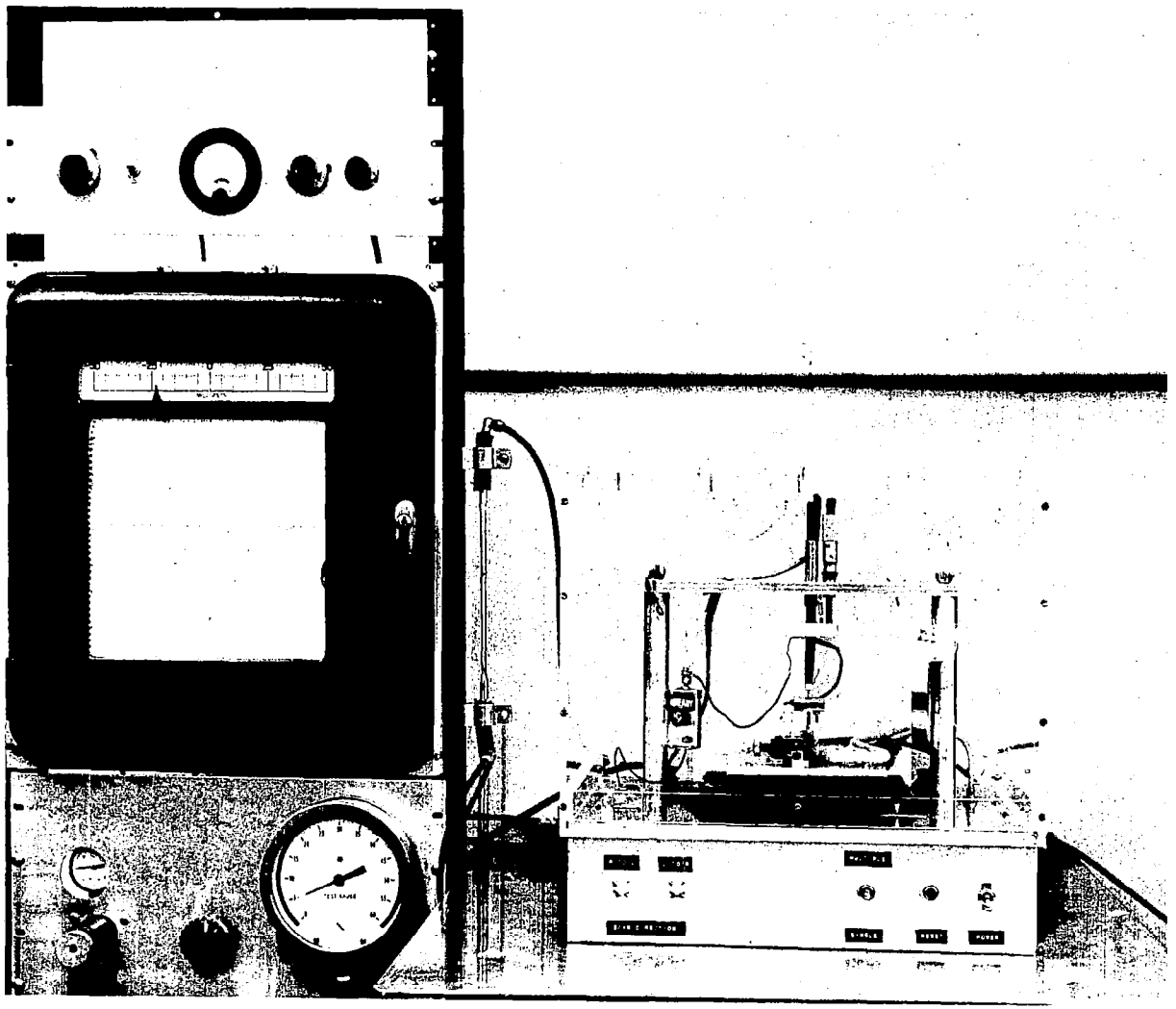

SCANNER ASSEMBLY MODEL 1

Figure 64

PHOTO NO. PH-65-754

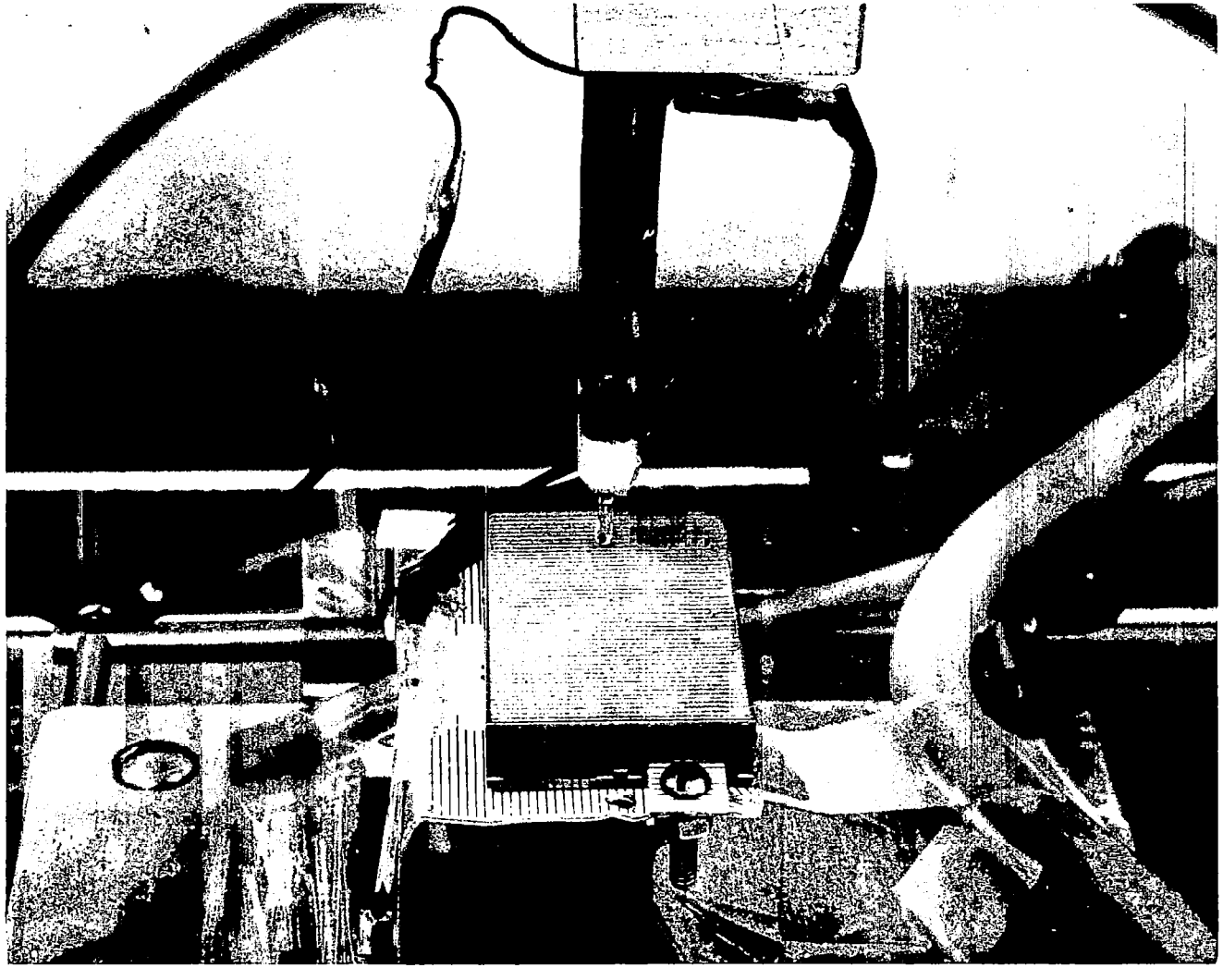

THERMISTOR PROBE SHOWN IN POSITION
ABOVE TUNGSTEN IONIZER

Figure 65

SECRET

Several ionizer assemblies were scanned and in some cases there could be little doubt that changes in gas velocity were being recorded. However, since it was necessary to operate with reduced sensitivity little signal above background was obtained with air as the test gas. Figure 66 illustrates typical performance of the scanner. These curves were obtained by repeatedly scanning the same path across a flat porous sample. Curve B shows the output trace obtained with no flow through the sample. When the other curves are compared with the zero flow curve it appears that the output could be a function of sample topology as well as sample permeability. The effects of changing thermistor current and test gas are clearly evident. That the sample topology is a factor is illustrated in figure 67. Here a recorder trace is compared to a mechanical measurement of the gross variation of the sample surface. Clearly the recorder trace appears to be a function of the probe-to-sample distance. Two recorder traces are shown. The mirror image effect is due to different directions of thermistor probe travel. Note the reproducibility of the trace form and the apparent slow drift with time. The discontinuities at the ends of the trace are probably due to the proximity of the metallic sample mount.

From data such as these and from data obtained from the Thermistor Calibrator, discussed below, it was concluded that better control of the thermal gradients was necessary before the thermistor scanning technique could be evaluated.

Thermistor Calibrator. A device was assembled to evaluate the characteristics of the thermistors used in the scanner assemblies. Figure 68 shows a sectional view of the calibrator. The two thermistors are mounted in separate glass tubes. A heat exchanger, a flow meter, and a flow controlling device are provided for each tube. The inside diameter of each tube was carefully measured so that the cross-sectional area could be used with the volumetric flow to calculate the velocity of the test gas past the thermistors. A constant temperature stream of water was pumped through the water jacket to maintain the desired temperature level.

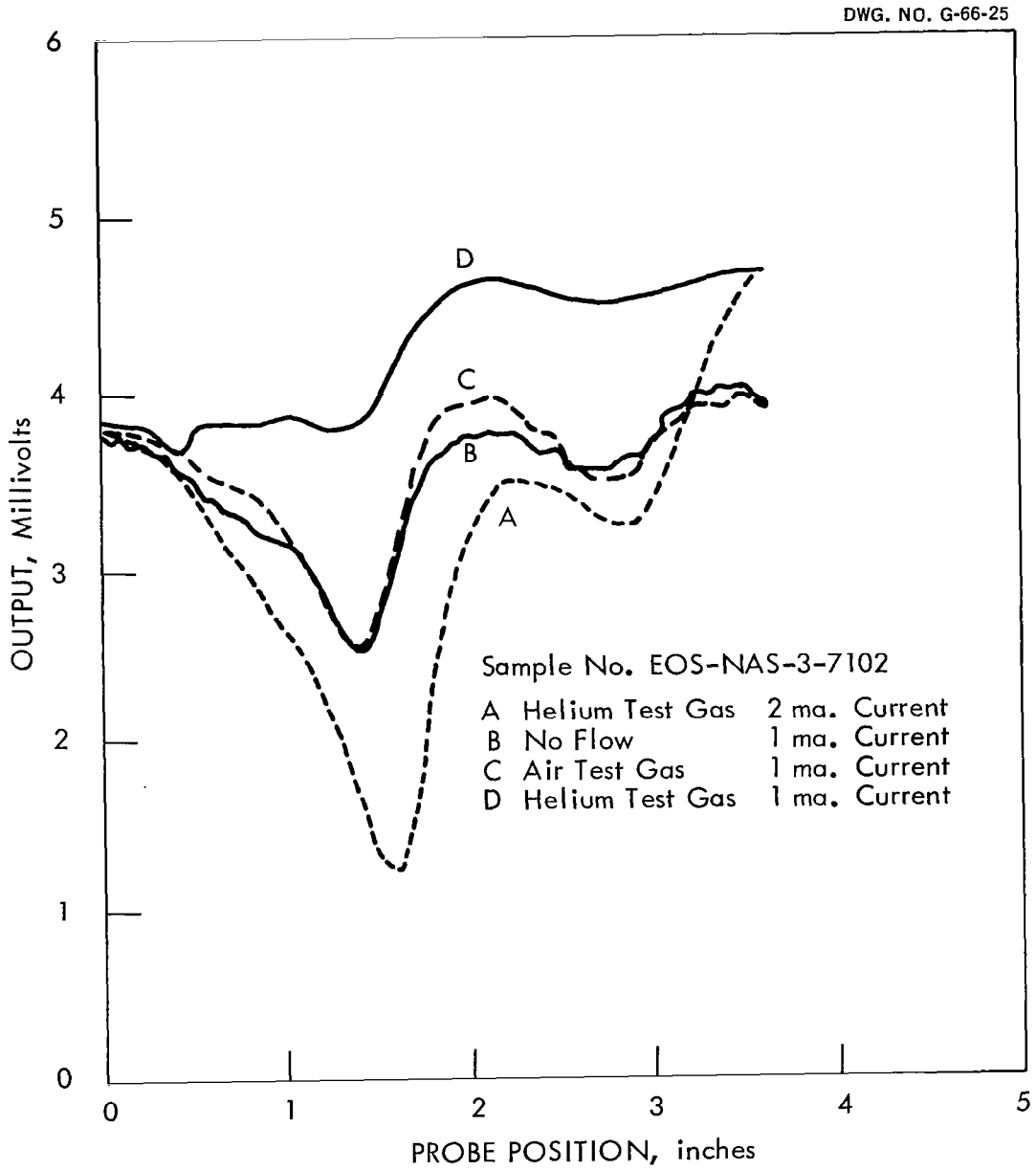

THERMISTOR BRIDGE SCANNER OUTPUT TRACES

Figure 66

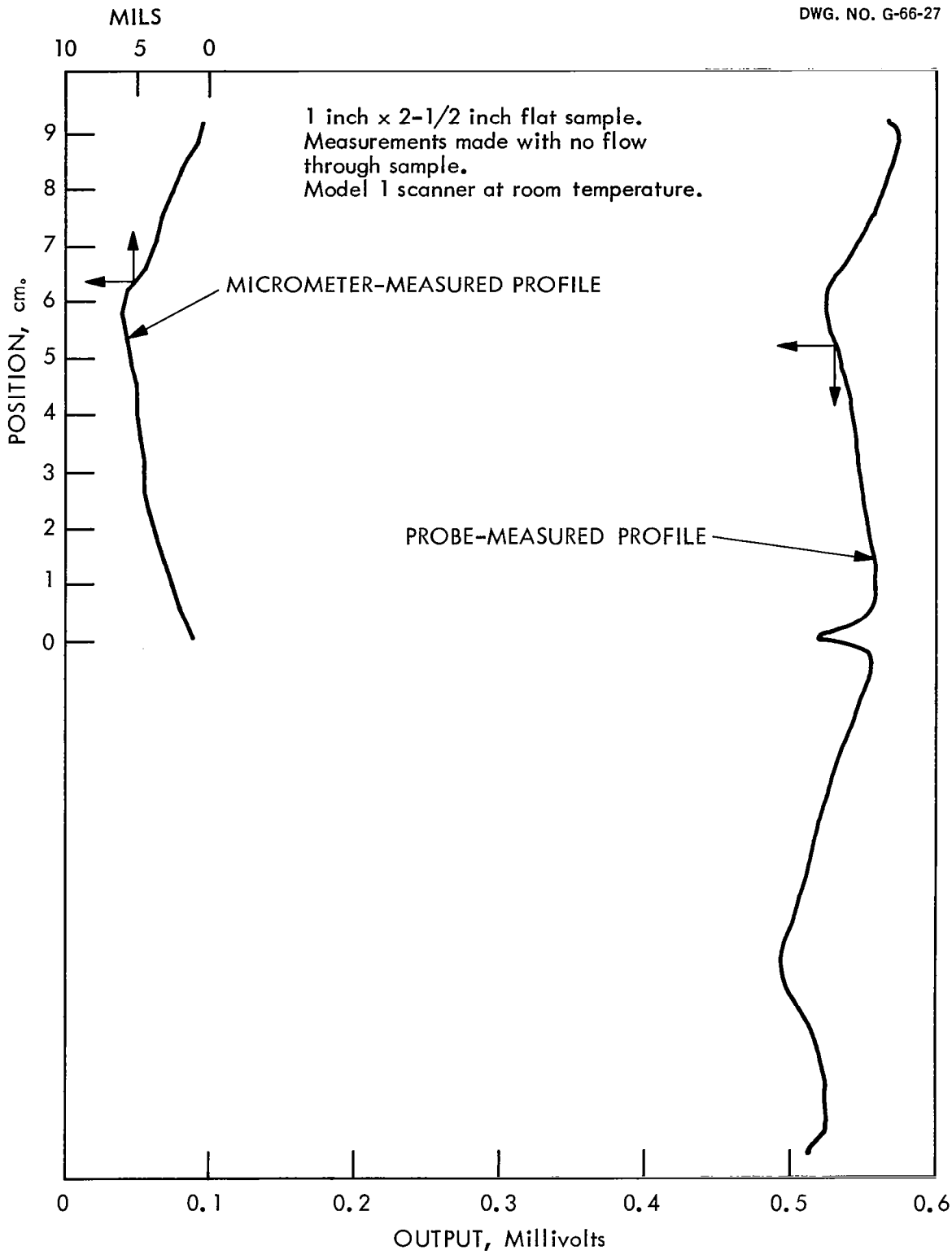

SAMPLE SURFACE PROFILE

Figure 67

DWG. NO. G-66-28

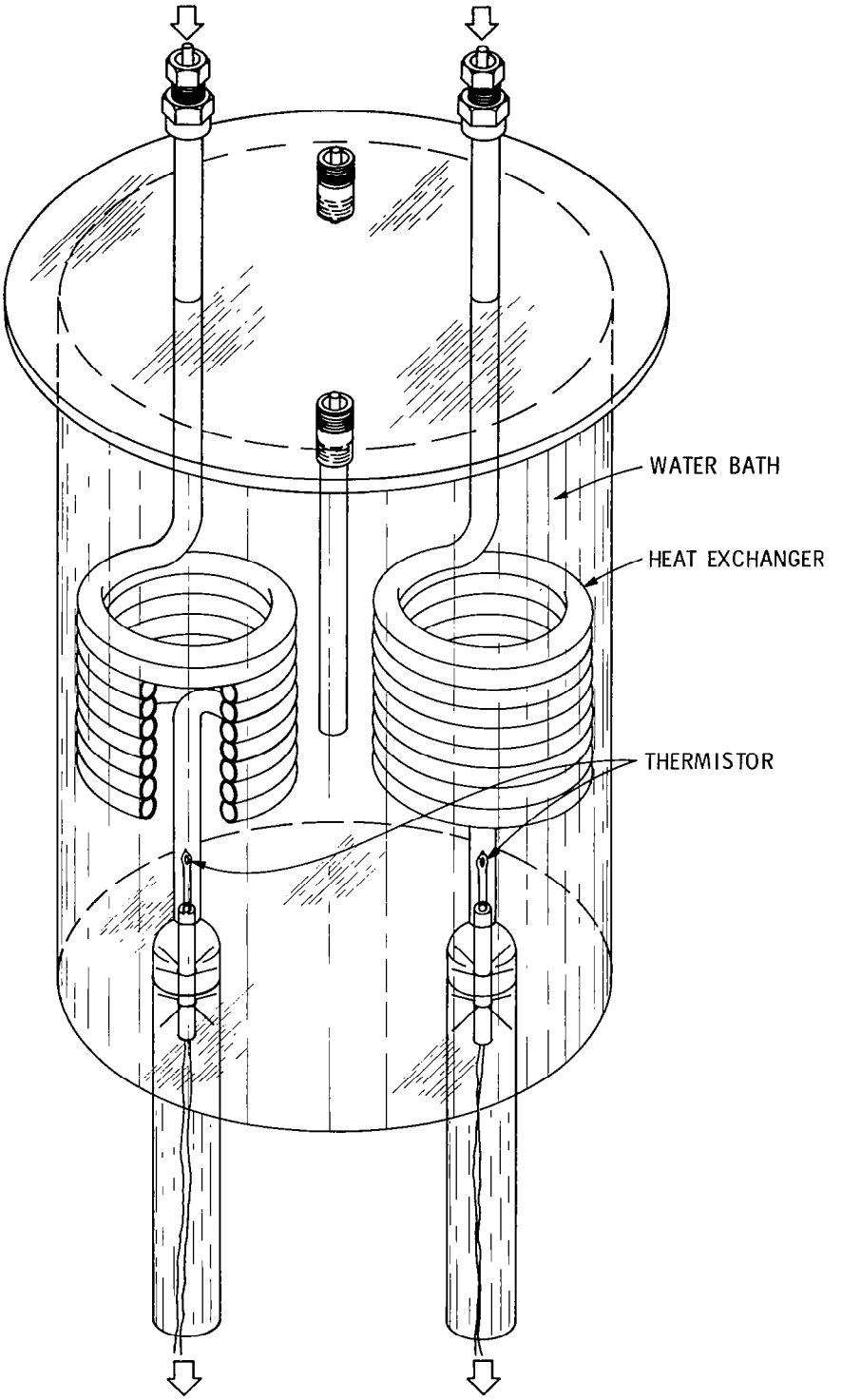

DIAGRAM OF THERMISTOR CALIBRATOR

Figure 68

Figure 69 shows the results of a calibration test made on a pair of 0.0145 inch diameter thermistors. Note the two distinct curves obtained using slightly different flow levels on the reference probe. The variation in the level of the curves with the smaller slope was probably caused by small differences in temperature level. A significant observation arising from the use of the calibrator was the good stability achieved at high output sensitivity as a result of improved temperature control. This result coupled with the results from the Model 1 scanner emphasized the need for careful consideration of the temperature control aspects of the thermistor scanner technique. Another encouraging result was the very rapid response of the thermistor to changes in test gas velocity; a necessary requirement if a continuous scanning mode of operation is to be considered.

Scanner Assembly Model 2. A second scanner was assembled to examine temperature control problems and to obtain an estimate of the sensitivity of thermistor bridge output to sample permeability variations. A photograph of the assembly is shown in figure 70. The probe and reference thermistors (0.0145 inch diameter) were mounted in fixed positions relative to the porous sample. The whole assembly was sealed in a plastic box with the necessary test gas connections. A sample traversing mechanism with micrometer adjustment was also provided.

This assembly along with an input heat exchanger was immersed in a water bath regulated to ± 0.05°C. at about 19°C. The improvement in stability of the output signal was immediately apparent although considerable time was required to reach equilibrium. The long equilibrium times resulted from the poor thermal conductivity and relatively large volume of the plastic container. However, the sensitivity was increased sufficiently that another source of thermal variation could be observed; ambient temperature variations caused the resistor elements of the thermistor bridge circuit to change resistance and alter the bridge output.

Tests made with the reference thermistor at different locations showed a minimum time delay in response to changing flow conditions when

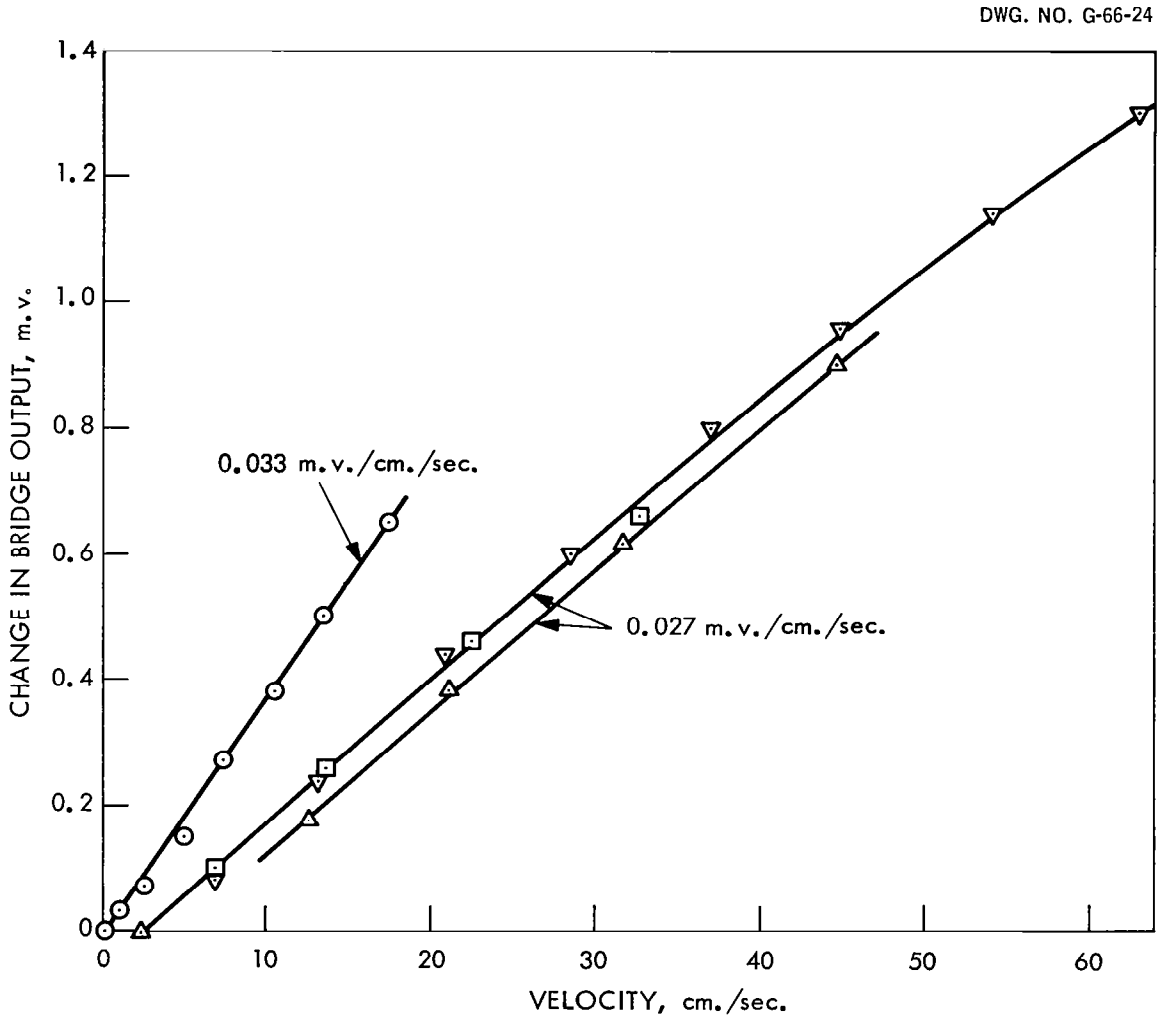

CALIBRATION OF 0.0145-INCH DIAMETER THERMISTORS

Figure 69

PHOTO NO. PH-65-1546

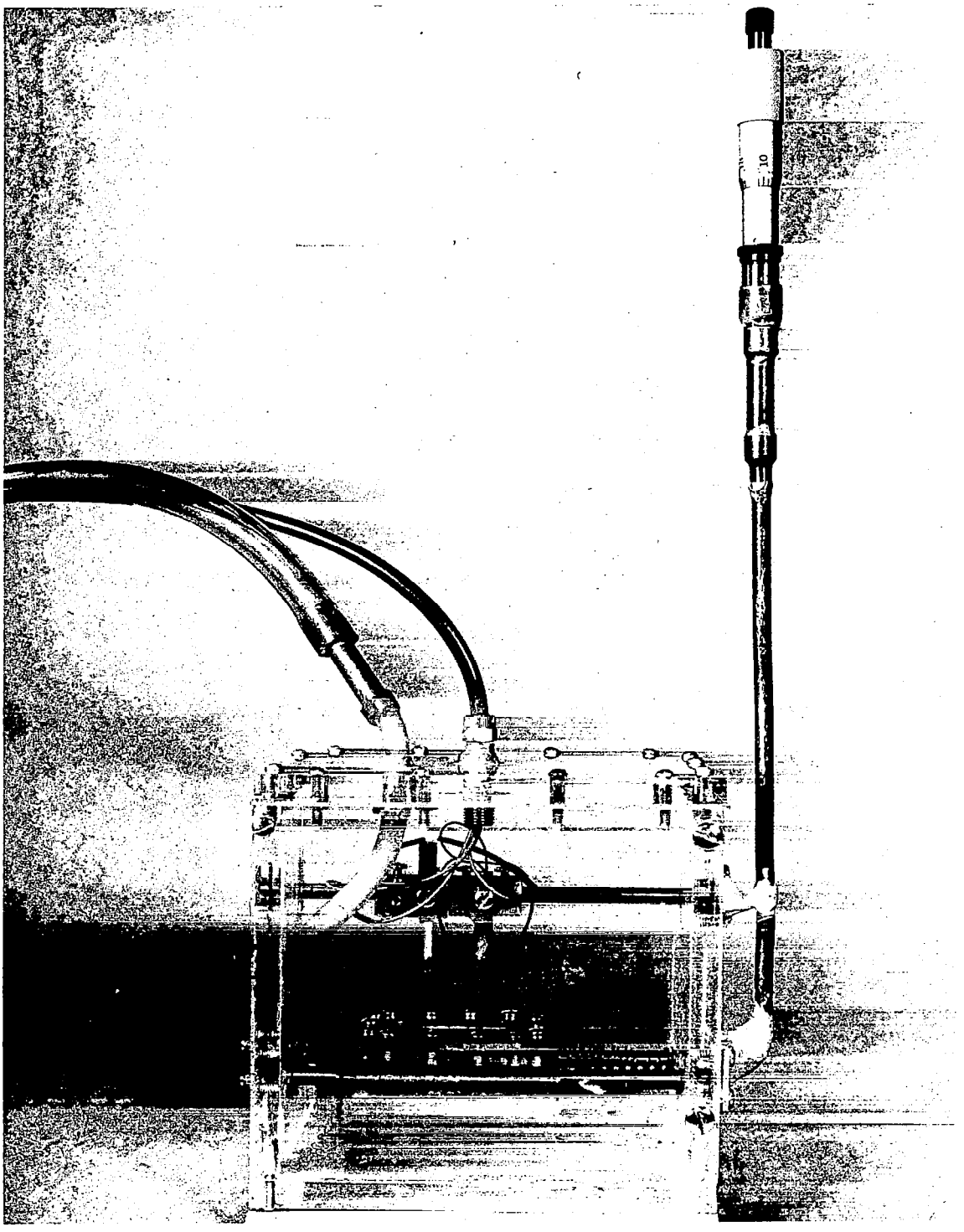

SCANNER ASSEMBLY MODEL 2
Figure 70

the reference thermistor was located in the flowing stream. However, since both thermistors occupied the same volume their response could not be independently controlled. These problems precluded the usefulness of information obtained from scans across the sample surface so a different approach was used to estimate the bridge sensitivity to permeability variations.

The two thermistors were positioned over separate areas of the sample and left undisturbed; then the flow through the sample was changed by varying the pressure differential across the sample. This procedure results in different gas velocities at the sample surface. The velocity-differential pressure relationship for the sample used in these tests is shown in figure 71. The average velocity, V_a, at the sample surface was calculated as follows.

$$V_a = \frac{\text{Volumetric flow}}{\text{Sample area x void fraction}}$$

Ideally, if the sample were homogeneous and the thermistors perfectly matched, no bridge unbalance should result as the differential pressure across the sample was changed. A typical result of such a test is shown in figure 72. The changes in bridge output are thought to represent changes in local gas velocity. The differential pressures and flow level are indicated at each equilibrium point. Several general observations can be made from these data. First, the long term drift is apparent from the 60 centimeters of mercury and 10 centimeters of mercury points. Secondly, the equilibrium problem is clearly evident from the shape of the traces. The circuit should respond rapidly and produce a step function trace if continuous scanning is to be considered. As discussed above, these long equilibrium times probably resulted from design problems rather than a basic fault of the technique. Finally, these data can be used to obtain an estimate of the measurement sensitivity.

From figure 72 a value of about 0.008 millivolt per centimeter of mercury change in differential pressure is obtained. Using figure 71 this result can be converted to about 0.02 millivolt for a centimeter per

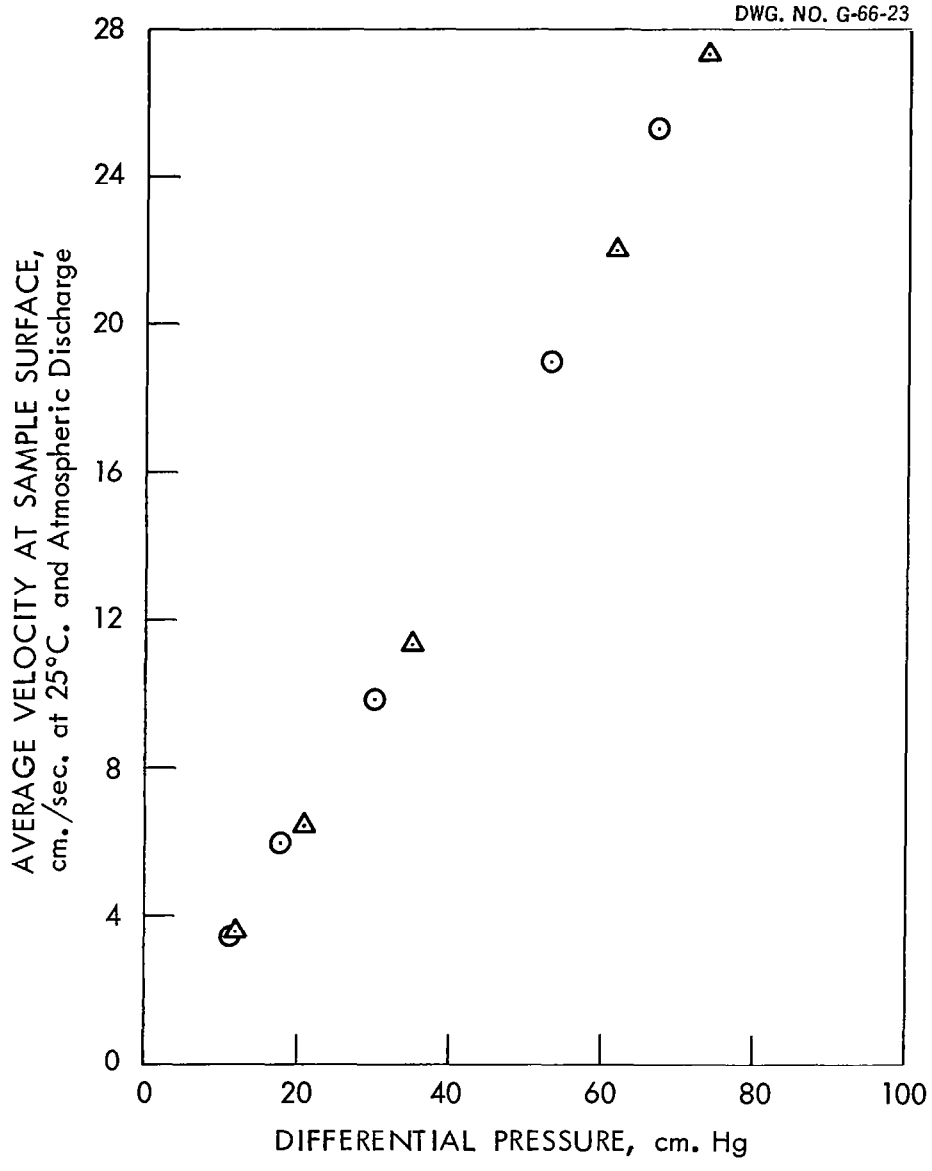

FLOW CHARACTERISTICS OF POROUS SAMPLE TESTED IN ASSEMBLY MODEL 2

Figure 71

DWG. NO. G-66-26

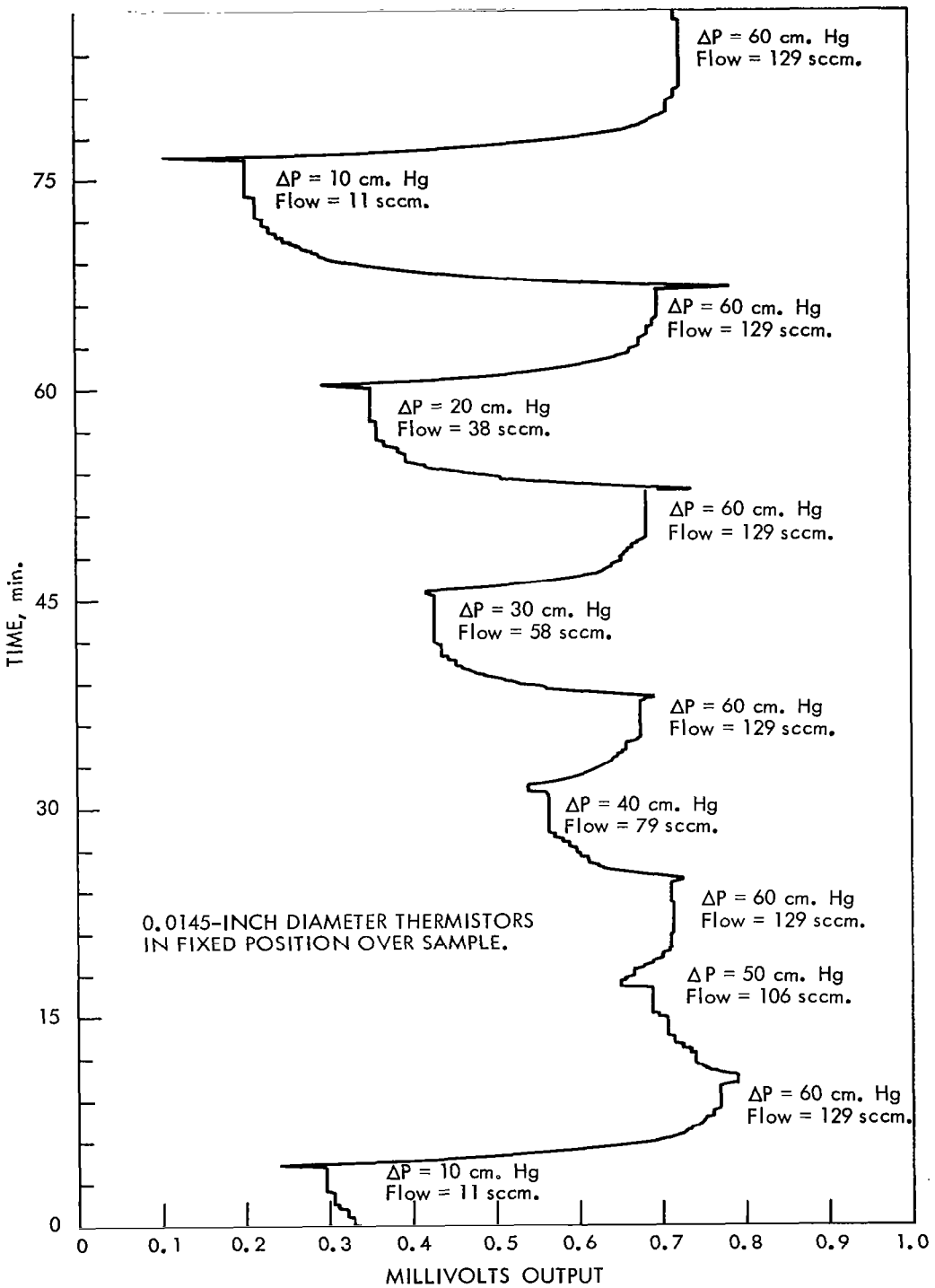

RECORDER TRACE SHOWING THERMISTOR BRIDGE OUTPUT AS A FUNCTION OF SAMPLE DIFFERENTIAL PRESSURE

Figure 72

second change in velocity at low differential pressures. This value is in good agreement with that obtained for similar thermistors tested in the Thermistor Calibrator (figure 69). It is of interest to estimate what this sensitivity might mean in terms of changes in ionizer pore size.

If one assumes that the volume flow is a function of the fourth power of the pore radius then the velocity can be expressed as,

$$V = \frac{\text{Flow}}{\text{Area}} = \frac{Kr^4}{\pi r^2} = Kr^2$$

where approximately,

$$\frac{\Delta V}{V} = \frac{2Kr\Delta r}{Kr^2} = \frac{2\Delta r}{r} \quad .$$

For a ten-percent change in pore radius ($\frac{\Delta r}{r} = 0.1$) $\Delta V = 0.2V$. If the velocity is taken as 20 centimeters per second then ΔV would be equal to 4 centimeters per second which would be equivalent to 0.08 millivolt change in bridge output. Therefore, a ten-percent change in pore size, or equivalent pore density, would be seen as a change in bridge output of about 0.08 millivolt. This estimated sensitivity requirement seems quite realistic in terms of the experimental data obtained to date. These results must be considered as a rough estimate only. However, they do illustrate the potential of the scanning technique.

Current Effort. Based on the results obtained in the experiments described above, it is concluded that the thermistor scanning technique is a promising test procedure. However, very careful consideration must be given to thermal design factors, as well as to the physical relationships between the test and reference thermistor probes.

A new scanner, Model 3, has been designed and is being fabricated. This assembly will provide greater flexibility and control of the variables to be evaluated.

The following principal features have been incorporated into the assembly:

1. The body of the scanner is made from a large brass block for thermal stability.

2. Direct thermal contact is maintained between test sample and scanner body.

3. Reference and test thermistor probes are placed in separate flow chambers over individual porous samples.

4. Individual flow control is provided to the two test chambers. This will allow the reference thermistor to operate on either an absolute or relative basis.

5. A limited amount of scanning with the test probe will be possible by manual rotation of the probe in a circular path above the sample.

6. Micrometer adjustment is provided to accurately position both thermistors above the porous samples.

7. The resistor bridge elements are sealed in mineral oil inside the brass body of the scanner.

The new scanning assembly will be evaluated using an improved liquid temperature bath. The initial evaluation will be made with the 0.0145-inch diameter thermistors. Smaller thermistor probes will also be evaluated.

~~SECRET~~

Report Number: K-1672 Subject Category: SPECIAL

DISTRIBUTION

Internal Distribution

1 - 28. Oak Ridge Gaseous Diffusion Plant

External Distribution

29 - 30. Oak Ridge Operations Office
Attention: C. A. Keller
Library
31 - 32. Atomic Energy Commission, Washington
33 - 38. NASA Lewis Research Center
Attention: Anglin, Albert E., Jr.
Eski, John R.
Rayle, Warren D.
Riley, Thomas J.
Saunders, Neal T.
Librarian